UiO : **Department of Geosciences**
University of Oslo

Detection and Location of Tremor signals:

A case study from East Java, Indonesia.

Sergio A. Díaz
Master's Thesis, Autumn 2021

Abstract

Mt. Bromo is a strombolian-type volcano in East Java, Indonesia, that entered into one of its main eruption periods; between November 2015 and January 2016. The activity was registered by several seismic stations, including a 2-years temporary seismic network deployed to study the dynamics of a near sediment-hosted geothermal system called LUSI. Therefore, the following work reports the achieved detections of the events recorded by using all 3 components, and their locations in latitude, longitude and depth, all from a proposed automatic processing procedure. The detection was done using a coincidence trigger method in the available components to adjust the start and end of each signal, and the first-arrival picks were validated through a polarization analysis. The location process was achieved using the Oct-Tree importance sampling method throughout a probabilistic density function. A total of 32'787 events were detected with higher occurrence during a number of periods, where some of them can be correlated to the eruption period of Mt. Bromo. The events detected are mainly tremor signals of 2 to 4 minutes duration, with weak first-arrival impulses. The locations with low errors (RMS $\leq$ 1.0; 3'965 events) revealed multiple superficial sources, concentrated between 0 and 5 Km depth, originating from Mt. Bromo and 4 other main volcanic structures nearby. Other sources are found deeper, between 10 to 50 Km depth, and are attributed mainly to interactions between the magmatic chambers of the volcanoes, and movements in pre-existing sutures zones (faults) from overpressure of magmatic activity. Chronologically, a peak preceding the main eruption was found, characterized by an increase in Volcano-Tectonic-type (VT) signals beneath Mt. Bromo. This is consistent with cases observed at other similar strombolian-type volcanoes prior to eruptions. After an assessment of the automatic processing procedure used, we suggest promising improvements for future works by: 1) applying an association method based on the same principle as the coincidence trigger used in the detection step, and 2) using the polarization analysis in a sliding window along the event signal to re-pick the first-arrivals.

Bromo er en vulkan av strombolsk type i Øst-Java, Indonesia, som inngikk en av de viktigste utbruddsperiodene; mellom november 2015 og januar 2016. Aktiviteten ble registrert fra flere seismiske stasjoner, inkludert et 2-årig midlertidig seismisk nettverk som ble distribuert for å studere dynamikken i et geotermisk system nær-sediment som er kalt LUSI. Denne rapporten tar for seg de detekterte funnene med alle 3 komponenter, samt deres plasseringer i breddegrad, lengdegrad og dybde, alt fra en foreslått automatisk behandlingsprosedyre. Deteksjonen ble utført ved hjelp av en tilfeldighetsutløsermetode i de tilgjengelige komponentene for å justere start og slutt på hvert signal, og de første ankomstvalgene ble validert gjennom en polarisasjonsanalyse. Lokaliseringsprosessen ble oppnådd ved hjelp av prøvetakingsmetoden for Oct-Tree-betydning gjennom en sannsynlighetsdensitetsfunksjon. Totalt av 32 787 hendelser ble oppdaget med høyere forekomst i løpet av en rekke perioder, hvor noen av dem kan korreleres med utbruddsperioden til Mount Bromo. Hendelsene som oppdages er hovedsakelig tremorsignaler med en varighet på 2 til 4 minutter, med svake impulser fra første ankomst. Stedene med lave feil (RMS $\leq$ 1.0; 3'965 hendelser) avslørte flere nær-overflate kilder, konsentrert mellom 0 og 5 km dybde, som stammer fra Mount Bromo og 4 andre vulkanske strukturer i nærheten. Andre kilder finnes dypere, mellom 10 og 50 km dyp, og tilskrives hovedsakelig interaksjoner mellom vulkanenes magmatiske kamre og bevegelser i eksisterende forkastnings strukturer fra overtrykk av magmatisk aktivitet. Kronologisk ble det funnet en topp før hoved utbruddet, preget av en økning i VT-signaler (vulkan-tektonisk) under Bromo-fjellet. Dette er i samsvar med tilfeller observert ved andre lignende vulkaner av strombolisk type før utbrudd. Etter en vurdering av den benyttede automatiske behandlingsprosedyren, foreslås det lovende forbedringer for fremtidige arbeider ved: 1) anvende en assosiasjonsmetode basert på det samme prinsippet som tilfeldighetsutløseren som ble brukt i deteksjonstrinnet, og 2) å bruke polarisasjonsanalysen i en glidende vinduet langs hendelsessignalet for å velge de første ankomstene på nytt.

Acknowledgments

Firstly, I would like to express my gratitude to my main supervisor, Valerie Maupin, for her guidance, observations and discussions throughout this project. Also for her audit towards the fulfillment of the master program. The lessons I have learned trespass beyond this work, as they are for life itself.

Moreover, I want to thank my co-supervisor Adriano Mazzini for his reviews on this document, the help with the structure, and the support with the literature material.

Special thanks to Riccardo Minetto, Matteo Lupi, Karyono, Pasquale De Gori and Luisa Valoroso for the technical information regarding the dataset. Also to the IT staff at the Department of Geosciences and the Sigma2-HPC project team for their technical support towards the computational resources used in this project.

The dataset handled in this work is part of the European Union's Seventh Framework Programme Grant agreement n° 308126 (LUSI LAB project, PI A. Mazzini), funded by the European Research Council.

I also thank the Geophysical Instrument Pool Potsdam (GIPP) for providing the instruments for the SEED experiment in the framework of the LUSI LAB project.

The experience of living in a foreign land was more challenging, and yet more amazing than what I expected. The COVID-19 pandemic and many more situations set my body and mind into test. However, I could not have got through without the support of my family and friends; here in Oslo and abroad. Therefore my eternal gratitude goes to them, for they gave me the strength to finish this path.

"Tusen hjertelig takk for alt".

Contents

List of Figures

List of Tables

CHAPTER 1

Introduction

Along the history, humankind has tried to explain the origin of the ground movements (called earthquakes), and why they happen. These are unknown aspects that many civilizations have tried to solve by measuring somehow this phenomenon; from the first instrument by Zhang Heng in ancient China (132 A.D.), to the modern basis of the electromagnetic seismometer, invented by Boris Galitzin in 1906 (Yan and Hsiao, 2006). The first explanations came from diverse mythological beliefs; some of them suggesting it was an act of divine judgement and punishment from superior beings (Dimock et al., 1989; Smits, 2006; Lloyd, 2012; Ginevra, 2018). Nowadays, the cause of earthquakes has been solved at some level with the use of the plate tectonics theory, postulated in the 1960s by Alfred Wegener (Greene, 2015). Nevertheless, this is just a simple answer since it is far from complete. Some plate boundaries interact smoothly, others are enhanced by catastrophic failures, and in the meanwhile, stress can also accumulate as intra-plate local fields (Kanamori and Brodsky, 2004).

The release of these stresses and contained forces produce waves that propagates through the earth, and depending on their strength or released energy (magnitude), it could be measured locally or globally (Stein and Wysession, 2009). The propagated waves are catalogued into 2 main groups: 1) the compression and sheared waves (P and S), which are called body waves, and 2) the Rayleigh and Love waves (R and L), which are called surface waves and, according to the name, they travel only at the interface between two different media, i.e. earth and atmosphere (Stein and Wysession, 2009).

Within the active margin between tectonic plates, volcanic activity occurs, and this is inexorably related with earthquakes through plate tectonics (Hill et al., 2002). This is the case of the Indonesian territory, which posses 147 volcanoes; 76 of them classified as active volcanoes and distributed along the islands of Java, Lesser Sunda, Sumatra, and Clebes (Hariyono and Liliasari, 2018).

On the end of 2015, a Strombolian-type volcano located at the east side of the Java island, known as Mt. Bromo, erupted for near 3 months (Sukir et al., 2017) (see Figure 1.1b). The activity caused crop failure for 473 farmers, change in flight schedules, and its ash emissions affected the near-area visibility, which resulted in traffic accidents and human health impact (Venzke, 2016; Rachmawati et al., 2018; Wardoyo et al., 2020). It also represented losses in the tourism industry, with a total loss estimated around 126 billion Rupiahs (local currency) (Rachmawati et al., 2018). Due to the risk and recurrent activity, Mt. Bromo has been monitored through various methods such as remote sensing, geophysical measurements, ground deformation, gas emissions, and visual observations (Sukir et al., 2017).

As part of the geophysical methods used to follow Mt. Bromo's activity, passive seismic is one of the main approaches, and typically used. Authors like Sukir et al. (2017) studied tremor signals from February 2016, with the use of 3 temporal seismic stations near the crater. The authors applied a polarization analysis to several time-windows on the record, and obtained back-azimuth and incidence-angle values, which they use to locate the tremor signals.

Minetto et al. (2019) also aimed to study the eruption period with different stations. The network used was deployed in the framework of the LUSI LAB project (Mazzini, 2018), for a period of 2 years (2015-2016) with the purpose of investigate the structures and dynamics beneath LUSI, a sediment-hosted

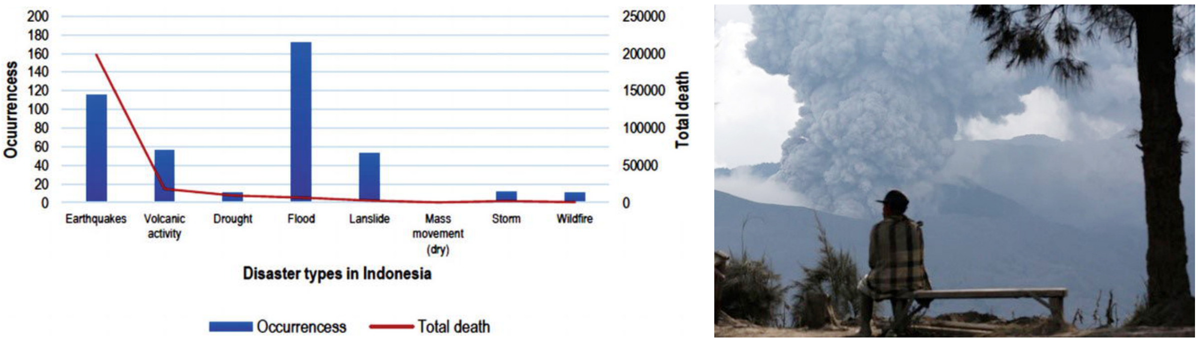

(a) (b)

Figure 1.1: (a): Statistics of disaster impact in Indonesia, from 1900 to 2016. Notice that the total numbers of death are the highest for earthquakes and volcanic activity disasters *From Hariyono and Liliasari (2018).* (b): Photo of a man watching an ash plume rising from Mt. Bromo crater. Photo taken on the date 2016-05-01 (year-month-day). *From Venzke (2016).*

geothermal system (Mazzini et al., 2012; Karyono et al., 2015; Fallahi et al., 2017; Panzera et al., 2018; Mazzini, 2018; Lupi et al., 2018; Obermann et al., 2018). To the configuration, Minetto et al. (2019) added 3 other stations from the permanent national network around Mt. Bromo, in an attempt to increase the azimuthal coverage around the volcano. Working with only the vertical channels, the authors spotted 2 types of tremors (continuous and fragmented signals), and attempt a localization of the continuous tremor through station-pair cross-correlation (CC) between the envelope of the signals, on a 2D grid-search, and assuming a constant velocity of 1.35 Km/s.

Both studies from Sukir et al. (2017) and Minetto et al. (2019) identified signals originating from Mt. Bromo. However, the methods used by Minetto et al. (2019) imply that the tremor was treated as pure Rayleigh waves, and traveled through the surface from source to the stations. Besides this, Minetto et al. (2019) encountered an apparent velocity of 3.3 Km/s from the time-delay of similar signals recorded a different stations. This then suggests that other possible tremor sources besides the assumed one could be present in the recording period, in depths that could even imply origin from the subduction channel.

A clear approach to the study of the tremor signals seen by Minetto et al. (2019) is important in order to achieve reliable location results, which could describe the temporal dynamics of the volcanic activity and other potential sources in the area. Such results may be used as tools for mitigating the effects of future eruptions, as they represent a risk to local communities (see Figure 1.1a).

Therefore, the aim of this work is to investigate the origin and characteristics of these signals through a designed automatic processing routine that could achieve detections and 3D locations (latitude, longitude, depth). To achieve this, the following workflow was used: 1) an inspection of the 2-years recordings from the LUSI LAB network across time and frequency ranges, 2) an exploration into some of the most popular signal detection algorithms, 3) detection of the signals through a proposed method that uses all the available components from each station, 4) association of the detections, 5) a polarization analysis to first-arrival picks in order to assure the P-wave arrivals, and differentiate potential P-wave from Rayleigh phases, and 6) a localization attempt in 3D using the P-wave arrivals.

CHAPTER 2

Geological Setting

2.1 Tectonic setting of the Java island

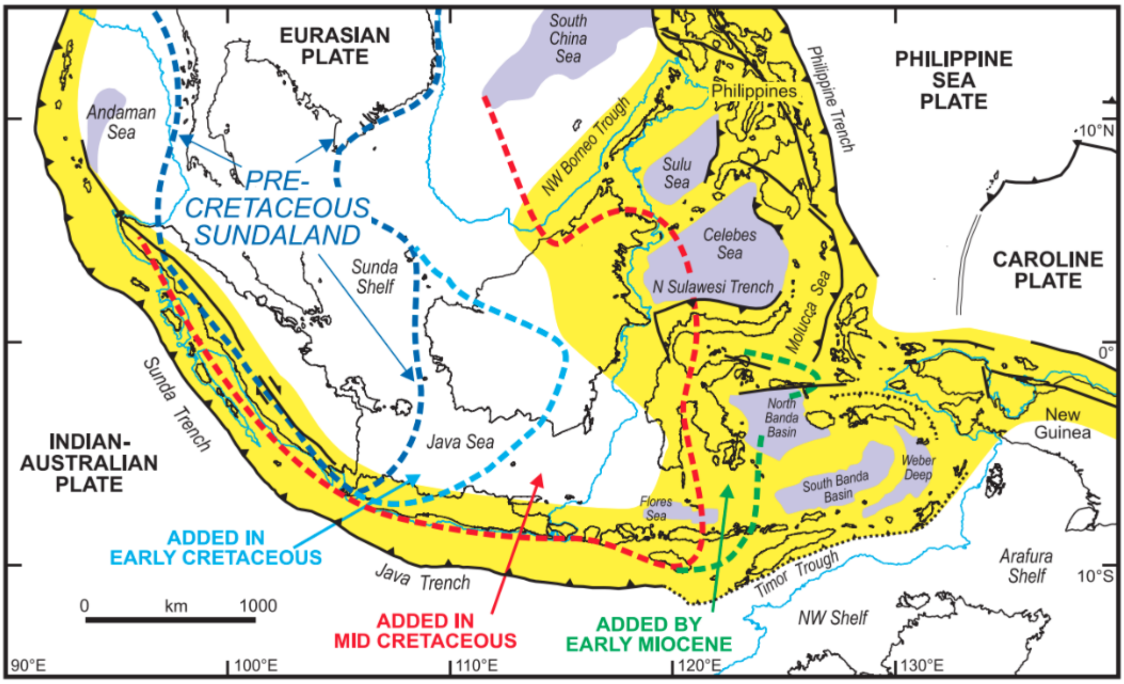

Figure 2.1: Tectonic interpretation of the accretion processes at the southwestern part of Asia. *From Hall (2011).*

Java is an island located in the southwestern part of Indonesia, occupying an active margin between the Eurasian continental plate; specifically the Sunda block (Susilo et al., 2015), and the Indo-Australian plate that have converged since the Jurassic-Cretaceous (Satyana, 2006; Kundu and Gahalaut, 2011) (see Figure 2.1). The margin between these two plates developed the Sunda trench, which extends from northwestern Sumatra, along the Java island and ends near Flores (Kundu and Gahalaut, 2011). However, authors like Hall (2011) divide this trench into two sections; the Sunda trench at the northwestern part of the Sunda block and the Java trench at the south, as shown in Figure 2.1. The rate of the Indo-Australian plate in a convergent motion towards the Eurasian plate decreases gradually from the eastern end to the western end of the Sumatra coast (Kundu and Gahalaut, 2011), describing a decrease all along the Sunda trench from 76 mm/yr to 60 mm/yr, respectively (Müller et al., 2008).

The basement of the Java island is composed of Eurasian continental crust in the northwestern and central part of the island, and intermediate accreted terranes in the southwestern, south-central and in some part of eastern side of Java (Satyana, 2006, 2007). There are several tectonic elements as a result from the convergence: subduction trenches, volcano-magmatic arcs, accretionary prisms and basins of type fore-arc and back-arc (Satyana, 2006, 2007). Central Java acts as a transition between the dominant continental basement from West Java and the intermediate basement from East Java, where sedimentary and volcanoclastic rocks are affected by magmatic intrusions and cover most of the basement rocks (Satyana, 2006).

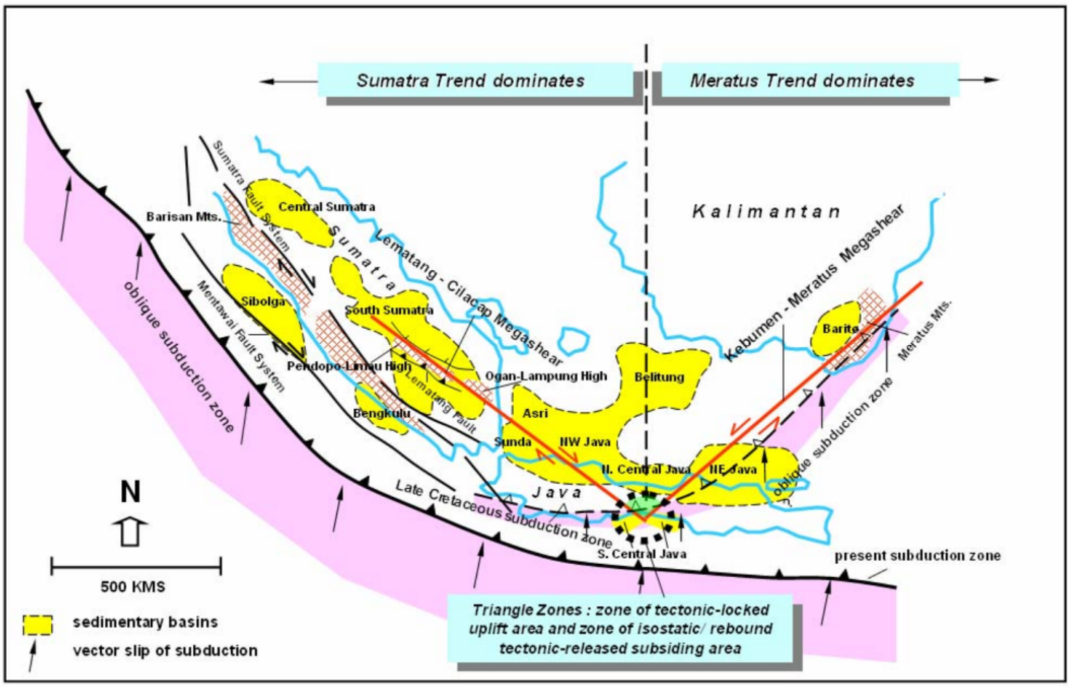

Figure 2.2: Main trends interpretation as two strike-lip faults act on Central Java, Indonesia, which works as the center of structural trends between the Sumatra and the Meratus ones (Satyana, 2007). *From Satyana (2007).*

The Java island present structural patterns based on surface geology and remote sensing data (Satyana, 2007). Figure 2.2 shows the main structural trends presented on the island. These structures may be subdivided into four groups: (1) the Meratus Trend, from Late Cretaceous, with a strike of southwest-northeast direction, (2) the Sumatra Trend (from Late Cretaceous - Paleocene) with a northwest-southeast domain, (3) the Sunda Trend (Eocene - Late Oligocene) with a north-south domain, and (4) the Java Trend (Early Miocene) with an east-west domain (Satyana, 2007). The latest is mainly present in the West Java region and disappear towards the eastern part of Central Java. This conclusion is also supported by seismic data (Gresko et al., 1995; Ryacudu and Bachtiar, 2000; Satyana, 2007). Central Java occupies a structural transition between the Sumatra (Late Cretaceous - Paleogene) and the Meratus Trends (Late Cretaceous), which are at the east and west of Central Java (Satyana, 2007).

The mentioned structural configuration seems to be also supported by Marliyani et al. (2020). With an analysis of physical parameters observed in Digital Elevation Models (DEM) from Quaternary-age monogenetic and polygenetic volcanoes and volcanic field in Java, the authors were able to determine the maximum horizontal compressive stress σ_{Hmax} orientations through the island. The orientation of σ_{Hmax} on the western part of the island is NE-SW, but then gradually rotates into SE-NW trends while heading to the east part of the island.

2.2 East Java and its Structural Domain

The eastern part of the Java island is a basin constructed by a basement with a long tectonic history related to active margin; collision of micro-continents and continent growth by coalescence of accretionary prisms (Satyana et al., 2004). It is well known for its hydrocarbon potential and for the interaction between active volcanism and piercement structures that have been active through at least the last 8 Ma (Satyana et al., 2004; Satyana, 2007; Moscariello et al., 2018; Mazzini, 2018).

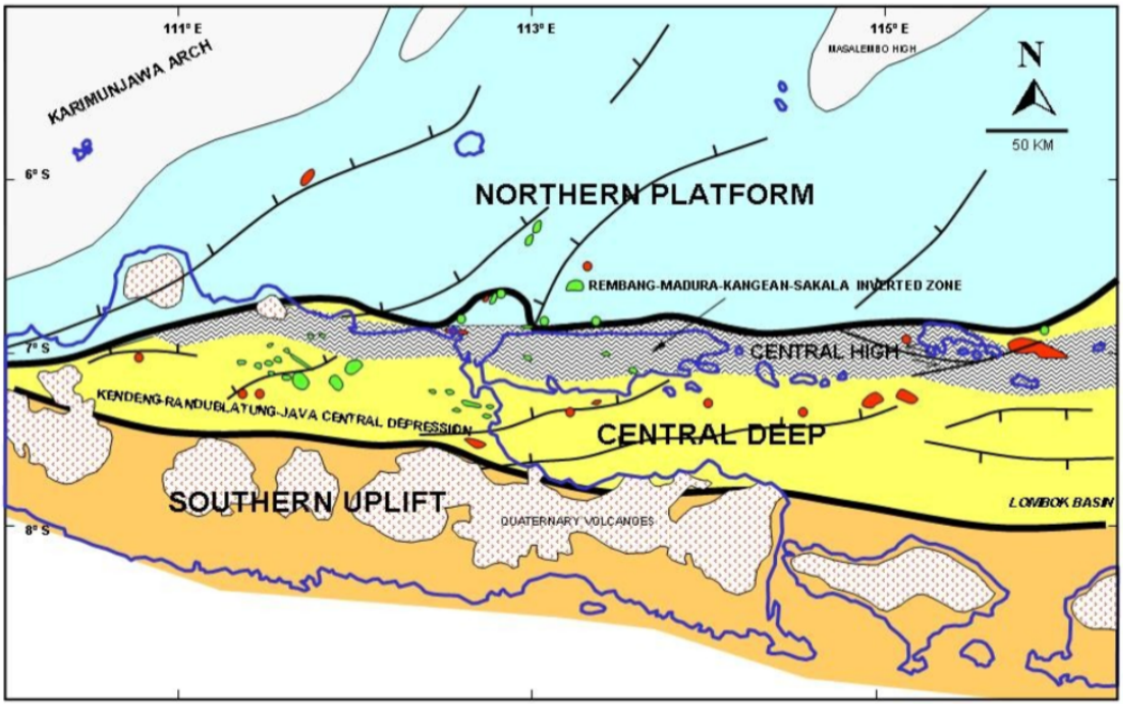

Figure 2.3: Main tectonic configurations and structural divisions of East Java, Indonesia. The Northern Platform, Central Deep (including the Central High), and Southern Uplift are well appreciated. Inverted, main depressions and quaternary volcanic realms are noticed. *From Satyana et al. (2004).*

The East Java region represents a back-arc basin, as a result of the northwestward subduction zone of the Indo-Australian plate below the Sunda continent during the Late Cretaceous (Istadi et al., 2009; Satyana et al., 2004). It is limited to the west by the Karimunjawa Arch, residing eastwards and deep into the Lombok Basin, and rises northwards onto the Paternoster High (Satyana et al., 2004). The region is divided into three main structural configurations identified from north to south, according to Satyana et al. (2004): the Northern Platform, the Central Deep, and the Southern Uplift (see Figure 2.3).

During the Early Tertiary time a major extensional system prevailed on the area, causing graben systems and rift basins (Istadi et al., 2009). These structures aligned along Pre-Tertiary lines of weakness with NE-SW trends which then shifts to E-W direction while heading south. These two main trends constitutes the structural configuration of the East Java Basin (Satyana et al., 2004; Istadi et al., 2009). The NE-SW trending is interpreted as the prominent structural in all the basin, mostly dominant in the Norther Platform, and reflects the plate boundary trend from the Cretaceous subduction zone and the accretionary prism. The other trends (E-W) develop in the southern part of the basin, and are bound by the Northern Fold Belt (Istadi et al., 2009), also called the Central High; located in the northern part of the Central Deep division (Satyana et al., 2004). This second trend defines the mayor sub-basins and also how the deposition spaces are aligned with these features; parallel to the Madura island and the northern coast of East Java (Istadi et al., 2009).

One of the most noticeable prominent E-W trends is the Rembang-Madura-Kangean-Sakala (RMKS) Fault Zone, with an extension of near 650 Km E-W, and 15 to 40 Km wide (Satyana et al., 2004). It is explained to be the suture between the Paternoster-Kangean micro-continent (Northern Platform basement), and the transitional/intermediate crust with subduction accretionary complex (basement of the East Java Basin). To the north of the fault zone the basement was segmented, forming high trends and folding zones (Central High), and to the south the basement is also segmented but forming narrow ridges and deep through trends (Satyana et al., 2004). Several north-south seismic lines crossing perpendicular to the trend of the fault zone in Madura island reveal the presence of a positive flower structure below the anticlines of Central High division and negative flower structure in the south as a result of the Central Deep depression (Satyana et al., 2004).

2.3 The East Java Basin

The basement at the Central Deep has a NE-SW structural configuration and comprises basement ridges with grabens that works as deposition zones for Tertiary sediments (Istadi et al., 2009). Clastic sediment deposits and carbonate buildups took place during the Eocene and Early Oligocene, and then Late Oligocene and Miocene sequences of carbonates that served as the foundation for the NE-SW trends and highs, called the Kujung limestone (Istadi et al., 2009; Moscariello et al., 2018). The last and most pronounced period of regional compression began in the Late Miocene and continued into the Pleistocene, which resulted into transpressional regimes causing left-lateral movements in E-W directions and shaped the E-W orientation of the anticline structures presented in the area (Istadi et al., 2009). Afterwards, Pliocene and Pleistocene sedimentation began, consisting of eastward prograding mudstone-dominated volcaniclastic deposits. These materials are derived from the Java volcanic arc at the south of the Sidoarjo regency, in the Southern Uplift division (Istadi et al., 2009). The rapid sedimentation rate ongoing during the time resulted in thick deposits of under-compacted shales (Willumsen and Schiller, 1994; Istadi et al., 2009), and this highly plastic zone is pointed to be over-pressured due to an excessive quantity of trapped water and maturing organic-rich materials (Istadi et al., 2009). Today, on the onshore part of the East Java Basin, the Late Oligocene and Miocene carbonate platforms and its E-W anticline structure trendings define the structural boundaries of a series of elongated and narrow deposition zones as the Ngimbang, Kendeng and Porongo basins on top of the big East Java Basin.

2.4 The Modern Sunda Arc

Basement exposures at East Java are rare and only found in the southwestern part of East Java (Smyth et al., 2008), in the Southern Uplift division. These ones are Cretaceous in age and include basaltic pillow lavas, radiolarian cherts, metasedimentary lithologies, schist, and high-grade metamorhpic rocks from subduction metamorphism (Parkinson et al., 1998; Smyth et al., 2008) while the basement rocks represent fragments of ophiolitic affinity accreted during the Late Cretaceous active margin (Smyth et al., 2008).

Above the basement, a volcanic arc was built from Middle Eocene (42 Ma) to the Miocene (18 Ma) in southern Java; southern part of the Southern Uplift division (Smyth et al., 2008), which is known to have an extend from East Java into West Java (Soeria-Atmadja et al., 1994; Smyth et al., 2008) and named by Smyth et al. (2008) as the Southern Mountains Arc. It consist of volcanic products of thickness superior to 2500 m (Soeria-Atmadja et al., 1994; Smyth et al., 2008) of Middle Miocene reworked volcanoclastic deposits, Oligocene-Miocene andesites and intrusive bodies (Soeria-Atmadja et al., 1994; Smyth et al., 2008), which indicates a most voluminous and explosive eruptive style (Smyth et al., 2008).

The present-day active volcanoes of the Sunda Arc in Java are located in the transition between the Central Deep and the Southern Uplift divisions, varying in height as some of them are higher than

3000 m in elevation, and forming a NW-SE trend; parallel to the Java trench, which are labeled as the backbone of the island (Marliyani et al., 2020). Most of these active volcanoes are situated near 100 Km above the subducting slab and approximately 300 Km north from the Java trench (Marliyani et al., 2020).

The start activity of the present-day volcanoes of the Sunda Arc in Java differs between different authors; from 12 - 10 Ma (Zaputlyaeva et al., 2020), 10 Ma (Soeria-Atmadja et al., 1994), or 8 Ma (Satyana et al., 2004; Satyana, 2007; Moscariello et al., 2018; Mazzini, 2018), which ranges between Mid to Late Miocene. They are built mainly in the southern part of the Kendeng basin, but also locally overlapping the edge of the Southern Mountains Arc (Smyth et al., 2008). The average composition of the present-day volcanic products is basaltic andesite, which is much more of a basic composition than the average from the Southern Mountains Arc products (Smyth et al., 2008; Marliyani et al., 2020), and nowadays, most of their eruptive and epiclastic materials cover a significant portion of the Java island (Marliyani et al., 2020).

With this in mind, according to Smyth et al. (2008), the Kendeng Basin began to form at the same time as the Sunda arc activity at the south side of the basin, which means that its subsidence history is closely linked to the arc activity, even if the main basin fill was derived from the Southern Mountain Arc (Smyth et al., 2008). Besides, there is no evidence of compressional loading that contributed to the the basin formation since thrusting in East Java occurred in the Late Neogene, time after the Kendang basin was formed (Smyth et al., 2008). With this, Smyth et al. (2008) suggested that the load of the volcanic arc was the major cause for the basin subsidence.

Nowadays, the Indonesian territory has 147 volcanoes, where 76 of them remain as active and are spread along the islands of Java, Lesser Suda, Sumatra, and Clebes (Hariyono and Liliasari, 2018). The present-day volcanic structures on East Java are illustrated in Figure 2.4. Most of these volcanoes are of explosive eruption style, with exception from the Arjuno-Welirang volcanic complex (AW); which is of a moderately explosive one, and Lamongan; which is mostly effusive (Pfeiffer, 2017). Also, excluding Malang Plin all the other volcanoes are of Stratovolcano type; since the mentioned one is of type Maars (Pfeiffer, 2017).

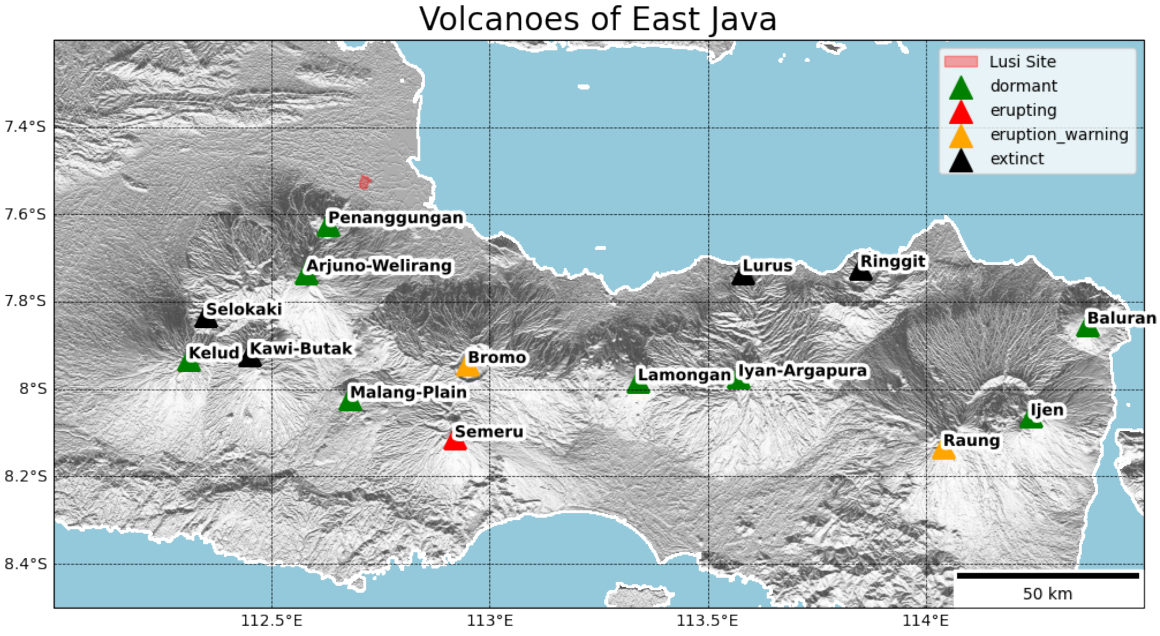

Figure 2.4: Volcanoes of the East Java and the LUSI Site, Indonesia. Volcanic activity status and eruptive styles were taken from the webpage *Volcano Discovery* (Pfeiffer, 2017).

2.5 Hydrothermal Systems and other Piercements

On the 29th of May 2006 several unexpected eruptions of 100 °C hot mud and gas took place at NE Java, 200 meters away from the 2.8 Km deep hydrocarbon exploration well Banjarpanji-1 (BJP1) in the Porong area (Mazzini et al., 2007, 2009; Sawolo et al., 2009). The eruption sites were located near 10Km to the NE of the Penanggungan and the AW volcanic complex (see Figure 2.4). The eruption was nicknamed LUSI (**LU**mpur = "mud" in Indoneisan Bahasa; **SI**doarjo = the local regency where the phenomenon occurred), and multidisciplinary studies revealed that this is a sediment-hosted geothermal system (hybrid system) (Mazzini et al., 2007, 2009; Richards, 2011; Miller and Mazzini, 2018; Procesi et al., 2019).

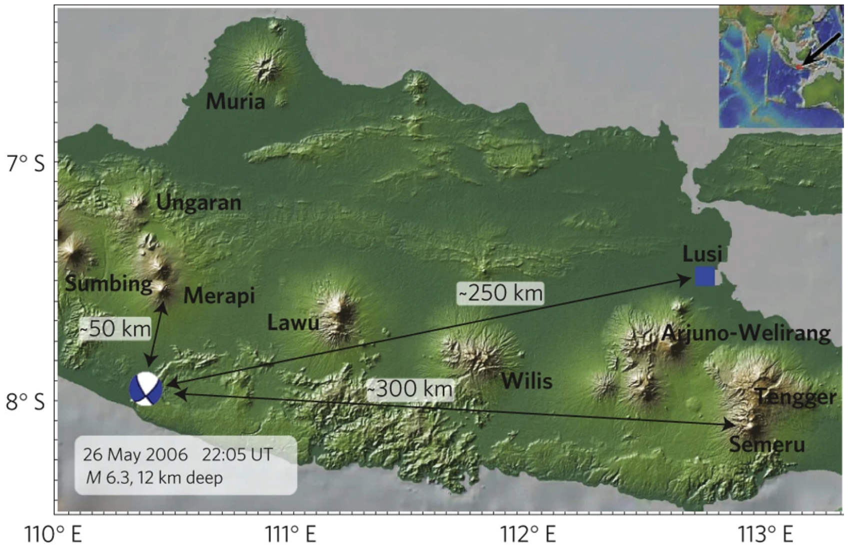

Figure 2.5: The M6.3, 12 Km Yogyakarta earthquake and the epicentral distance with some volcanic structures, including the LUSI site. Studies also shown that the Semeru and Mepari increased their heat flow and erupted volume flux in response to the seismic event (Harris and Ripepe, 2007). *From Lupi et al. (2013).*

The triggering of this mud eruption has been debated (Brumm et al., 2007; Davies et al., 2008; Mazzini et al., 2009; Sawolo et al., 2009, 2010; Lupi et al., 2013), and the proposed scenarios include: by 1) hydrocarbon well-drilling operations near the LUSI site, by 2) the Yogyakarta earthquake (see Figure 2.5), which occurred on the 27th of May 2006, or 3) a combination of earthquake and drilling operations (Brumm et al., 2007).

However, Mazzini et al. (2009) exhibit field observations indicating that the Watukosek fault zone was reactivated after the Yogyakarta event. The fault is located at the NE of the AW volcanic complex and continues trending in the same direction SW-NE (see Figure 2.6) with a strike-slip kinematic (Mazzini et al., 2009). An important fact is that the LUSI site appears to be along the mentioned fault zone, and curiously, other mud eruptions emerged near the fault; in the same SW-NE trend, such as Gunung Anyar, Pulungan, and Kalang Anyar, and hydrothermal springs as Kepulungan, Pacet, Cangar and Songgoriti (see Figure 2.6) (Mazzini et al., 2007). Mazzini et al. (2009) explains that the critical fluid pressure required to induce sediment deformation and upwards migration is dramatically reduced when a strike-slip movements are occurring, and that this idea is consistent with why mud volcanoes and other piercements are often located along fault zones (Mazzini and Etiope, 2017). Also, Lupi et al. (2013) support the Yogyakarta earthquake as the trigger by numerical wave propagation experiments. Based on the high velocity and impedance mudrock layer surrounding the LUSI site, incoming waves energy could have amplified, reflected or focused on the layer, and thus could be sufficient to liquefy the mud source (Lupi et al., 2013).

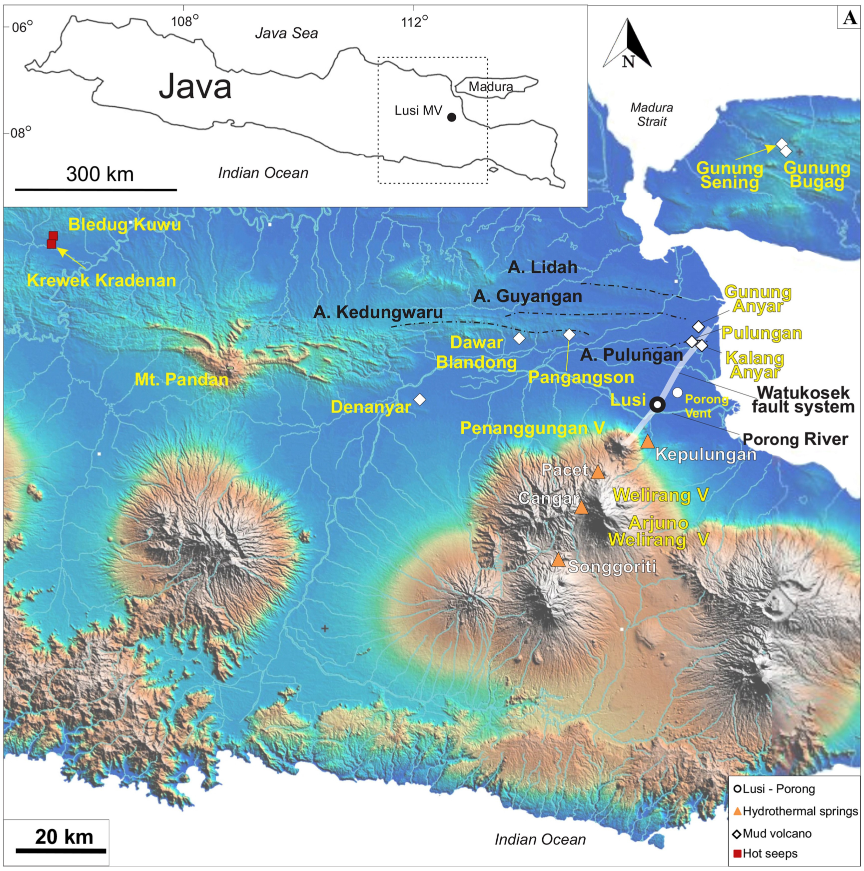

Figure 2.6: Setting of East Java showing the position of the LUSI site, mud volcanoes and hydrothermal springs. The Watukosek fault zone is marked as a white line trending NE from the Penanggungan volcano. Notice the closeness and alignment of the structures along the fault zone. *Modified after Mazzini (2018).*

2.6 Volcanic activity during 2015-2016

Mt. Raung (see Figure 2.4) is one of the most active volcanoes in Indonesia, located at East Java (Kaneko et al., 2019). It has a conical edifice with a height of 3260 meters above sea level, and is categorized as a Strombolian type-volcano (Kaneko et al., 2019). During June to August 2015, an effusive eruption occurred at the intra-caldera cinder cone, burring the caldera floor and forming a "lava lake" (Kaneko et al., 2019). Since the eruption occurred intra-caldera, at high altitude, it was partially observed by local authorities and has not yet been documented due to lack of information (Kaneko et al., 2019).

Mt. Bromo, with 2392 meters height above sea level (Bachri et al., 2015), is one of the most 20 active volcanoes in Indonesia (Hariyono and Liliasari, 2018). It is categorized as a Strombolian type-volcano, and it is located within the Tengger caldera, Probolinggo Regency, East Java (see Figure 2.4). This volcano has exhibit eruptions more than 50 times since 1775 (Sukir et al., 2017), with 4-5 year intervals on its activity (Rachmawati et al., 2018). Its last eruption, on 2015, lasted about 3 months, and resulted in crop failure and deficit in income towards the tourism industry (Rachmawati et al., 2018). It also affected the visibility, traffic accidents, flight schedules, and human health (Wardoyo et al., 2020). Due to the activity intervals, a new one was expected on 2020 (Rachmawati et al., 2018), and confirmed by observations of ash plumes, from the 26th to the 28th of December 2020, with ashfall to the NE (Venzke, 2021).

CHAPTER 3

Previous seismological studies in East Java

Several authors (Fallahi et al., 2017; Obermann et al., 2018; Karyono et al., 2015) have studied the LUSI site from a seismological perspective in accordance to one of the objectives of the LUSI LAB project, which is to understand the relationship between the LUSI hydrothermal area and the near AW heat source (Mazzini, 2018). Each focused on different analysis; from the signal descriptions, through the seismic processing routine, and ending with focal mechanisms and tomography inversions.

3.1 Seismicity at AW and Noise

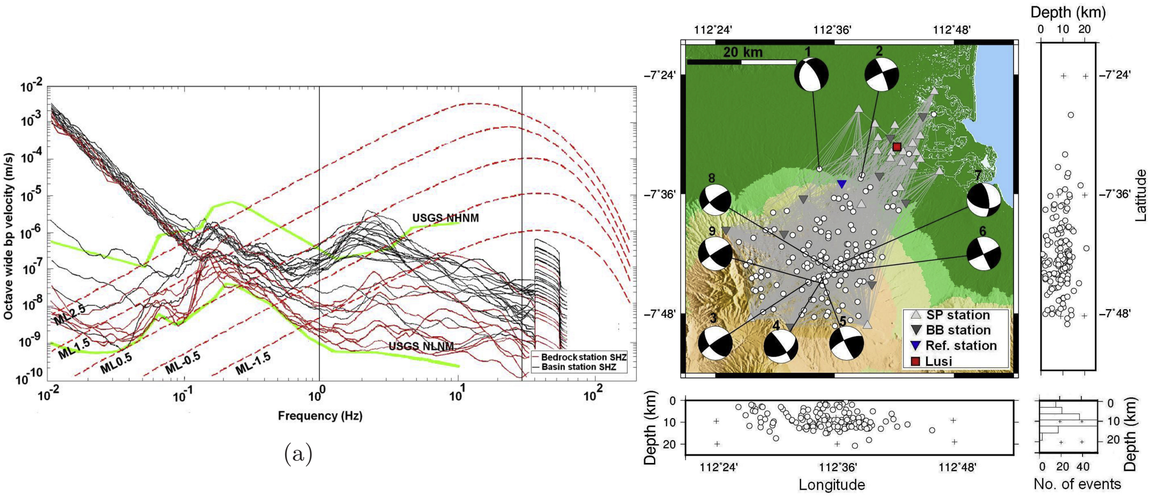

(a)

(b)

Figure 3.1: (a): Ambient seismic noise levels of bedrock stations (red) and basins stations (black). Green curves are the US Geological Survey low and high noise models. Black vertical lines indicate the frequency range of interest for earthquake search. Notice the noise peaks on cut-off frequencies below 0.1 Hz and in the range of 2 - 3 Hz. (b): Relocated microseismicity around the AW volcanic complex. Focal mechanisms indicate mostly a strike-slip kinematic regime. *From Obermann et al. (2018).*

Fallahi et al. (2017) and Obermann et al. (2018) made use of 31 temporal seismic stations from the ERC LusiLab project, to study the dynamics between LUSI and AW through the Watukosek fault zone. Obermann et al. (2018) analyzed recordings from January 2015 to December 2016 to see the earthquakes distribution and retrieved focal mechanisms based on manually picked P-wave first arrivals for 156 microseismic events (see stations in Figure 3.2a).

The authors computed the stations noise levels by producing probability density functions (PDF) of the power spectral density (PSD). They compared the ambient seismic noise levels with a theoretical Brune S-wave source spectra for local earthquakes with local magnitudes ranging from M_L 1.5 to 2.5. Concerning the data status, Obermann et al. (2018) found out that there was moderate to poor signal-to-noise conditions (S/N). They also see a relation in the noise between short-period and broad-band stations. As shown in Figure 3.1a, the short-period stations increase their noise level below the cut-off frequency (0.1 Hz), and the stations around the volcano have lower noise since they are installed in bedrock (see red curves in Figure 3.1a). On the other hand, the stations installed at the basin (around LUSI) exhibit a peak noise around 2 - 3 Hz (see black curves in Figure 3.1a) that is dominant on the basin stations and disappears further into the AW volcanic complex. For this reason, the authors suggest that this noise is likely due to resonance effects and cultural noise in the densely populated basin. Finally, for the picking and location, Obermann et al. (2018) used a band-pass filter from 1 to 30 Hz.

The results of the earthquakes location by Fallahi et al. (2017) and Obermann et al. (2018) shows that most of the events are located beneath the AW volcanic complex, in the upper crust (between 8 and 13 Km depth), instead of being around the LUSI area (see Figure 3.1b). The authors established that theoretically there might be more events, but with magnitude lower than M_L 0.5 since the theoretical threshold for detection is over this magnitude. Based on this, it was concluded that the lack of events around LUSI suggested aseismic deformation beneath the site due to large amount of fluids that may lubricate the Watukosek fault zone. Regarding the focal mechanisms, most of them points towards strike-slip kinematics, which is consistent with observable features as escarpments, river deviation and railroad deformations, as pointed by Mazzini et al. (2009); Obermann et al. (2018).

3.2 Tomography beneath LUSI

In order to understand the plumbing system of the hydrothermal system beneath LUSI, authors like Fallahi et al. (2017) made use of tomographic images produced by seismic events near the area.

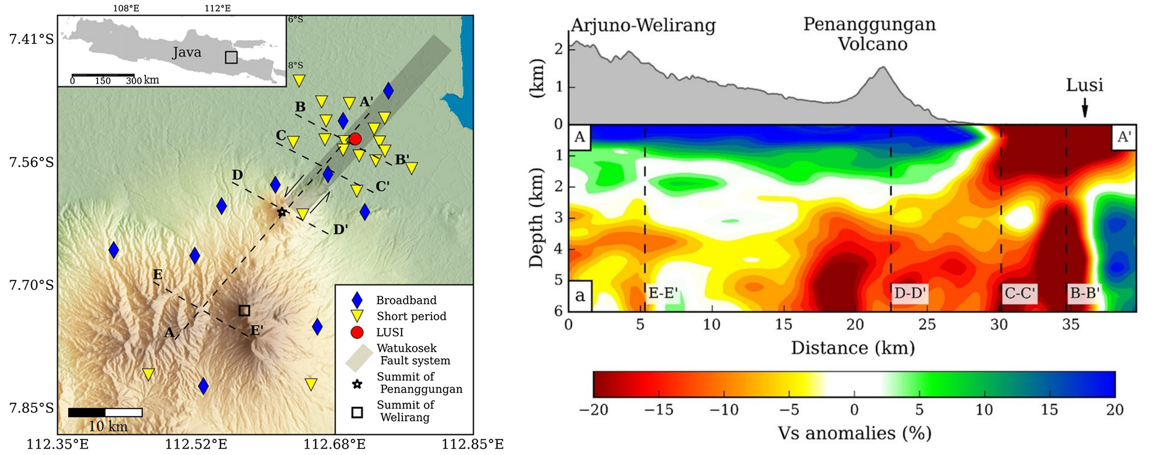

(a) (b)

Figure 3.2: (a): Map showing the network distribution used for the local ambient noise tomography. Short and Broad-Band period stations are illustrated with their locations as yellow inverse triangles and blue diamonds, respectively. (b): Vertical depth cross-section (vertical exaggeration of x2) through the S-wave tomography. Location of the slice is indicated in the (a). Notice the low Vs anomaly under LUSI and how its root seems to come also from beneath the Penanggungan volcano, indicating a connection between them. *Modified after Fallahi et al. (2017).*

Fallahi et al. (2017) made an ambient noise tomography based on the data collected on the temporary network, from January 2015 to November 2016 (see Figure 3.2a). The method consisted on: 1) slicing records into 2 hr length each, 2) applying corrections to the instrumental response, 3) resample the data to 10 Hz, 4) applying a band-pass filtering from 0.05 to 4 Hz, 5) elimination of 2 hr segments with standard deviation higher than 3 times the standard deviation of the daily record, 6) spectral whitening from 0.05 to 4 Hz, and 7) one-bit amplitude normalization. To the final data, a cross-correlation function (CC) was applied for all station pairs and stacked them over 10 months.

Their results showed the presence of an hydrothermal plume originated at, less than 6 Km depth, that reached the surface at LUSI. Also, the authors found that the plume is connnected at depth to the Penanggungan volcano through a near 3 Km wide low S-wave velocity (Vs) anomaly corridor that follows the trend of the Watukosek fault zone (see Figure 3.2b). Through field observations they established that once the hot volcanic fluids, coming from the Penanggungan chambers, reached the source rock, an overpressure was generated from the baking of organic-rich sediments, and forced the displacement of it up to surface.

3.3 Bromo Tremors

During the recording period of the temporary seismic network deployed to study the dynamics of the hybrid system of LUSI, Mt. Bromo entered into an eruptive period, from the end of 2015 to early 2016. The volcanic activity attracted the attention of scientists like Sukir et al. (2017) in order to study the eruptive period with seismic recordings from February of 2016.

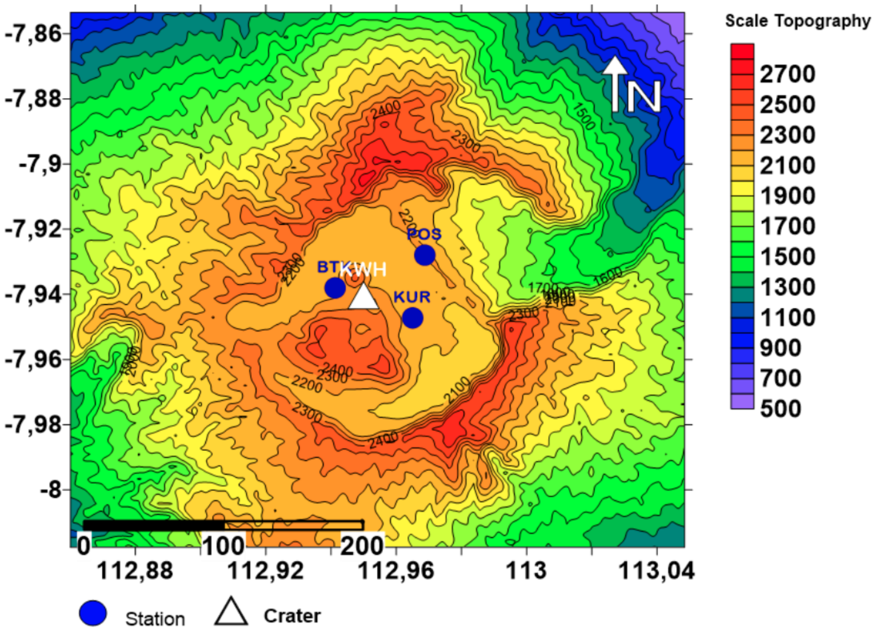

Figure 3.3: The temporary seismic network used by Sukir et al. (2017). It consisted on 3 multi-component stations: BTK, KUR and POS. *From Sukir et al. (2017).*

To locate the events, the authors used a temporary seismic network consisting of 3 multi-component stations of broad-band type (ID codes: BTK, KUR and POS), located at the top of Mt. Bromo (see Figure 3.3). The data recorded consist on continuous tremors, with a coherent dominant frequency above 5 Hz, and across the stations (see Figure 3.4a). For the location of the events, the authors adopted a polarization analysis method applied to instances of the continuous tremor in the 3 components. They retrieved the back-azimuth and incidence angle and used them to locate the events. The location method consisted on interpolating the back-azimuths of the different stations to estimate the epicenters, and then using the incidence angles to calculate source depths. The Figure 3.4b illustrates the location approach, and shows several assumptions made by the authors: 1) a straight ray-path from source to stations (homogeneous medium), and 2) discard of topographic effects.

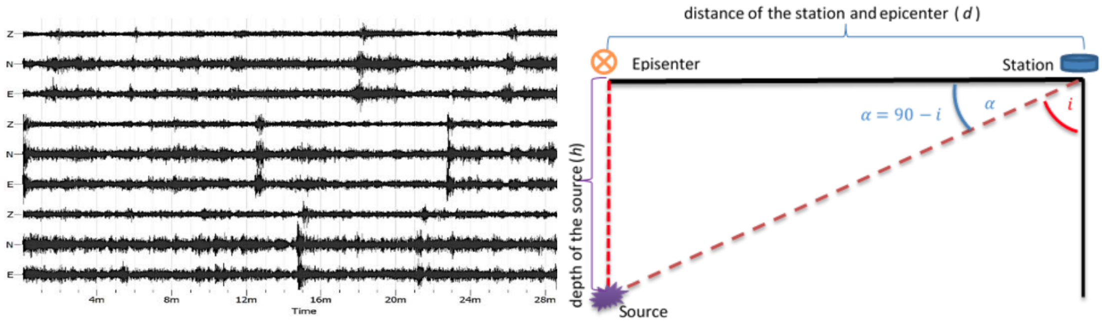

(a)

(b)

Figure 3.4: (a): Continuous tremors spotted by the station BTK. (b): Location method used by Sukir et al. (2017) to locate the tremors. *From Sukir et al. (2017).*

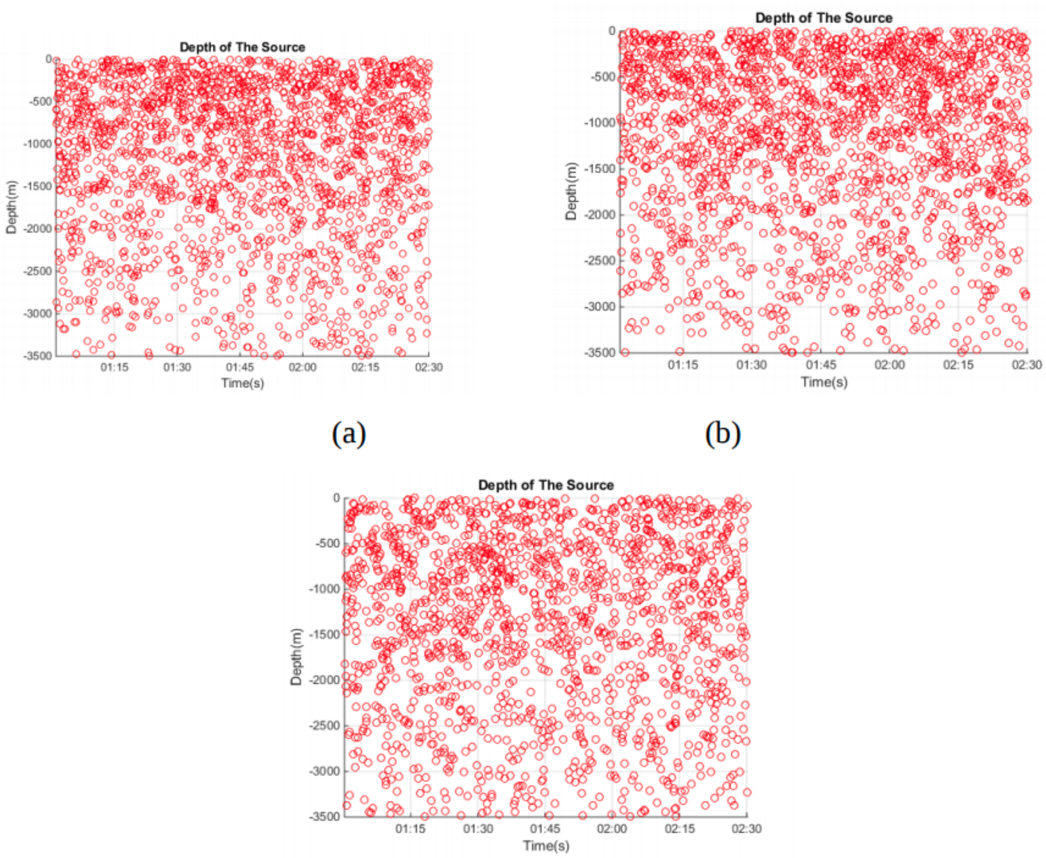

(a)

(b)

(c)

Figure 3.5: Tremor locations beneath Mt. Bromo, achieved with incidence angle and back-azimuth intersections at stations: a) BTK, b) KUR, and c) POS. *From Sukir et al. (2017).*

Sukir et al. (2017) present the results of the location as shown in Figure 3.5, where the depth varies with time. They concludes that the source moved up the surface with time. Also, the characterize the events based on 4 types tremor source mechanisms: 1) fluid flow, 2) fluid discharge through cracks, 3) hydrothermal boiling system, and 4) resonance from the large magma volume (Konstantinou and Schlindwein, 2003; Maryanto et al., 2008; Sukir et al., 2017).

The temporary network deployed to study LUSI covers a time ranging 2 years period (2015-2016), and so it gives an opportunity to study the events produced from Mt. Bromo's eruptions. Minetto et al. (2019) approach this opportunity in order to identify the eruption on the records of the LUSI LAB stations, only using the vertical channels. For this study case, the temporary network have a bath azimuthal coverage around Mt. Bromo, and so they extended the network by adding 3 more stations around Mt. Bromo, part of the permanent network from the Meteorological, Climatological, and Geophysical Agency of Indonesia (BMKG) (see Figure 3.6).

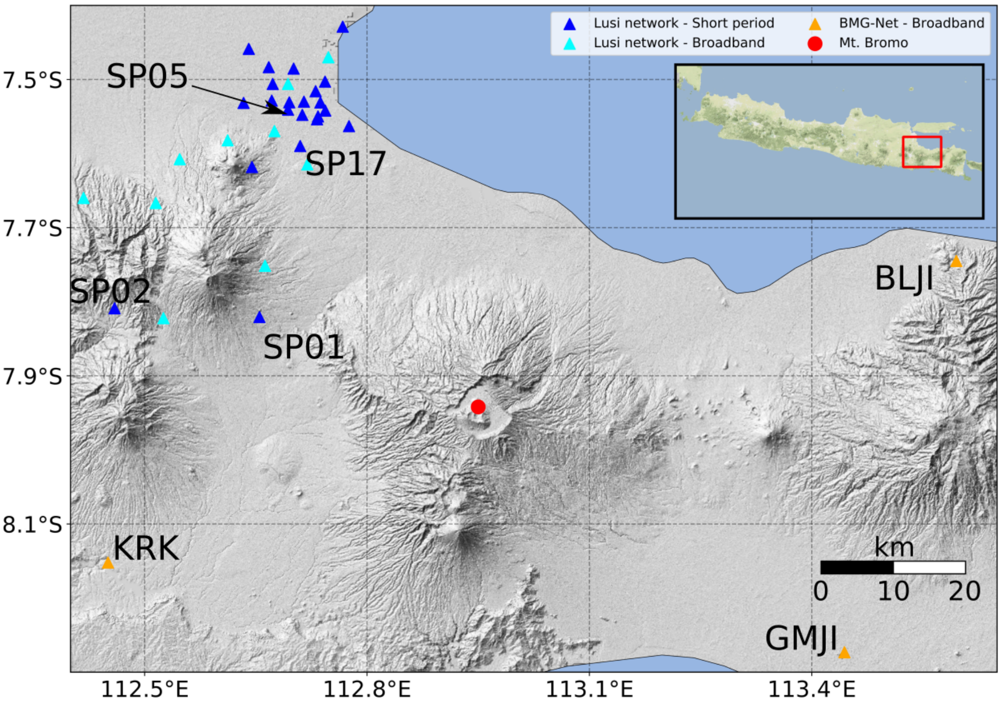

Figure 3.6: The seismic network configuration used by Minetto et al. (2019). It consisted on 7 multi-component stations; 4 from the temporary LUSI LAB network, and 3 from the permanent BMKG network. *From Minetto et al. (2019).*

In the records, Minetto et al. (2019) found sustained low frequency signals in several stations, mostly during the 2 years of data, and to research for these, they used some of the stations installed on bedrock (in AW), which had the best S/N ratios (Minetto et al., 2019).

Results based on frequency analysis showed mainly two types of low frequency sustained events inside a signal with its energy concentrated between 0.1 to 2 Hz range (see Figure 3.7; left side). The first type of events were named Type A: a distinguished fragmented tremor, of 2 minutes of duration, occurring every 5 minutes, with frequency ranges between 0.7 and 2.0 Hz. The second event was named Type B: a continuous tremor from end of October 2015 to mid January 2016, in a frequency range between 0.2 to 0.8 Hz, with high peaks of recurrence in certain periods (see Figure 3.7; right side). According to Minetto et al. (2019), recognizing the Type A events was difficult due to the presence of events Type B.

Then based on their frequency content, the authors established detection algorithm triggers for it to create templates from only one station, and find similar signals in other stations by the use of template

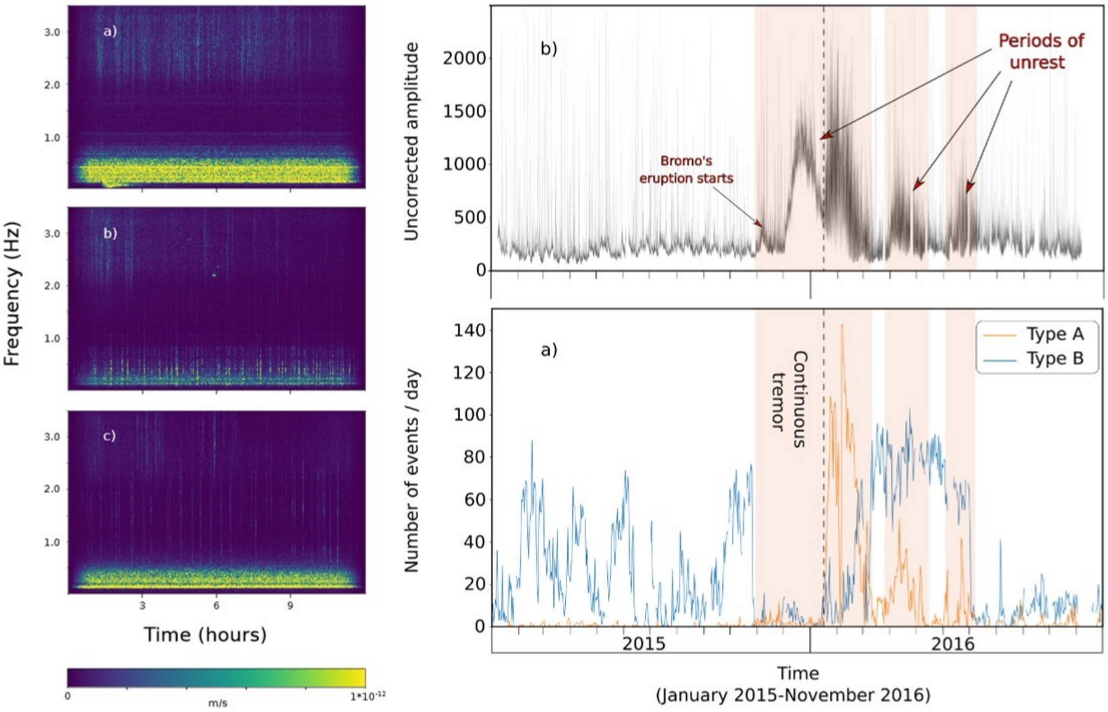

Figure 3.7: (Left): Spectrograms from continuous tremors. Type A and Type B events can be seen as the two lowers, respectively. The low frequency energy ambient noise partially overlaps with Types A and B events. (Right): (Top) Maximum amplitude of events every 15 minutes. (Bottom) Number of events Type A and B recorder daily. Unrest volcanic periods of Bromo reported from direct observations are highlighted in the red areas. The vertical dashed line marked the change in the eruption style, which coincides with the transition of number of events from Type B to Type A. *From Minetto et al. (2019).*

matching. For detecting the 2 types of events, the authors proposed two types of band-pass filters; from 0.7 to 1.7 Hz, and from 0.3 to 0.9 Hz. Finally, it was set the location of the events through a 2D grid-search cross-correlation (CC) method from the (Ballmer et al., 2013; Droznin et al., 2015). The method of Ballmer et al. (2013) and Droznin et al. (2015) consists on making station-pair CC between waveform envelopes in order to achieve the time-differences between signals, and use this to do a 2D-grid search for the possible source location. This needs then to test different constant velocities. This means that there was an assumption of the events to be surface waves, with straight paths. Using this approach it was also found that the events from Type B came mainly from Mt. Bromo volcano (see Figure 2.4), using a constant surface velocity of 1.35 Km/s, and it is mention that Type A comes from the volcano, however there is no report from it.

Despite the used surface velocity, some other signals picked up during the study suggested an apparent velocity between stations SP01 and SP02 of 3.3 Km/s (distance of 20 Km, signal time-delay of around 6 seconds) (see stations in Figure 3.6). This could imply two possible options: 1) the surface velocity could be higher and then location could achieve at a higher quality, or 2) there are some signals of the same nature that do not correspond to shallow sources at Mt. Bromo, but deeper. While Type B was continuous and present along the recording period, Type A events were consistent with Mt. Bromo eruption periods (see Figure 3.7; right).

The work done by Sukir et al. (2017) and Minetto et al. (2019) showed 2 ways to determine the detections and locate them. However, in both studies the authors assumed to have surface waves, as they locate in an scenario without heterogeneity. It is possible that some tremors could have emergent arrivals, and clear P-waves that could also be used. Due to the convergent tectonic environment and Minetto et al. (2019) findings, it is possible that some of the tremors could come from other deeper sources such as magmatic chambers, Moho's discontinuity, or subduction slabs. Since this has effects on the location, then this aspect will be handled in this work by attempting a location of these events in 3D (latitude, longitude and depth).

CHAPTER 4

Framework and Theory

4.1 Automatic Detection Methods

In ObsPy and in the literature there are several detection (trigger/picker) algorithms or methods which consists of the construction of a characteristic function from continuous recordings, and afterwards setting on it values that would work as Triggers On and Off to mark the start and the end of an event, respectively.

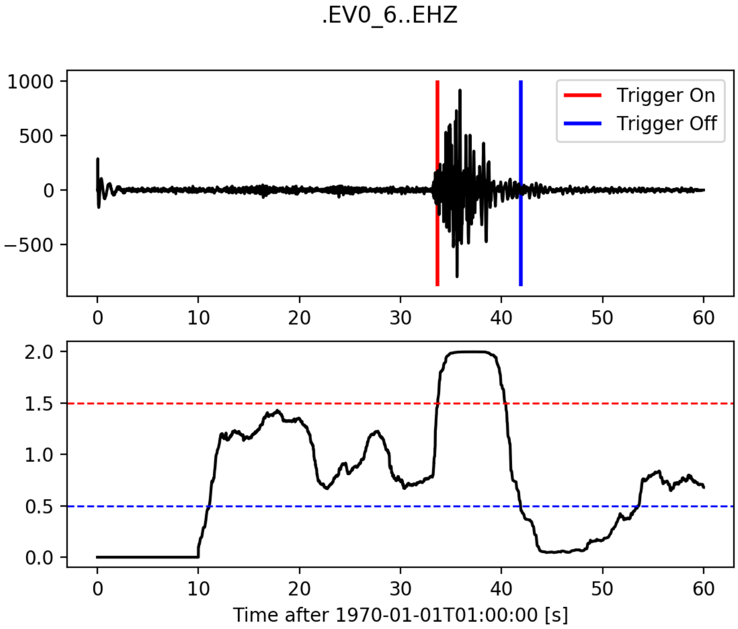

Figure 4.1: Example of the STA/LTA detection, taken from ObsPy Tutorial (Beyreuther et al., 2010). (Top): Normal seismic event recorded in a signal. (Bottom): Characteristic function from STA/LTA algorithm. The red and blue horizontal lines indicate the Trigger-On and Trigger-Off to detect the event.

The most broadly used detection method in earthquake processing routines, specially for weak-motion seismology, is the Short-Time Average through Long-Time Average (STA/LTA) (Trnkoczy, 2009), also called Classical STA/LTA due to the other variations that comes from it (Beyreuther et al., 2010). This method consists on creating a characteristic function based on calculating the ratio between average values of the squared amplitudes of a signal from 2 consecutive time-windows in movement (Trnkoczy, 2009). The following equation shows the formula for the short and long time-window value for a given data point in time x_i (Withers et al., 1998):

$$\begin{aligned} STA_i &= STA_{i-1} + \frac{x_i^2 - x_{i-N_{STA}}^2}{N_{STA}}, \\ LTA_i &= LTA_{i-1} + \frac{x_{i-N_{STA}-1}^2 - x_{i-N_{STA}-N_{LTA}-1}^2}{N_{LTA}} \end{aligned} \tag{4.1}$$

where N_{STA} and N_{LTA} are the number of points on each window (Withers et al., 1998), but this can be translated to a STA or LTA time-range as $N = Tf_s$, where f_s is the sampling frequency of the instrument and T is the time-window (Beyreuther et al., 2010).

The 2 time-windows should be defined by the user and the result of the calculation sliding through the signal in time is referred as the characteristic function of the signal (Trnkoczy, 2009; Beyreuther et al., 2010). The Figure 4.1 illustrates an example taken from ObsPy tutorial (Beyreuther et al., 2010) for a very well defined seismic event.

According to Trnkoczy (2009), a good choosing of the STA and LTA lengths is based on the duration of the observed events and the background noise behavior. The STA window must be shorter than the total duration of the signal to detect, and its range depends on the interest of detection; just the first-arrival of the signal, or more phases besides this. The LTA window must be longer than the signal duration in interest, so there is a good capture of the background behavior, and then be able to differentiate the noise from the signal amplitudes. Both the STA and LTA windows must be chosen in a way that avoids sensibility to background noise, allowing the highest possible number of real detections and minimizing the false ones, part of the background noise.

Based on the produced characteristic function, two values are set to work as Trigger-On and Trigger-Off (Trnkoczy, 2009; Beyreuther et al., 2010). Once the curve of the characteristic function is above one defined value (see Figure 4.1, red line), the Trigger-On is activated, meaning the arrival/start of an event. Afterwards, if the characteristic function descends below another defined value (see Figure 4.1, blue line), then a Trigger-Off is activated, meaning that the event has passed or has ended. This is the dynamic of the Trigger-On and Trigger-Off values which defines a time-window where an event is being detected (Trnkoczy, 2009).

There are other methods which are modified versions of the Classical STA/LTA as an attempt to solve certain limitations of the original one. One of these is the Recursive STA/LTA, which intends to avoid keeping a long data vector in memory when processing time-large recordings, and thus more computer efficient (Withers et al., 1998). It produces in the characteristic function an impulse response and an exponential decay that recovers more quickly from large energy transients instead of rectangular impulses as the Classic STA/LTA (Withers et al., 1998). This is achieved with the following equation:

$$\begin{aligned} STA_i &= Cx_i + (1 - C)STA_{i-1}, \\ LTA_i &= Cx_i + (1 - C)LTA_{i-1} \end{aligned} \tag{4.2}$$

with $C = 1 - e^{-S/T}$, where S is the seconds per sample and T is the characteristic decay time; the time required for the impulse response to decay at $1/e$ of its original value (Withers et al., 1998). Notice that when $C = 1/N_{STA}$ and $C = 1/N_{LTA}$, it leads back to Equation 4.1. As an addition, the recursive method also handles "shadow zones", meaning that after a large transient passes the STA value, the transient continues to dominate the output by causing a large LTA value (Withers et al., 1998).

Another variation of the Classic STA/LTA is the Delayed STA/LTA, which was designed to achieve a better statistical independence between the short and long time-windows by separating them with a delay time (Withers et al., 1998). It allows shorter time-windows and consequently produces a quick recovery from transients, however, short windows produce great variability in the STA/LTA value c(Withers et al., 1998). Its respond to the background noise is not as smooth as the Recursive STA/LTA and requires computing capabilities for a fast performance (Sya'bani et al., 2020).

There is another detection method with a more distant approach than the STA/LTA series, which is called the Z-Detector, developed by Swindell and Snell (1977). According to Sharma et al. (2010), the Z-Detector algorithm is based on the following equation:

$$Z = \frac{X_n - \overline{X}}{\sigma} \tag{4.3}$$

where X_n is the sum of the current n values of the STA window, $\overline{X}$ is the mean of the values involved in X_n, and σ is the standard deviation of the values in the same time-window (Sharma et al., 2010).

The main advantage of this method is that it has an adaptive adjustment to background noise level an automatic adjustment to variance in the background noise (Withers et al., 1998; Sharma et al., 2010). If this noise variance is small, then a small change in the input is required for a large change in output, and so large inputs are required for a large change in output (Withers et al., 1998). As a disadvantage, the method does not enhance the ability of detecting phases after the main P-wave arrival in order to set the Trigger-Off in the seismic record system (Sharma et al., 2010).

4.2 Polarization Analysis

The polarization analysis is a quantitative approach that process the signals from 3-component instruments, as it records the particle motion during seismic phases, and extracts or enhances their polarization content (Jurkevics, 1988). A method to do this is based on implementing a Principal Component Analysis (PCA) through the construction of a covariance matrix (Lois et al., 2013):

$$C = \begin{bmatrix} \sigma_{zz} & \sigma_{zn} & \sigma_{ze} \\ \sigma_{nz} & \sigma_{nn} & \sigma_{ne} \\ \sigma_{ez} & \sigma_{en} & \sigma_{ee} \end{bmatrix} \tag{4.4}$$

for a Principal Component Analysis (PCA). The components $\sigma_{i,j}$ inside the covariance matrix C represents the zero-mean cross-power between the traces on the i and j channels Z, N and E. This is simply:

$$\sigma_{ij} = \frac{1}{N} \int_{t_0}^{t_f} s_i sj, \tag{4.5}$$

where s_i and s_j are the filtered and normalized traces in the different components, t_0 and t_f are the time before and after the first-arrival pick that conforms the waveform window in interest, and N is the number of points in the window, dependent from the sampling frequency (Walck and Chael, 1991; Lois et al., 2013).

To determine the principal directions of the space described by C, and thus the direction of maximum variances, the covariance matrix C must be rotated until it turns into a matrix with its eigenvalues $\lambda = \{\lambda_1, \lambda_2, \lambda_3\}$ occupying the diagonal spaces and zero value on the rest of the positions, the diagonal matrix C' (Walck and Chael, 1991). The values of λ can be obtained by taking the determinant of $(C - \lambda I)$ and solving the characteristic polynomial of C. The eigenvectors $\vec{u}$, product of the diagonalization of C, represents an orthonormal base of the 3D space and form the ellipsoid (polarization ellipsoid) that best fits to the data in a least-square sense (Lois et al., 2013), and its relation is expressed as the follow:

$$(C - \lambda I)\vec{u} = 0 \tag{4.6}$$

where I is the identity matrix of the same size as C, and 0 is the zero vector (Lois et al., 2013). By here, it is clear then that the eigenvectors $\vec{u} = \{u_1, u_2, u_3\}$ can be determined by solving the Equation 4.6. The polarization geometry is then explained to be an ellipsoid in 3D space (N, E and Z) that encloses the particle motion path, and is described by 3 orthonormal vectors (eigenvectors) (Jurkevics, 1988). These vectors represent the maximum direction of variance from the particle trajectory data, and so, they are the main axes of the ellipsoid (Jurkevics, 1988). The eigenvalues represent the magnitude of the main axes of the ellipsoid, and then it describes the elongation and roundness of the geometry (Jurkevics, 1988). A quantified description of the ellipsoid, as it is the eigenvalues and eigenvectors, leads to the determination of the main directions that describes the particle motion (Lois et al., 2013).

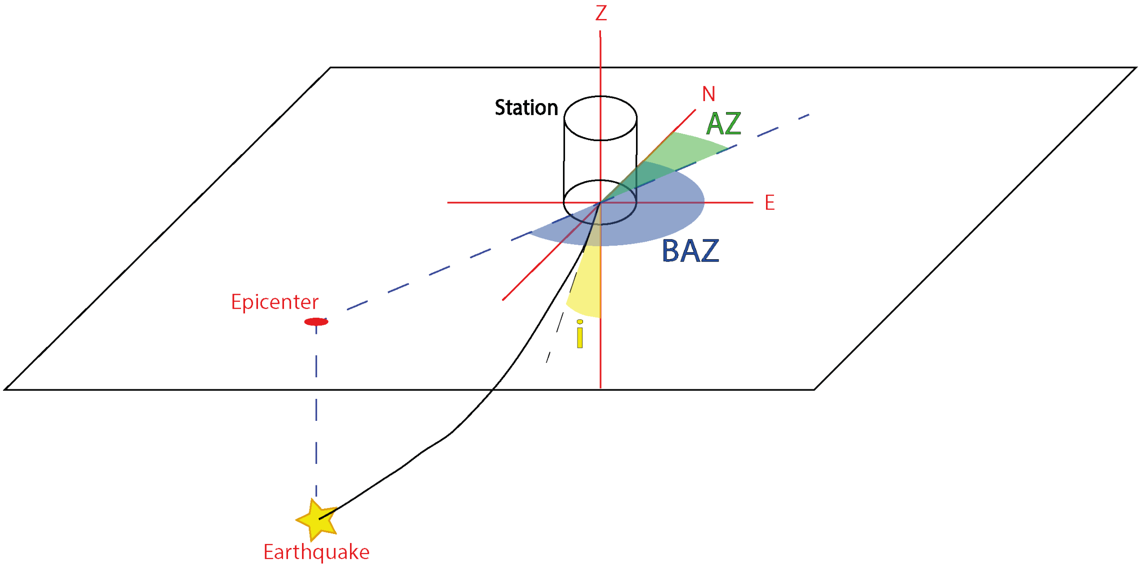

Figure 4.2: Illustration of angles describing the direction arrival of a traveling ray originated from a seismic event. i = incidence angle, AZ = azimuth angle, BAZ = back-azimuth angle.

Using the eigenvalues and eigenvectors retrieved from the PCA, the polarization is able to retrieve the azimuth, back-azimuth, and incidence angle describing the particle motion. Azimuth is understood as the azimuthal direction of the particle movement, and the Back-Azimuth is understood as the opposite direction, describing the direction from where the motion comes (Lois et al., 2013). The Incidence-Angle describes the direction of particle movement in relation to the vertical direction (see Figure 4.2) (Lois et al., 2013).

If $\vec{u}_{ij}$ is the eigenvector, with $i = 1, 2, 3$ being the 3 components Z, N and E, and $j = 1, 2, 3$ the 3 direction cosines, then the first-arrival azimuth can be obtained by:

$$Azimuth = \tan^{-1}\left(\frac{\vec{u}_{1,2}}{\vec{u}_{1,3}}\right) \tag{4.7}$$

and their back-azimuth is the same value with an addition of 180°. If the value overpasses 360°, then the same last value is extracted to the calculation. Finally, for the incident angle of the particle motion, it is described as:

$$Incidence = \cos^{-1}(|\vec{u}_{1,1}|) \tag{4.8}$$

Aside from these parameters, the rectilinearity and planarity are values that can also be extracted from the polarization analysis. Rectilinearity refers to the property that states how the particle motion is limited in a straight line (Kumar et al., 2019). In that sense, is a measure of how linearly the wave field is polarized, and thus, it measures the degree of linear polarization for a 3-component seismic signal (Kumar et al., 2019). On the other hand, Planarity refers to the distribution of energy and the degree of polarization within a chosen time-window (Kumar et al., 2019). Jurkevics (1988) explains this better as the ability of the particle motion to describe an elliptical trajectory, and thus, to the path being confined to a plane in the 3D space.

According to (Jurkevics, 1988), if the eigenvalues are arranged from largest to smallest ($\lambda_1 \geq \lambda_2 \geq \lambda_3$), then the rectilinearity of the particle motion can be given by the following relation:

$$Rectilinearity = 1 - \frac{\lambda_2 + \lambda_3}{2\lambda_1} \tag{4.9}$$

which is expected to be close to 1.0 for P and S phases, while the planarity of the particle motion is given by:

$$Planarity = 1 - \frac{2\lambda_3}{\lambda_1 + \lambda_2} \tag{4.10}$$

which is expected to be close to 0.0 for P arrivals and close to 1.0 for S arrivals (Lois et al., 2013). Nevertheless, the assumption for the S-wave phases is valid for isotropic mediums (Eisner et al., 2009). The cases are mostly imperfect, and thus, Jurkevics (1988) states that pure body waves achieve Rectilinearity values close to 1.0 when there is one nonzero eigenvalue. As for Planarity, it will be close to 1.0 for Rayleigh-wave motion as the particle trajectory is elliptical and confined into a plane (Jurkevics, 1988).

4.3 Linear Inversion method for Earthquake Location

In an homogeneous medium with a constant velocity v of a given wave type (normally P-wave), the arrival time of the wave to a location $X = (x, y, z)$, from a seismic source located at $X_0 = (x_0, y_0, z_0)$ which occurred at a time t_0 is:

$$t_{arr} = t_0 + \frac{1}{v}[(x - x_0)^2 + (y - y_0)^2 + (z - z_0)^2]^{\frac{1}{2}} \tag{4.11}$$

assuming the seismic ray travel path is straight (Karasözen and Karasözen, 2020). If the velocity varies with space $v(x)$, then the arrival time is expressed as an integration along the seismic ray path S:

$$t_{arr} = t_0 + \int_{r_0} u(r_0)d(s) \tag{4.12}$$

where $u(x)$ is the slowness of the medium and $r_0(s)$ is a point at distance s along the seismic ray path r between X_0 and X (Karasözen and Karasözen, 2020).

When there is multiple observations of arrival times at different N stations, then they can be represented as a vector containing the observed arrival times on each station (Karasözen and Karasözen, 2020):

$$d_{obs} = (t^1_{arr}, t^2_{arr}, ..., t^N_{arr})^T \tag{4.13}$$

The spatial (x, y, z) coordinates and origin time t of the seismic event are the model parameters and can be represented as a model vector $m = (x, y, z, t)^T$. Finally, both Eqs. 4.11 and 4.12 can be written as:

$$d_{obs} = g(m) \tag{4.14}$$

where $g(m)$ is a non-linear function that could predict the arrival times for a given $m(x, y, z, t)$ (Karasözen and Karasözen, 2020). Notice the 4 variables are part of the model and 4 variable must be solved to describe the location of an earthquake. In linearized problems, it is required ≥ 4 arrivals picked to solve the 4 variables of the m (Stein and Wysession, 2009).

All deterministic location problems are based on linearized inversion, which was introduced by Geiger (1912), which starts with an initial guess $m_0 = (x_0, y_0, z_0, t_0)^T$, and takes into consideration the difference on arrival times between an ideal model d_{pre}, and the observed d_{obs}, giving then $\delta d = d_{obs} - d_{pre}$ (Karasözen and Karasözen, 2020). Then for a number of N arrivals observed and $M \leq 4$ model parameters, the linear problem can be written and solved through least squares:

$$\delta d = G \delta m \tag{4.15}$$

$$\delta m_{est} = (G^T G)^{-1} G^T \delta d \tag{4.16}$$

where G contains the partial derivatives of the N arrivals respect to the model parameters, and $G^{\dagger} = (G^T G)^{-1}$ is the Moore-Penrose inverse of G. At the end the basis of the earthquake location inversion methods consist on doing a forward model with a pre-known velocity model and compare the results of arrival times calculated with the observed ones (Stein and Wysession, 2009; Karasözen and Karasözen, 2020). The model with the least difference compared to the observations is assumed to be the solution (Stein and Wysession, 2009; Karasözen and Karasözen, 2020).

4.4 Probabilistic Functions for Earthquake Location

Most earthquake location algorithms already implement error functions to evaluate the possible earthquake location; either by computing the Root Mean Square (RMS) from theoretical and observed arrival-times differences, or as a PDF using the same differences of arrival-times. One of the most used PDF's is the Likelihood Function (Karasözen and Karasözen, 2020), such as the Least-Squares L2 norm likelihood function (LS-L2):

$$pdf(x, t_0) \propto k \exp\left[-\frac{1}{2} \sum_{obs_i} \frac{[T_{obs_i}(x) - T_{calc_i}(x)]^2}{\sigma_i^2}\right] \tag{4.17}$$

where x is a point in 3D space, t_0 is an estimate of the origin time, k is a normalization factor, T_{obs_i} and T_{calc_i} are the observed and calculated arrival times, respectively, and σ_i is the assigned error for obs_i (Lomax, 2004). The LS-L2 function is sensitive to outliers, and the maximum likelihood point can be strongly biased by outliers in the data (Lomax, 2004). Based on this, the Equal Differential Time (EDT) likelihood function was proposed to overcome the limitations of the LS-L2 function. It is based on the LS-L2 function and also from station-pair time differences. The EDT is expressed as:

$$pdf(x, t_0) \propto k \left[\sum_{obs_a, obs_b} \frac{1}{\sqrt{\sigma_a^2 + \sigma_b^2}} \exp\left(-\frac{[T_{obs_a}(x) - T_{obs_b}(x) - T_{calc_a}(x) - T_{calc_b}(x)]^2}{\sigma_a^2 + \sigma_b^2}\right)\right]^N \tag{4.18}$$

where T_{obs_a} and T_{obs_b} are the observed arrival times, and T_{calc_a} and T_{calc_b} are the calculated travel times, respectively, for two observations (obs_a and obs_b) (Lomax, 2004). The sum is taken over all possible pairs of observations, and N is the total number of observations (Lomax, 2004). Since the sum of observations is done outside the exponential, the function has its maximum value on the points x where most pairs of observations are satisfied, decreasing the sensitivity to outliers data (Lomax, 2004).

4.5 The Oct-Tree Search method for Hypocenters

The Oct-Tree Importance Sampling is a grid-search method for hypocenter locations, which which recursively involves subdivisions and samplings in 3D space to generate a cascade of sampling cells (Lomax, 2004).

First, the method established a fixed grid volume in X,Y and Z (north, east, depth) was define to search for the possible solutions of the earthquakes. This is defined as the initial location grid. Each of the points of the initial grid location correspond to an hypothetical hypocenter, from where arrival-times to each station are calculated (Lomax, 2004), and also corresponds to a PDF evaluated in that point, based on the misfit between the observed arrival-times and the calculated ones (Lomax, 2004).

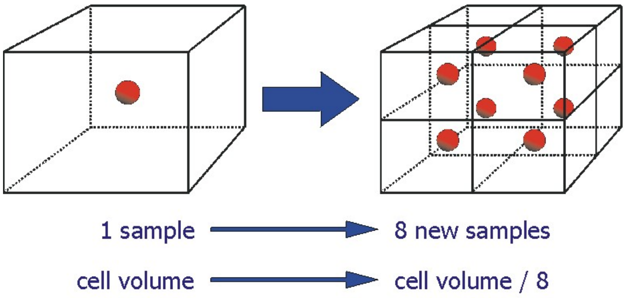

Figure 4.3: Example of the first step in the recursive subdivision of the Oct-Tree earthquake search method. The cell with the maximum EDT value from the initial location grid is subdivided into 2x2x2 grids (location search grid). The same method then is applied to the sub-cell with the maximum EDT value with the same subdivisions established. *Taken from NonLinLoc webpage (Lomax, 2004).*

Once the initial location grid points have their respective probability value, the volume cell containing the point with the maximum value is selected (Lomax, 2004). The recursive subdivision is then applied to this cell with a defined grid which would be the location search grid, and the process of mapping the EDT in the subdivided cell volume, and recurrent subdivisions are made until a defined number of evaluated points or resolution is reached (see Figure 4.3) (Lomax, 2004). The point of the subdivisions at the end with the highest EDT value is meant to be the most accurate earthquake location (Lomax, 2004).

CHAPTER 5

Data

5.1 Network

The Figure 5.1 shows the configuration and location of all the different stations used in this study; deployed and active from January 2015 to December 2016 (Fallahi et al., 2017; Mazzini, 2018; Obermann et al., 2018; Minetto et al., 2019). They consist on a total of 36 stations; 10 broad-band stations of Guralp CMG-3T 120s sensors in combination with EarthData (ED) loggers sampling at 100 Hz, 22 short-period stations (18 Lennartz LE-3Dlite Mk II 1s sensors in combination with Nanometrics TAURUS loggers sampling at 100 and 250 Hz, 5 Mark L-4-3D 1s sensors with ED loggers sampling at 200 Hz), and 3 broad-band permanent stations of STS-2 120s sensors sampling at 20 Hz from the IA Indonesian Seismic Network (IA), BMKG (Centre, 1993; Minetto et al., 2019). All of the stations record in North, East and Vertical channels. From now on, they will be referred as N, E and Z, respectively.

The position of the stations where designed in order to cover mostly the LUSI area, the proximate Penanggungan and AW volcanic complex, and their connection between them through the Watukosek fault zone (see Figure 5.1 and 5.2) (Karyono et al., 2015; Fallahi et al., 2017; Obermann et al., 2018). However, this study is aware of the limitations that such configuration represents in terms of coverage, since there can be also other tectonic elements that might affect the data, such as local tectonics (fault and fractures), regional events (plate interactions and subduction zones), and volcanic events. The last one is the one with the more influence, since in this area there are many active volcanoes as shown in Figure 2.4, specially Bromo, as pointed out by Minetto et al. (2019).

In order to assess the problem, the stations KRK, GMJI and BLJI from the BMKG were added to the network to increase the covered area, and increase depth resolution. The main advantage of these stations are that they are located in bedrock sites since they are near volcanic buildings (see Figure 5.1). Due to their sampling frequency of 20 Hz, these stations are not able to detect short-period events as the other ones. Then it is expected that the high-frequency content from the events originated at near volcanoes would not be noticed in these stations, but only the low-frequency ones; as the survive longer travel-distances since the earth works as a low-pass filter (Stein and Wysession, 2009).

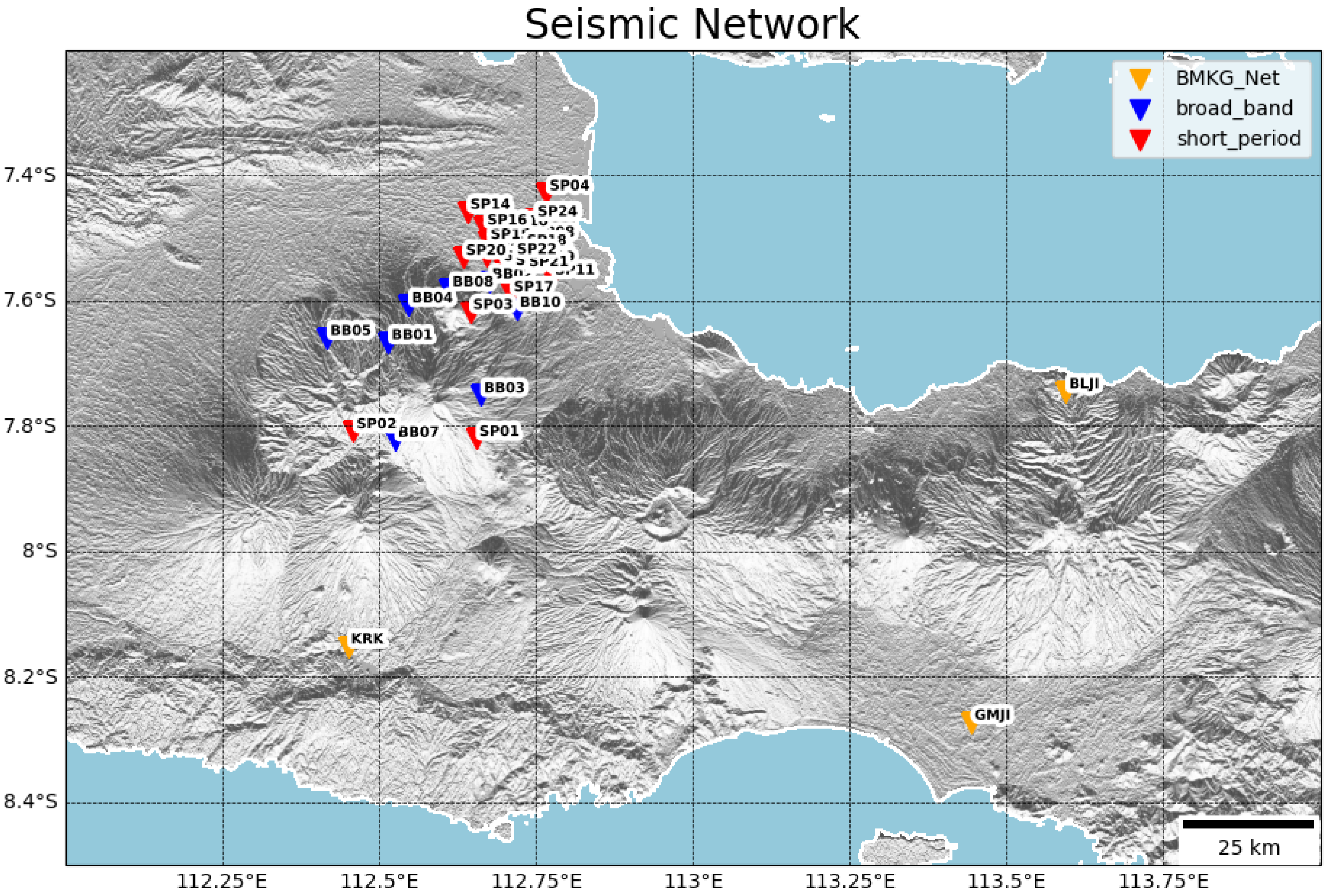

Figure 5.1: Stations available. The colors differentiate between the Short-Period stations, the Broad-Band stations, and the Broad-Band permanent stations from the BMKG.

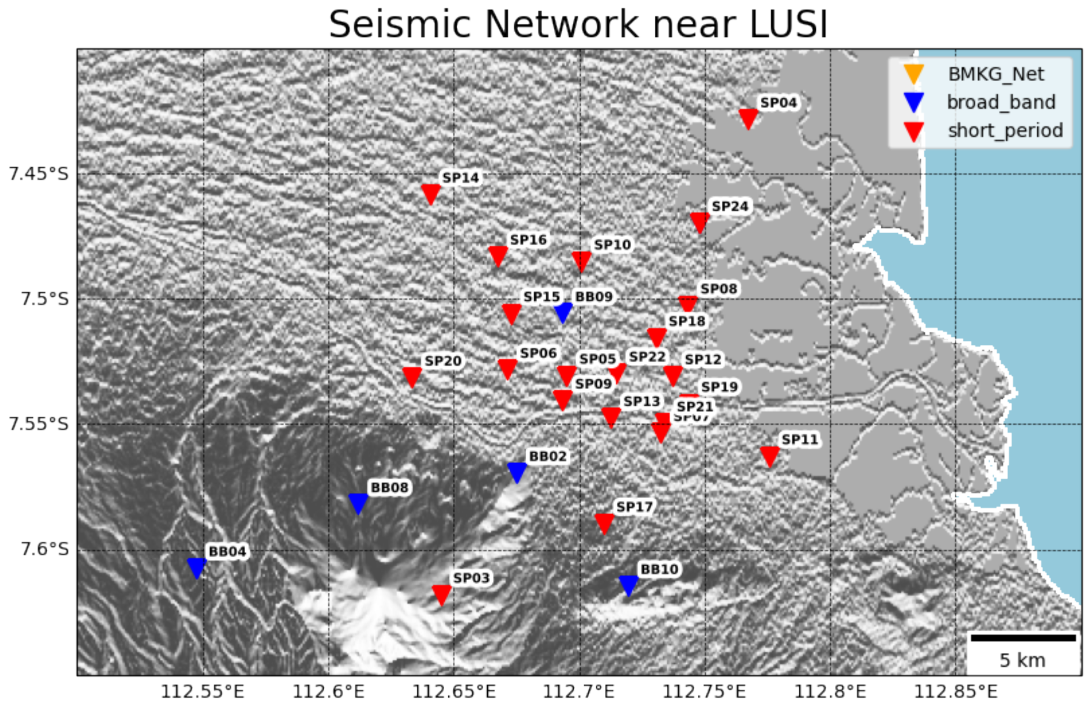

Figure 5.2: Zoom into the LUSI site from Figure 5.1. The station locations around LUSI are displayed in detail.

5.2 Seismic recordings: Format and Status

The data used in this study consists on continuous seismological recordings from the stations mentioned in this chapter. The data is handled as miniSEED files, one for each station channel. Each file consists of one entire day of recording at the sampling frequency of each station, and since each station is triaxial, then it is expected normally to have at least 3 recordings of 24 hours long each station, and per day. Some of the stations presents recordings even from before January 2015 or after December 2016, specially the BMKG permanent stations.

The dataset present certain features that represent challenges on how the dataset must be addressed, such as interruptions in the recordings, continuous ambient and instrumental noise (also pointed by Obermann et al. (2018) and Karyono et al. (2015)). The interruption time ranges were very variable, meaning that some stations lost recordings from a period of hours to days. In the last case, this supposed that miniSEED files were not produced by a station in those dates. Also it represents logistic problems regarding relocation of stations as SP07 for SP24, maintenance, and others. An important notation is that not all the stations started or concluded their operations at the same time, meaning some stations have more recordings than others.

Regarding the ones from the BMKG permanent network, they only present recordings in the vertical (Z) channel in 2014. The North (N) and East (E) components (horizontal) are available from January 2015, at least on station KRK. However, the availability of the horizontal components is not continuous as the stations presents then several interruptions in the data, malfunctioning, and high noise in most of the recording period.

Based on the mentioned aspects, and for the purpose of this work, only the period from January 2015 to December 2016 (2 years) was used in this study, leaving out existing data from before and after the mentioned period.

CHAPTER 6

Methodology

This work was done by creating functions and scripts in Python 3.7 language code (Millman and Aivazis, 2011) to build an automatic earthquake processing routine program that could be capable of achieving the goals of this work, managing wave files, proceed according to recording to available data and gaps.

Several python packages were used, however, ObsPy was the most important (Beyreuther et al., 2010). This package is a group of seismological processing tools already programmed to address different waveform file formats, network databases, waveform analysis, and others (Beyreuther et al., 2010). Nevertheless, each problem represents specific challenges that ObsPy tools can not solve completely, and thus it depends on the user to choose the best functions to address the challenges that the work represents.

Most of the processing applied in this work required a loop; scanning day by day, from the start date until the end date of all the files involved in the study period (2015-01-01 to 2016-12-31). A processing for one single day already represents a challenge in computation time, and the calculations must be interrupted between the methods described in the following sections, with the objective to check and validate the outputs. To address this, the loop was parallelized by using several nodes and cores simultaneously to accelerate the process. Each core received an entire day to process, so that several days were processed simultaneously. If one of the cores finished the processing routines for an assigned day, then the core will be assigned to process the next day in the queue of the loop. This is a dynamic approach which implies that the cores can work independently, without the need to wait for every core to end their process. The selection of cores and nodes were entirely dependent on the supercomputer resources and the jobs queue from other users.

6.1 Data inspection

The following step was crucial since this determined the methods to use for the earthquake routine processing. Part of the inspection was to check gaps in the recordings, instrumental noise, spikes, and others as told in Chapter 5. Nevertheless, the main feature to assess was to inspect some of the observed events and their frequency content, duration, and amplitudes. For this, certain stations were selected since most of them present poor S/N ratio as pointed by Minetto et al. (2019), and also checked in this study.

The first approach was to check the recordings through simple seismograph plots in order to assess if there is any filtering needed before running the detection code. Stations like SP01 and SP02 present signals with a good S/N ratio, and so they are optimal for inspecting the type of signals recorded. Several random days were chosen to try to spot any events and plot spectrograms to explore their frequency content. A priority was given to certain time periods related to maximum volcanic activity, pointed by Minetto et al. (2019).

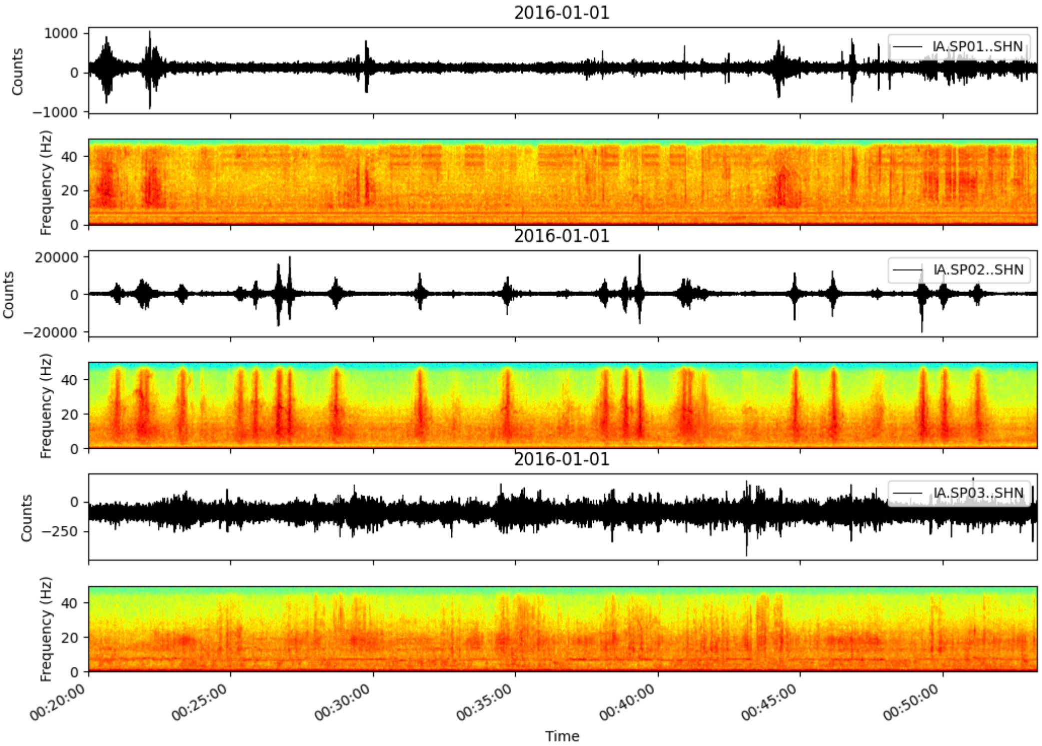

Figure 6.1: Seismographs and spectrograms from 2016-01-01 (year-month-day) for N components of stations SP01, SP02 and SP03, sliced in time between 00:20:00 and 01:00:00 UTC. Events present in this moment have high frequency content ranging mostly from 10 to 40 Hz.

The Figure 6.1 shows an example of 40 minutes of data for stations SP01, SP02, and SP03 and its spectrograms. As observed, the main frequency content of the observed events range mostly from 10 to 40 Hz. The stations SP01 and SP02 show this well, however, the station SP03 seemed at this date to have some instrumental noise since the signals frequency content is not well defined as in SP02. On the other hand, SP01 shows defined events by amplitude as frequency content, even if there is presence of ambient noise with a large frequency range (see Figure 6.1).

A similar behavior happens with stations in the basin around LUSI (LUSI stations), but with subtle differences. The Figure 6.2 illustrates an example with LUSI stations SP19, SP10, and SP09. The frequency content of the recorded events are similar to short-period stations installed on bedrock; some ranging from 10 to 20 Hz, and others ranging from even lower frequencies (5 Hz) to higher than 20 Hz. A continuous signal bellow 5 Hz is pointed by the spectrograms. This could be the anthropogenic noise pointed by Obermann et al. (2018); between 2 and 3 Hz.

Something important to notice from Figure 6.1 and Figure 6.2 is that, despite of the clear high-frequency signals observed, they are not common between the stations. This means that their arrivals cannot be related or associated to singular events.

In contrast to the stations seen before, the permanent stations (BMKG) are not able to capture high-frequency events, but rather low-frequency ones. This is mostly due to the stations sampling frequency of 20 Hz. The BMKG stations and also other bedrock stations, as the ones installed around AW, share common arrivals from signals with frequency content ranging mostly from 1 to 10 Hz. As an example, the Figure 6.4 shows several tectonic events spotted in KRK, BLJI (BMKG) and BB05 (AW) stations. Here, the duration of each event do not extend more than 10 minutes, and their frequency content can slightly go over 10 Hz (see BB05 frequency content at Figure 6.4). However, this kind of events are not easily spotted by basin stations at LUSI (see Figure 6.3).

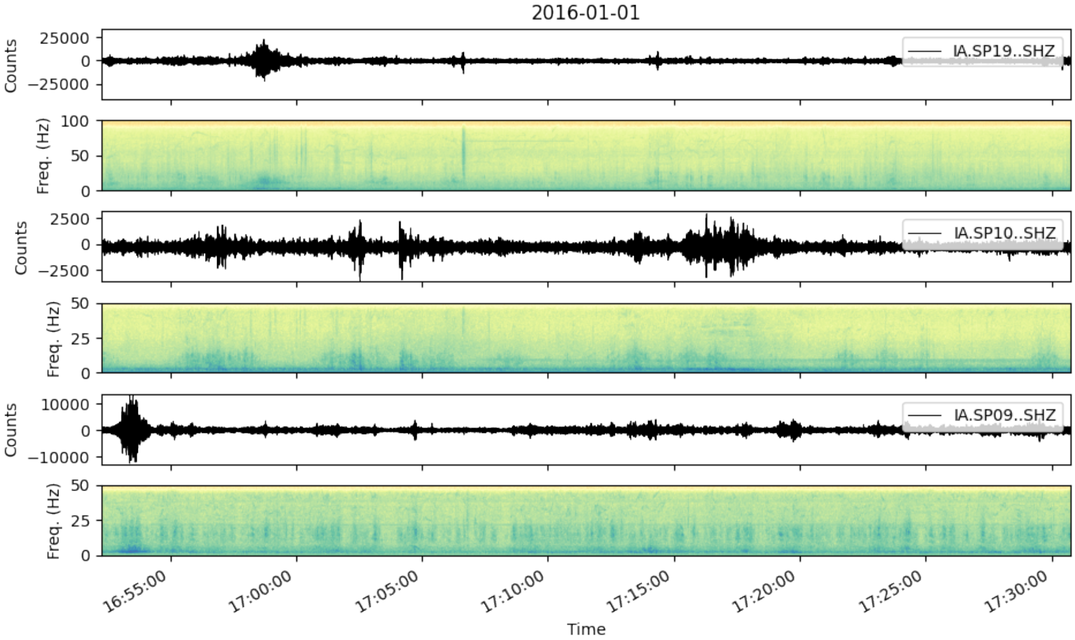

Figure 6.2: Seismographs and spectrograms from 2016-01-01 (year-month-day) for Z components of stations SP19, SP10 and SP09, sliced in time between 16:40:00 and 17:30:10 UTC. The frequency content of the events are similar to short-period stations. A continuous signal bellow 5 Hz is present in instruments located in basins, possibly by anthropogenic noise pointed by Obermann et al. (2018).

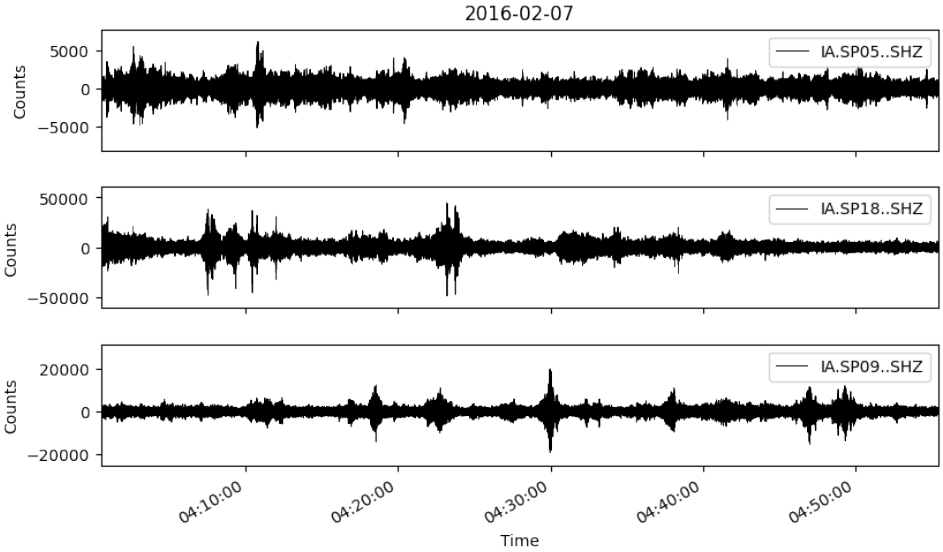

Figure 6.3: Seismographs from 2016-02-07 (year-month-day) for Z components of basin stations (LUSI) SP05, SP18 and SP09, filtered between 1 to 10 Hz, and sliced in time between 04:00:00 and 05:55:00 UTC. Signals are mixed with high-frequency events that underpass below 10 Hz and don not allow any recognition of common signals between the stations.

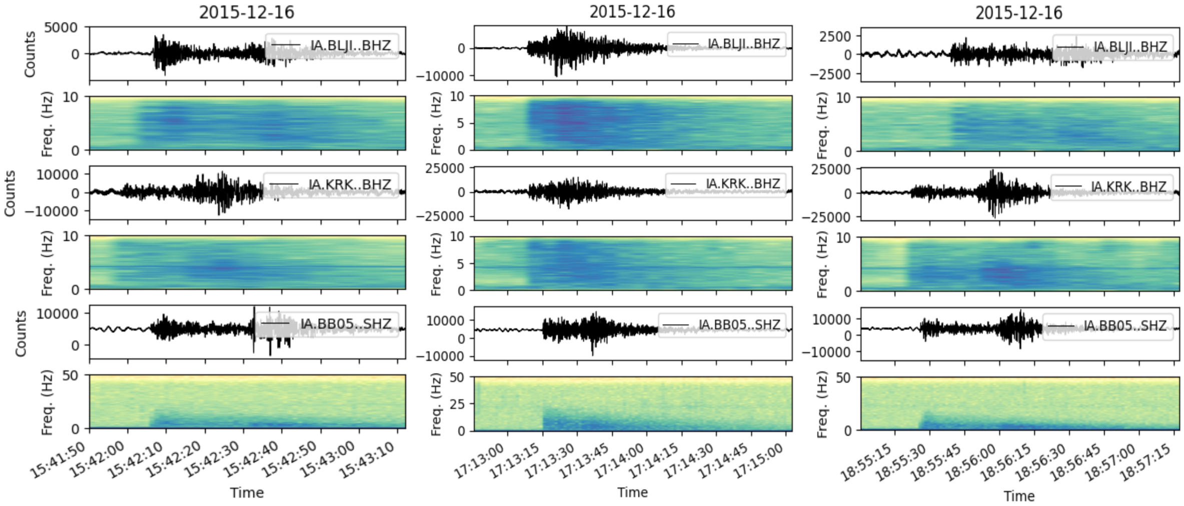

Figure 6.4: Seismographs and spectrograms from 2015-12-16 (year-month-day) for Z components of permanent broad-band stations BLJI and KRK, in comparison with the temporal short-period station BB05, sliced in time between 15:30:00 and 19:05:00 UTC. Three tectonic events are spotted in the stations due to the low-frequency content.

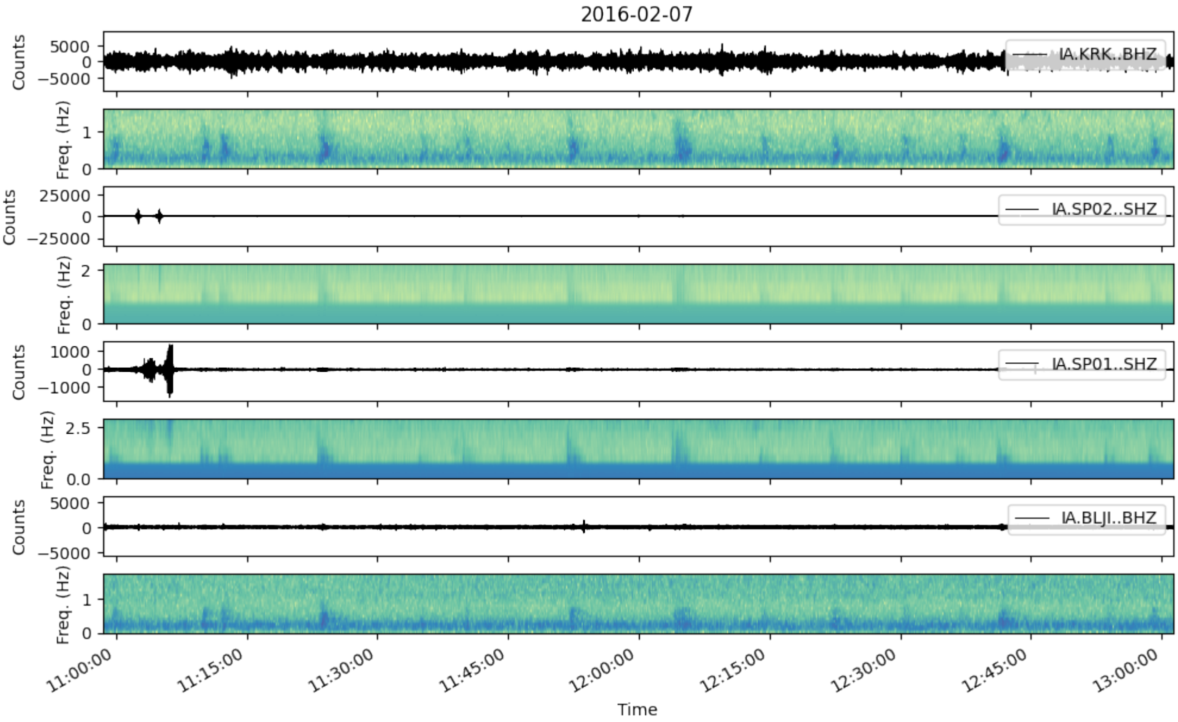

Figure 6.5: Seismographs and spectrograms from 2016-02-07 (year-month-day) for Z components of stations KRK, SP02, SP01 and BLJI, sliced in time between 11:00:00 and 13:01:00 UTC. Spectrograms spotted common signals in all stations with frequencies between 0.3 and 1.5, and not easily shown by the seismographs.

Finally, some events hidden in the time domain but clear in spectrograms below 2 Hz can be visualized in the spectrograms of stations installed on bedrock (AW and permanent BMKG stations). Some of them are tectonic seismic activity as the ones in Figure 6.4, and teleseismic events with a duration longer than 30 minutes. However, the stations installed on bedrock (AW and BMKG) are able to spot common signals, ranging in 0.3 to 1.5 Hz in frequency content. The Figure 6.5 is able to show these signals, not observed on the time domain, but they are clear on the frequency domain. Also, it illustrates that these events have a duration of maximum 2 minutes, with variations, and they occur repetitively; each 5 to 15 minutes. Their visualization in time domain of these events was achieved by filtering between 0.3 and 1.5 Hz (see Figure 6.6). Also another continuous signal is present with lower amplitude than the repetitive events mentioned. The frequency content of the repetitive signals also overlaps with the continuous signal (0.3 to 0.7 Hz). Below 0.3 Hz there is presence of instrumental noise that lasts for days, and above 1.5 Hz the anthropogenic noise starts to appear, mostly in the AW stations. The characteristics of these repetitive signals falls into the same ones described as Type A by Minetto et al. (2019), which are the fragmented tremor signals.

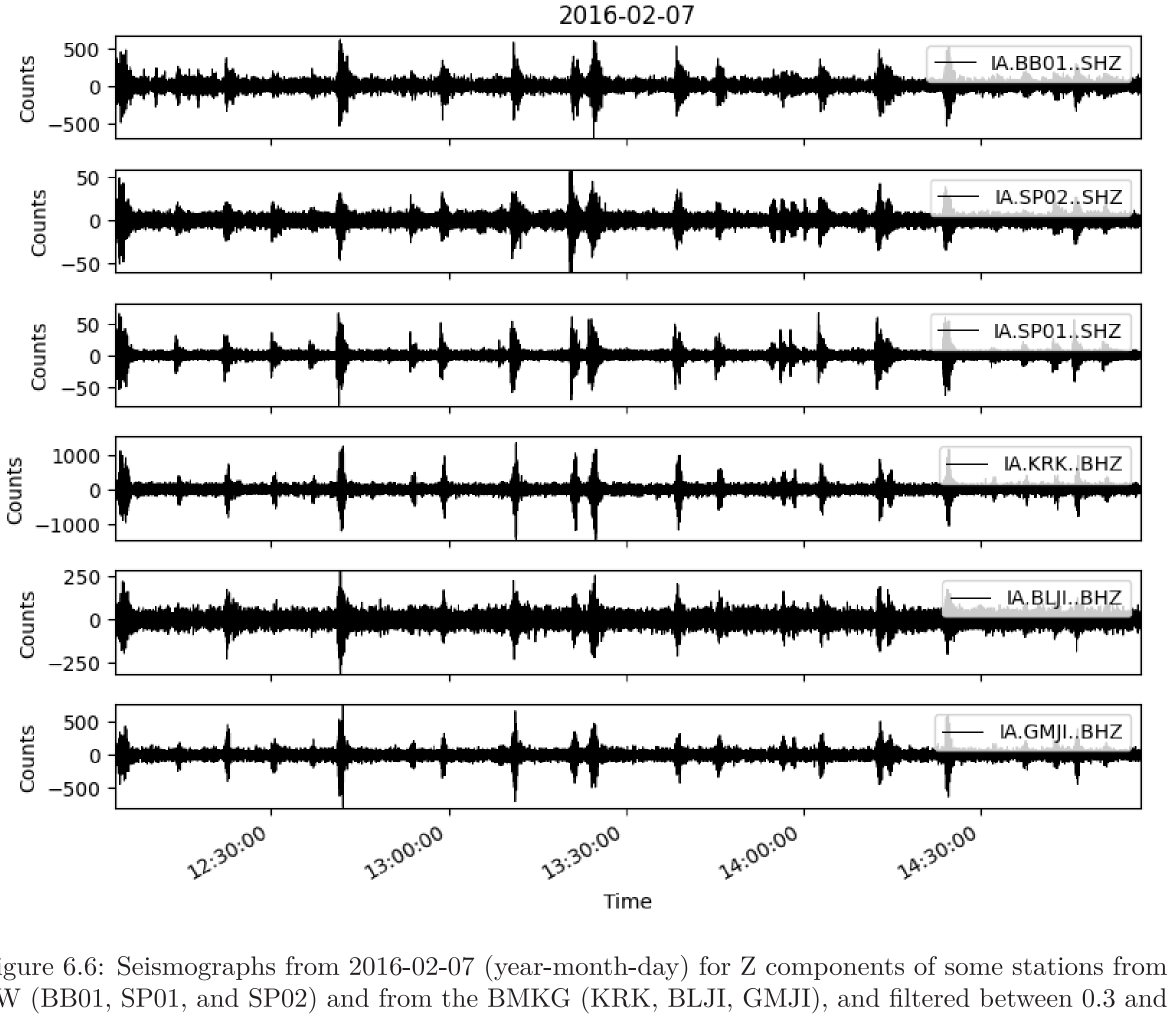

Figure 6.6: Seismographs from 2016-02-07 (year-month-day) for Z components of some stations from AW (BB01, SP01, and SP02) and from the BMKG (KRK, BLJI, GMJI), and filtered between 0.3 and 1.5 Hz. Signals in this frequency band are common between bedrock stations.

6.2 Network Batches

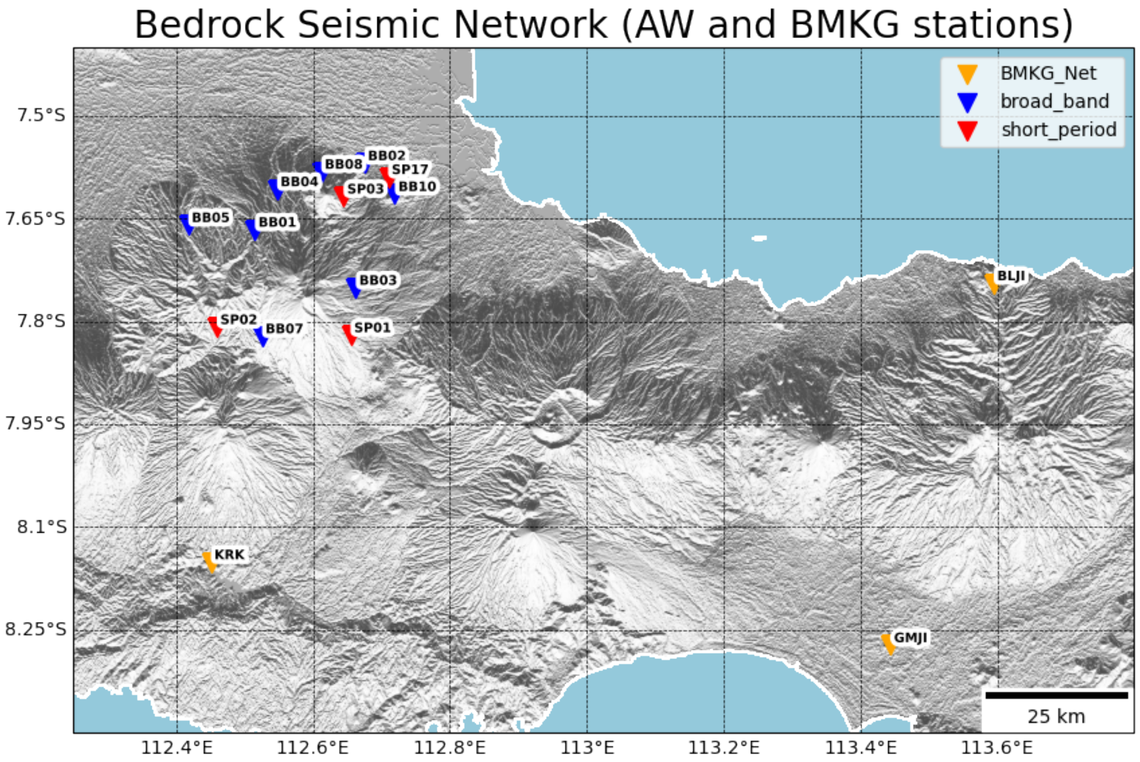

Figure 6.7: Stations available. The colors differentiate between the Short-Period temporal stations, the Broad-Band temporal stations, and the Broad-Band permanent stations from the BMKG.

Based on the data exploration, only the bedrock stations show signals common between them, in the 0.3-1.5 Hz and 1-10 Hz frequency ranges (see Figures 6.6 and 6.4). The basin stations that monitored LUSI do not show common signals between the stations that can be simply associated in any of the frequency spectrum or ranges explored. Based on this, and because they provide a bad coverage on the area, these stations were then discarded. Then, only stations installed on bedrock were selected as the final network to use; the ones at the AW volcanic complex and the permanent stations of the BMKG (see figure 6.7). From now on, the new network configuration will be mentioned as the Bedrock Network.

6.3 Detection

Once the data inspection was applied for several random days with different stations, the next step was to construct a detection algorithm that makes use of all the components available from each station on the Bedrock network. For this purpose, first it was explored which known detection method works best for single component data, and then it was proposed how to extend this into an all the components in order to achieve a final multi-component detection algorithm.

In several seismic processing routines is normal to enhance the data by applying filters, which is part of the pre-processing (Havskov and Alguacil, 2004; Zhang et al., 2019). Based on the data inspection, and to validate the multi-component detection method, 3 frequency bands were used as pre-filters: 1) a 10-40 Hz which covers the signals found by LUSI and AW stations, 2) a 1-10 Hz covering mostly tectonic seismic events, and 3) a 0.3-1.7 Hz which covers the tremor signals. The last pre-filter was chosen, even if it included the continuous signal, since the part of the information of the tremor signals also occurs in the frequency range of the continuous one.

For BMKG stations, the Nyquist frequency value is the half of the sampling value ($f_{Nq} = 10$ Hz), meaning they can not record high-frequency events without presenting aliasing (Stein and Wysession, 2009). So by choosing a top frequency of 10 Hz, the number 9.95 Hz instead of 10 Hz was used in order to avoid numerical problems. However, for simplicity in future mentions this value is referred as 10 Hz on the rest of the text.

Detection Algorithm

In this work, each of the 4 detection methods explained in Chapter 4 were evaluated in order to establish the method with best performance in each of the cases (pre-filter bands), and use this criteria to chose for the best method on the frequency band of interest (0.3-1.5 Hz). To achieve this, different trade-off's of time-window values for STA and LTA had to be tried out for each detection method, in order to accomplish the best characteristic function that could describe the transient behavior of the events in interest (for each frequency band) and discard the remain ambient noise presented after pre-filters (Trnkoczy, 2009). Afterwards, Trigger-On and Trigger-Off values were set to a proportion that could be optimal for detecting as much clear events as possible with a near pick of the first-arrival, while discarding most of the instrument peaks and ambient noise signals. All channels were used to find a consistency in the pickings. However, a special attention was set on the Z channels, as they mostly showed the lower amplitudes.

The detection algorithm performances were evaluated by selecting a 24-hours recordings from a station component with the highest S/N ratio or with the biggest amplitudes recorded from most of the events in a time range. The features to evaluate were the computing time, the sensibility to false detections as ambient noise or instrumental noise spikes, the complexity on the parameters selection (trade-off), and the result of the event windows. The last point is meant to describe the best approximation of the P-wave first arrival and the end of the event signal.

The Table 6.1 shows an summary of the best parameters for each detection method when applicable in a pre-filtered band, and the Figures 6.8, 6.9 and 6.10 shows the visual performance of each of the detection methods in the pre-filtered tested bands, with the use of the best parameters for each one.

Table 6.1: Detection methods tested for each pre-filter band and the selected optimal parameters for each parameters to achieve best detection results. The Recursive STA/LTA performed was chosen as the best detection method for both bands.

Pre-Filter Band (Hz)	**Method**	**Parameters**	**Best Method Result**
0.3 - 1.5	Classic STA/LTA	STA (sec): 5 LTA (sec): 1000 Trigger-On: 3.0 Trigger-Off: 1.0	**Recursive STA/LTA**
	Recursive STA/LTA	STA (sec): 10 LTA (sec): 1000 Trigger-On: 1.0 Trigger-Off: 0.5	
	Delayed STA/LTA	STA (sec): 5 LTA (sec): 10 Trigger-On: 2.0003 Trigger-Off: 2.00002	
	Z-Detect	STA (sec): 10 Trigger-On: -0.02 Trigger-Off: -0.027	
1 - 10	Classic STA/LTA	STA (sec): 5 LTA (sec): 1000 Trigger-On: 5.7 Trigger-Off: 1.0	**Recursive STA/LTA**
	Recursive STA/LTA	STA (sec): 5 LTA (sec): 1000 Trigger-On: 4.0 Trigger-Off: 0.9	
	Delayed STA/LTA	STA (sec): 5 LTA (sec): 10 Trigger-On: 2.001 Trigger-Off: 2.0009	
	Z-Detect	STA (sec): 10 Trigger-On: 0.08 Trigger-Off: 0.07	
10 - 40	Classic STA/LTA	STA (sec): 7 LTA (sec): 100 Trigger-On: 2.7 Trigger-Off: 0.9	**Recursive STA/LTA**
	Recursive STA/LTA	STA (sec): 10 LTA (sec): 100 Trigger-On: 2.2 Trigger-Off: 0.9	
	Delayed STA/LTA	STA (sec): 5 LTA (sec): 10 Trigger-On: 2.05 Trigger-Off: 2.0	
	Z-Detect	STA (sec): 7 Trigger-On: 0.39 Trigger-Off: 0.1	

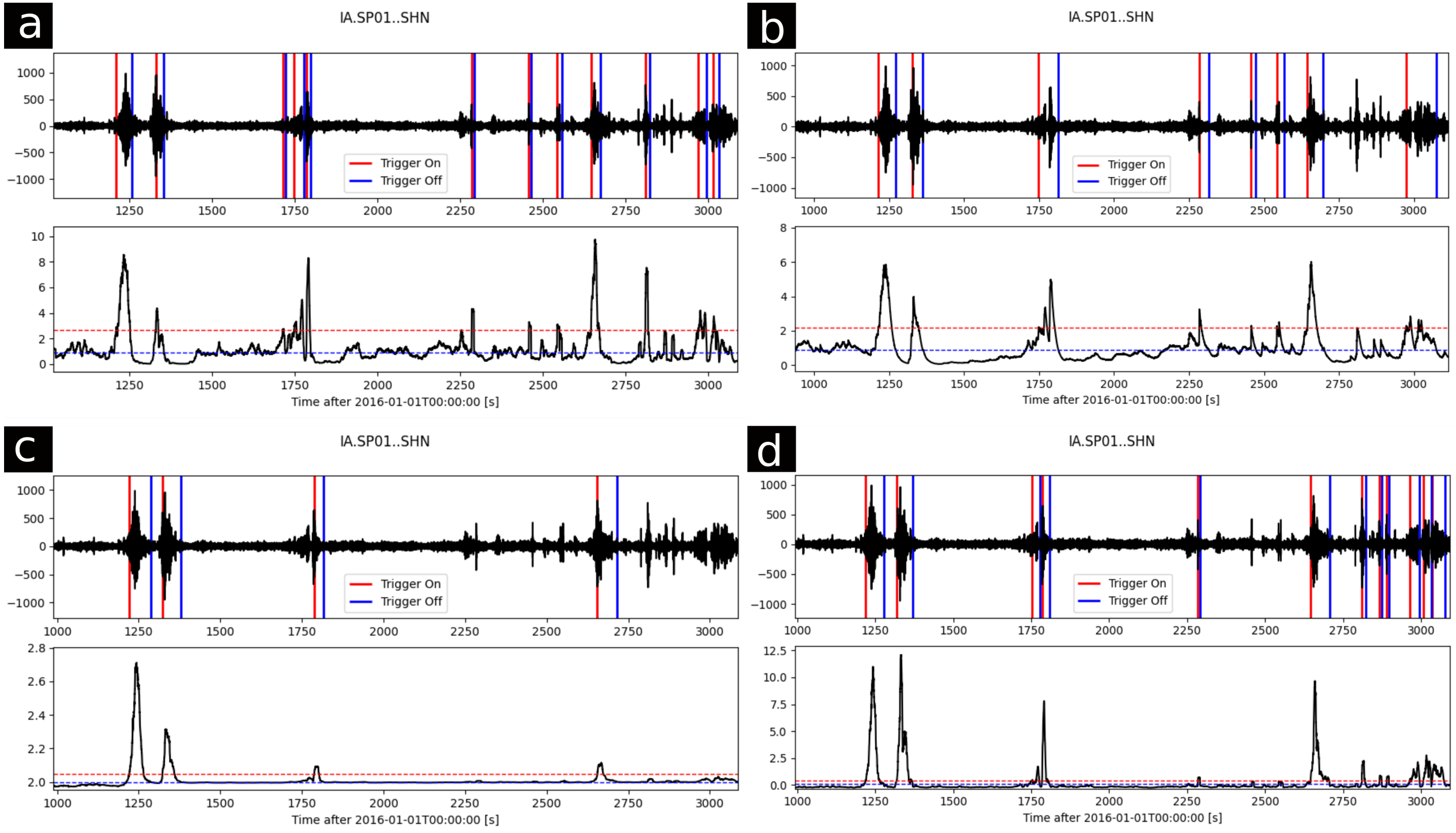

Figure 6.8: (Top of each image) Recordings of station SP01 on 2016-01-01 (year-month-day) on similar time slices with the detection performance from the tested methods. (Bottom of each image) Characteristic function from each tested method with the Trigger-On and Trigger-Off values (red and blue dashed lines). Pre-filter band used: 10-40 Hz. Parameters used are stated in Table 6.1. a) Classic STA/LTA, b) Recursive STA/LTA, c) Delayed STA/LTA, d) Z-Detect.

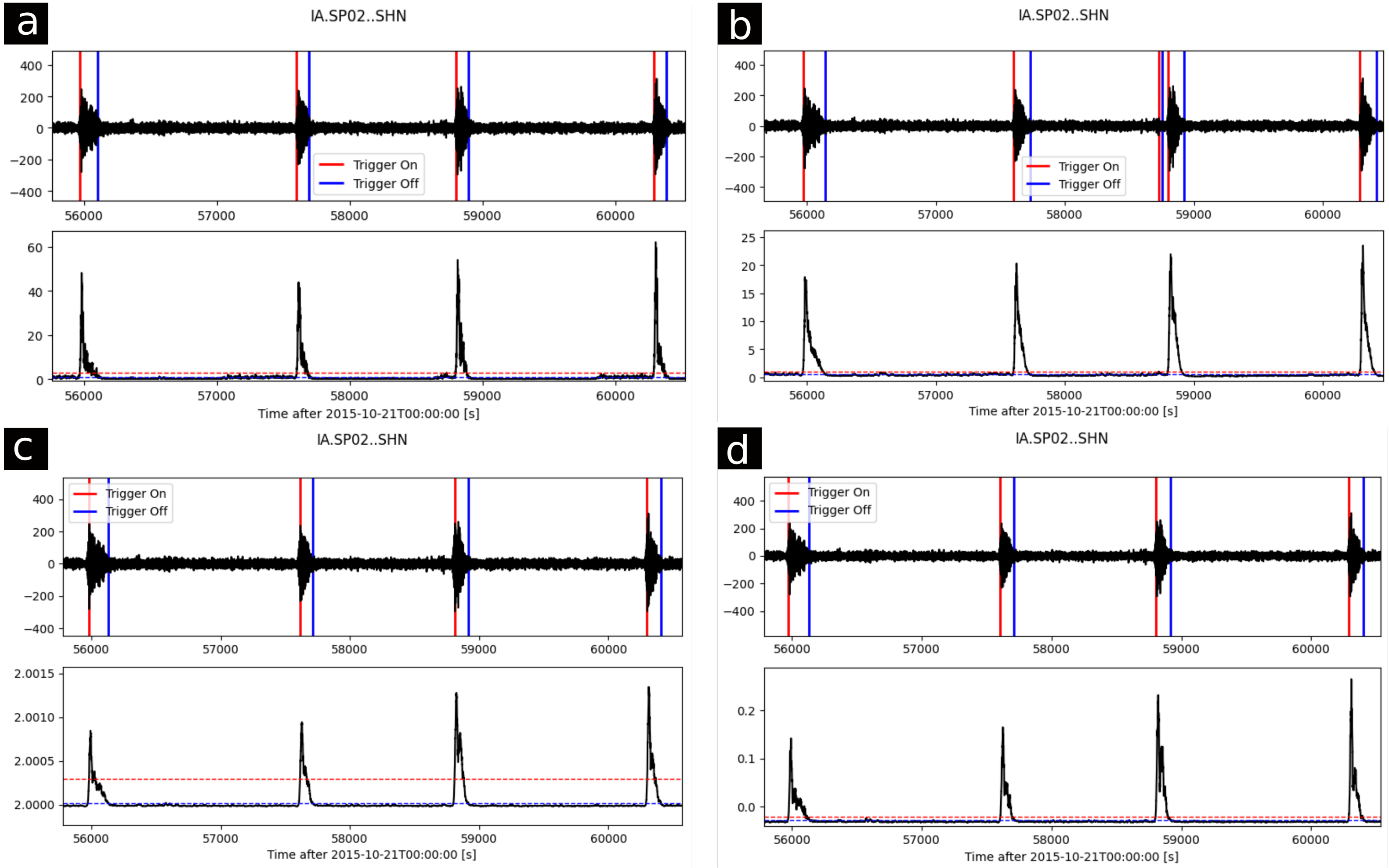

Figure 6.9: (Top of each image) Recordings of station BB05 on 2015-12-16 (year-month-day) on similar time slices with the detection performance from the tested methods. (Bottom of each image) Characteristic function from each tested method with the Trigger-On and Trigger-Off values (red and blue dashed lines). Pre-filter band used: 1-10 Hz. Parameters used are stated in Table 6.1. a) Classic STA/LTA, b) Recursive STA/LTA, c) Delayed STA/LTA, d) Z-Detect.

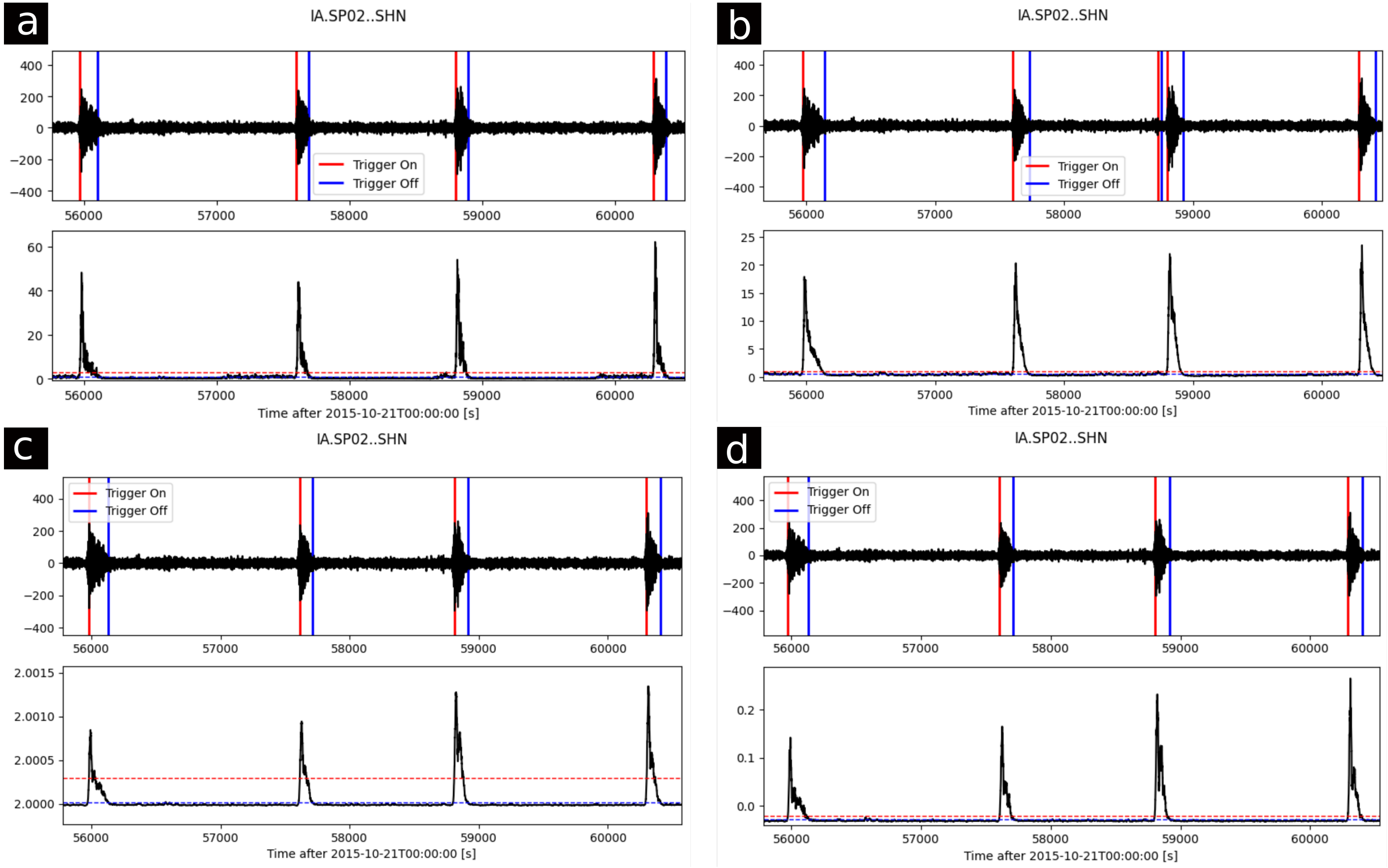

Figure 6.10: (Top of each image) Recordings of station SP02 on 2015-10-21 (year-month-day) on similar time slices with the detection performance from the tested methods. (Bottom of each image) Characteristic function from each tested method with the Trigger-On and Trigger-Off values (red and blue dashed lines). Pre-filter band used: 0.3-1.5 Hz. Parameters used are stated in Table 6.1. a) Classic STA/LTA, b) Recursive STA/LTA, c) Delayed STA/LTA, d) Z-Detect.

In all of them, the Recursive STA/LTA showed high sensibility towards the detection of the emergent signals while avoiding noise, and made faster detections than the other methods. The other algorithms (Classical STA/LTA, Delayed STA/LTA, and Z-Detect) showed in their characteristic function (see Figures 6.8, 6.9 and 6.10) a more symmetrical shape when describing the emergent signals on the time-domain. This aspect forced a choosing of very close Trigger-On and Trigger-Off values in an attempt to extract the best representation of the event window with the best possible P-wave arrival-time, however, it also was reflected into more false detections. On the other hand, the Recursive STA/LTA provided quick impulses in the characteristic function at the beginning of each emergent signal, and also a slow decay after the impulses. This aspect allowed an easy Trigger-On and Trigger-Off values selection. For all these motives, the Recursive STA/LTA was selected as the detection method.

Once the Recursive STA/LTA method was selected in accordance with its variables (STA time, LTA time, Trigger-On and Trigger-Off), then a multi-component coincidence trigger method was implemented. This was made in an attempt to integrate the selected detection method with all the available components of an instrument, and set unique start and end times of the signals detected.

Multi-Component Coincidence Trigger (MCCT)

There are situations where, depending on the location of the earthquake, 1 or 2 channels from the N, E and Z components might have recorded the event better than the other components. Based on the data inspection step, it was common to see enhanced signals in the horizontal components, rather than in Z; as most of the micro-seismic activity is superficial (Fallahi et al., 2017; Obermann et al., 2018). This could lead to a case where the detection method might not operate well when applied only to the Z channel, as it was the case of Minetto et al. (2019), when it comes to detecting superficial events. In order to overcome this problem and in an attempt to integrate all the available components of the stations, a Multi-Component Coincidence Trigger algorithm (MCCT) was designed with the use of the coincidence-trigger function from Obspy (Beyreuther et al., 2010). The purpose then is to integrate the individual detections across the different channels of a station in order to increase the number of detections, filter noise pickings, and improving the start-time picks (first P-wave arrival-time).

The method first make individual detections on each channel from a selected station, with a chosen detection method. The detections are then compared across the channels to check if there is any overlap between them. As an example, some detections with the use of Recursive STA/LTA applied on a 0.3-1.5 Hz pre-filtered data are shown in Figure 6.11a. Notice in this example how the Trigger-On and Trigger-Off times vary across the channels, making different time-windows for the same signals, or even how there are detections on the vertical, but not on the horizontal components. The MCCT method establishes a final time-window by taking the earliest Trigger-On and the latest Trigger-Off times from the time-window in the overlap, and then mark it across all the components as a final detection. The Figure 6.11b illustrates the result of the MCCT method applied to the example of individual detections referenced before (Figure 6.11a).

For a final time-window of a signal to be established, the overlap must exists in 2 out of the 3 components; then 2 is the threshold value. This is why in the example, the detections achieved only in the Z channel (see Figure 6.11a) do not appear as final detections across the components (see Figure 6.11b) and these false detections are discarded. Nevertheless, there are situation where, for certain periods of time across the 2-years, only 1 or 2 components out of the 3 are available in some stations. In this case, the threshold value is set to 1. Any other situation that do not match the above conditions makes the detection to be officially discarded.

Finally, the Trigger-On times are taken as the theoretical P-wave arrival. Notice that by selecting the earliest Trigger-On in an overlap the error of the P-wave picking is reduced as it moves to the earliest detection from the beginning of the signal. No other phases were picked since they are not clearly emergent on the majority of events. For example, trying to pick an S-wave phase could bring huge errors in the earthquake location step.

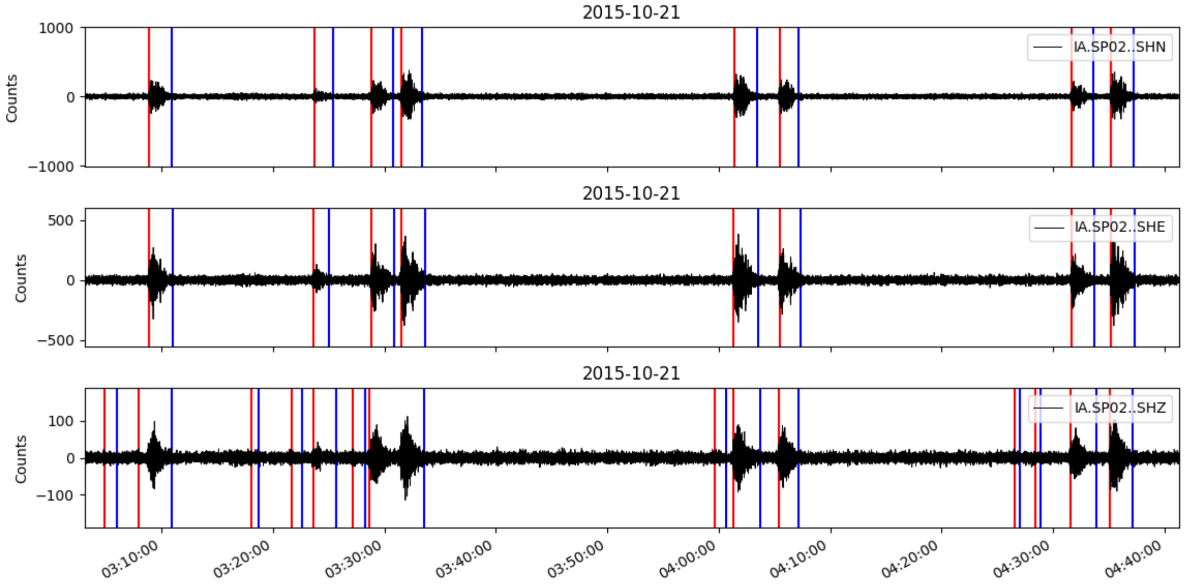

(a) Recursive STA/LTA applied individually to each channel of station SP02, with a 0.3-1.5 Hz pre-filter.

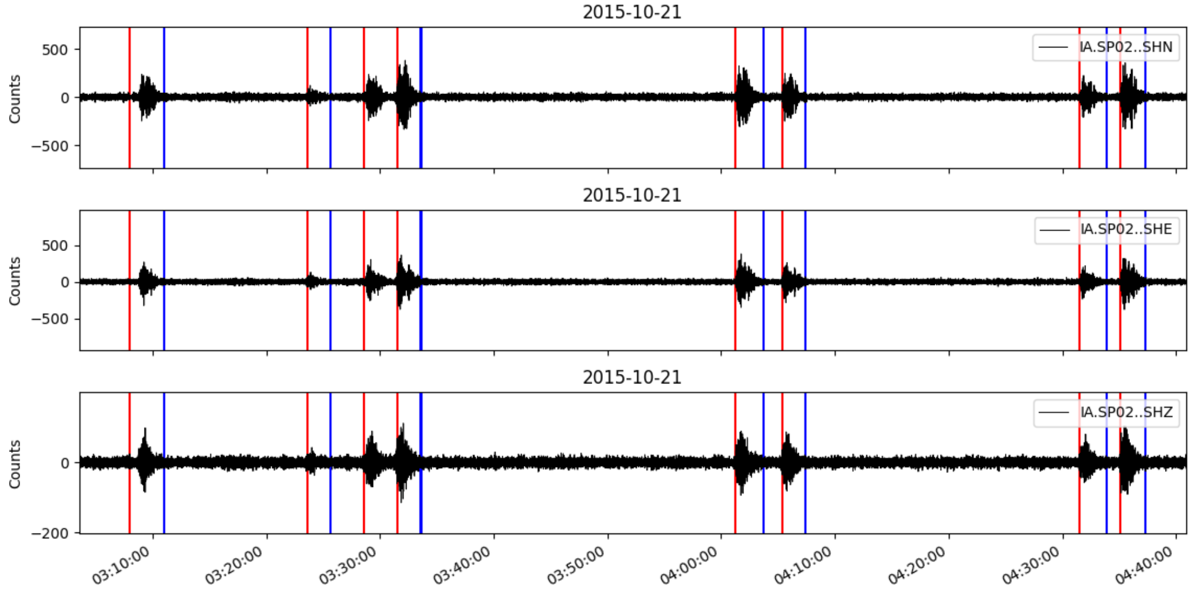

(b) Result of the Multi-Component Coincidence Trigger (MCCT) method applied to station SP02 from the individual channel detections from the image above

Figure 6.11: Multi-Component Coincidence Trigger method (MCCT) applied to 0.3-1.5 Hz pre-filtered signals from station SP02. Data from 2015-10-21 (year-month-day).

6.4 Association of Detections

The association process aims to group those detection picks that could best fit the different arrival times in each stations that comes from the same event or a particular earthquake (Stewart, 1977). This is a very difficult step to assess in seismic routine processing and often is very limited, specially in this study case. Recalling Chapter 2, the tectonic setting on the study is on an active margin, with volcanic activity and a recent mud-eruption systems. Based on this, it is expected to find high amounts of seismic activity from different sources, and they might happen simultaneously. There are several ways to approach this problem, but in this work it was use the simplest one, which is establishing a defined time-window for an specific event to happen (Stewart, 1977).

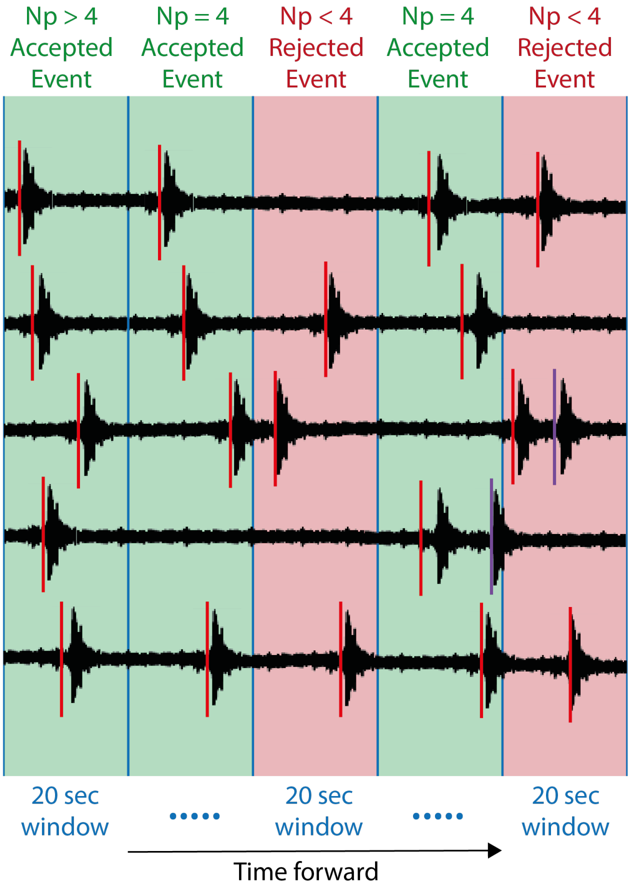

Figure 6.12: Example with edited waveforms to illustrate the way the association window method works. Each waveform line represents the recordings of a different station. Notice that the detected arrivals in red are the first arrivals in each window, and are the ones that are associated. Other arrivals that come after those (purple) are not taken into account.

The Figure 6.12 illustrates the association method used. Entire days were divided into 20 seconds to establish consecutive 20 second windows (4320 windows per day). The number of detection times from stations falling in each window were associated as P-wave arrivals corresponding to the same event. If there were 2 or more detections from a single station falling in the same window, then only the first detection was used. This basically states that maximum number of events that can happen in 20 seconds is 1. The length of the time-window to group the detections was established by the data inspection process, where arrival times in most of the distant stations were observed.

For a local event, based on the P-wave velocity on the first layer (4.3 Km/s from the velocity model chosen; further discussed) and the largest possible distance between stations ($\sim$ 140 Km), the time-window should be of around 32 seconds. Even if this time-length could be the optimal, it could also represent several problems such as discarding other events that could have occurred near the same time since the window is to long. This problem at the end is reflected on a reduction of detected events in the final earthquake catalog. Also there is a high chance of mixing detections of one event with another one, which could bring high errors on the location step

Each group of associated detections constituted as a possible event. A threshold of $\geq$4 detections in a single group was used to mark each group as acceptable candidate events, while the rest are discarded. This number was established since 4 parameters are needed to solve an earthquake location: latitude, longitude, depth, and origin time. The number 4 constitutes then the minimum number of inputs needed to solve the 4 variables.

Most of the earthquakes detected by the stations seemed to be from upper crust to subsurface depths based on the amplitude relations between components as shown with SP02 in Figure 6.11 (special attention to the counts scale axis). As mentioned by Fallahi et al. (2017) and Obermann et al. (2018), these are mostly microseismic events, where the tremor signals are included.

6.5 Polarization Analysis

In the detection and later MCCT processes, the main goal was to pick as accurate as possible a window that describes the signals on interests, from P-wave first arrival to the transient vanishing of most of the signal energy. There are signals with emergent first P-wave arrivals that show weak impulses and also other ones with strong impulses, meaning that the exact time-pick is complex for the detection method. This is due to the high S/N ratio pointed by Minetto et al. (2019), but also it could be due to presence of surface waves on continuous tremors, besides the tectonic clear impulses.

In order to validate or contradict the surface waves assumption by Minetto et al. (2019) and check the first-arrival picks obtained, a polarization analysis was done to all the waveforms of the stations involved in each of the associated detections (events), as long as there are 3 components available. A clear visibility or clarification that it could be a P-wave would then validate the process. It is well-known that polarization measurements may indicate the arrival of different seismic phases and discriminate between body and surface waves (Flinn, 1965; Lois et al., 2013).

For the polarization analysis, the method of Flinn (1965) was used, and also part of the ObsPy library (Beyreuther et al., 2010). Even if the method is old, it is still widely use due to its computational efficiency, with also some modifications (Vidale, 1986; Walck and Chael, 1991; Lois et al., 2013; Greenhalgh et al., 2018). For each station involved in the event, the traces in each component were taken (Z, N, and E). However, the data of interest is around the theoretical P-wave arrival, and thus a time-window was selected around the first-arrival time on each channel. If any detection was done using a pre-filtering; which is the case of this study, then the traces were also pre-filtered in the same way (0.3-1.5 Hz). A time-window of [1,1] was established; 1 second before and 1 second after the first-arrival time. The time-windows are used with the intention of spotting a good behavior of the particle motion during the first-arrival time. It was estimated that 2 seconds for the 0.3-1.5 Hz pre-filter is sufficient to evidence a clear particle motion path.

As an example of this, the Figure 6.13 shows the particle motion in the horizontal projection and vertical of the stations involved in the specific event detections. The difference between the window lengths around the first-arrival time obeys to the same fact of the pre-filtering. Longer periods require for a longer time window than the shorter-periods, as it takes more time to describe the cycling path of the particle motion.

The data in the 2-seconds window is normalized with respect to the maximum value across all the components, and then used for the covariance matrix construction (see again Equation 4.4). Following the Equations 4.4, 4.9 and 4.10, the next parameters were obtained for each time-window instance:

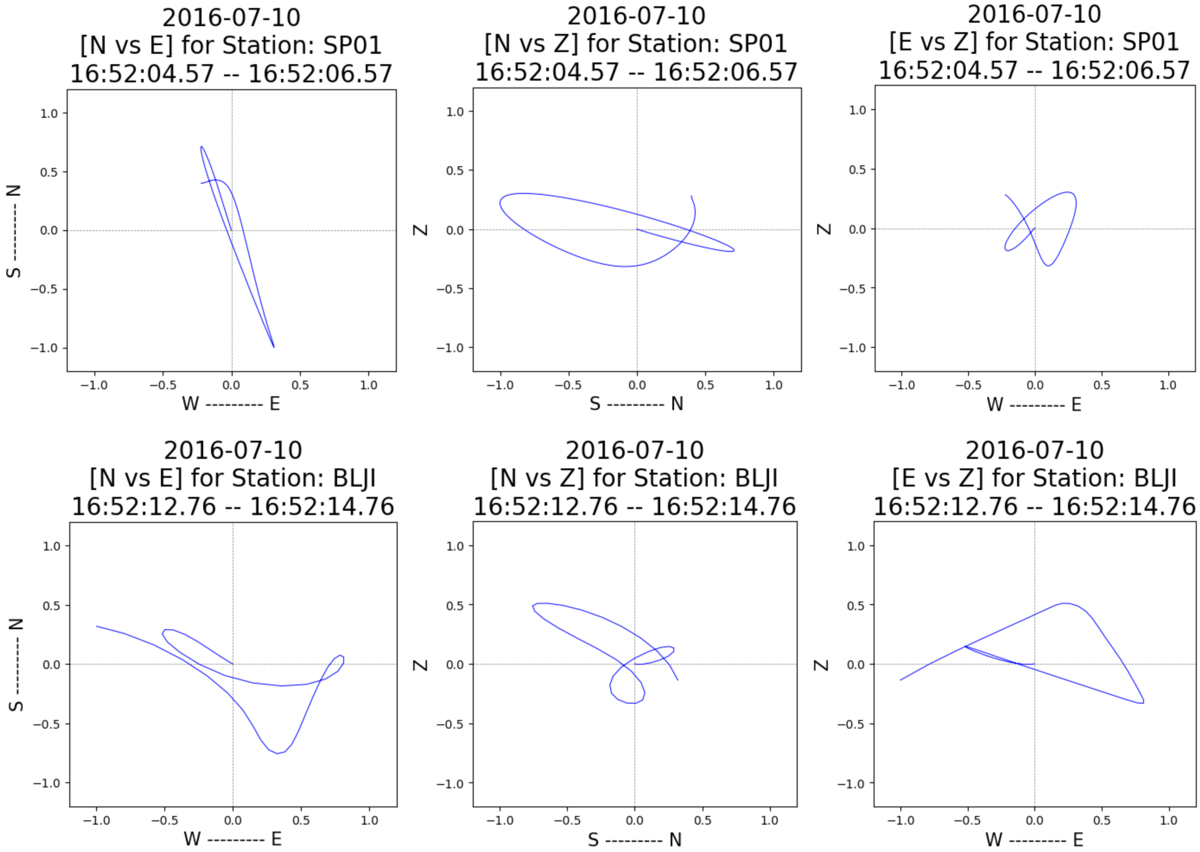

Figure 6.13: Particle motion plot in E vs N, N vs Z, and in E vs Z components for detections achieved with a 0.3-1.5 Hz pre-filter, and later associated as an event. Here a time-window of 1 second before and after the first-arrival pick is used.

rectilinearity, planarity, and the ratios between the smallest eigenvalues and the largest eigenvalue (λ_2/λ_1 and λ_3/λ_1).

In order to understand better the rectilinearity and planarity parameters, aside with the ratio values, a perfect P-wave and Rayleigh wave motion was simulated using the sin and the cos trigonometric functions (see Figures 6.14 and 6.15). Finally, to apply it to real data, the polarization analysis was also observed with several examples from the data. The Figure 6.16 shows an example with one event captured by the station SP01, where a window was taken around the P and the Rayleigh waves.

After the polarization was made to all the first-arrival windows, the following constrains were established to classify whereas the theoretical P-wave pick correspond truly to a P-wave, or is a surface wave: 1) rectilinearity and planarity must be the higher than 0.9, and 2) λ_2/λ_1 and λ_3/λ_1 must be lower than 0.2. The conditions were set in accordance to the theory (see again Chapter 4), to the simulations plots of a P and Rayleigh wave (see Figures 6.14 and 6.15), and with the real examples (see Figure 6.16). According to the Equations 4.9, 4.10, and the plots, the ratio values are a representation of the rectilinearity and planarity, and therefore, setting the constrains with the eigenvalue ratios is a redundancy on the rectilinearity and planarity constrains. Nevertheless, the values have shown that they are not completely concordant, and slightly differences exists. Also, it served as a confidence control measurement, where a confident ellipsoid geometry will then be reflected as small values in the ratios.

As an addition, another threshold is adopted to classify the type of event, mostly to determine the accepted quality of the P-wave. If an event (group of associated detections) had a certain number of

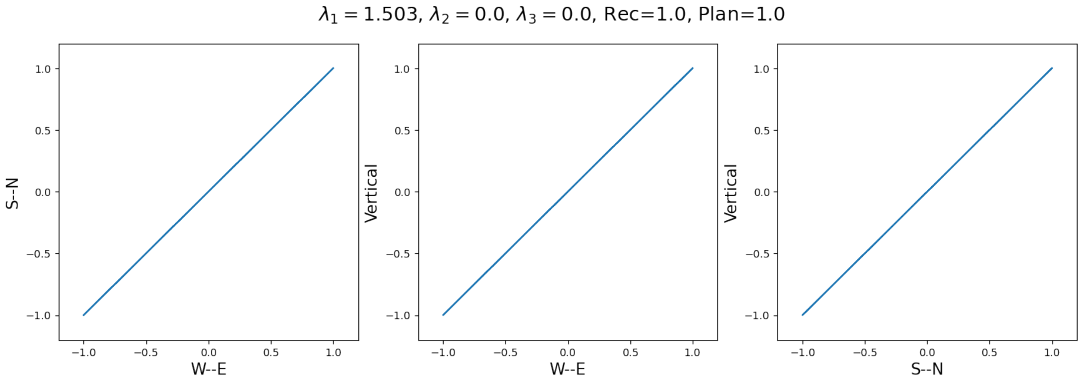

Figure 6.14: Simulation of P-wave particle motion and polarization analysis (linear motion). Polarity analysis results: λ_1=1.503, λ_2=0.0, λ_3=0.0, λ_2/λ_1=0.0, λ_3/λ_1=0.0, Rectilinearity=1.0, Planarity=1.0.

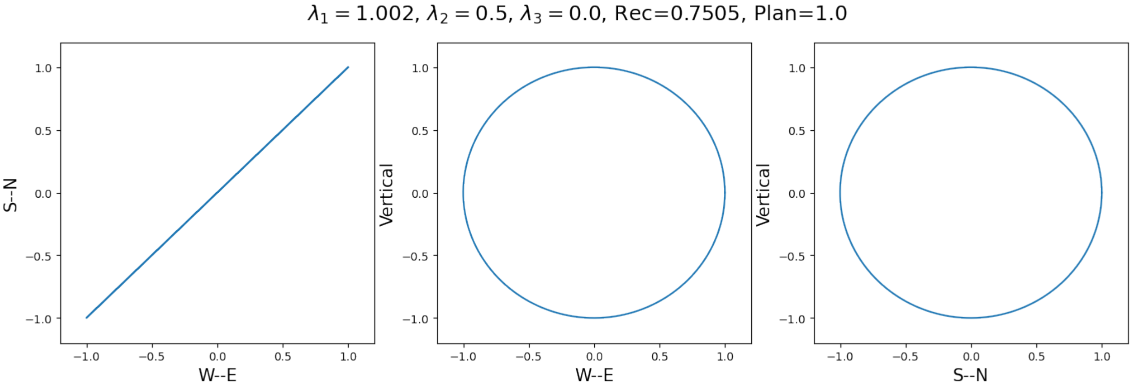

Figure 6.15: Simulation of Rayleigh wave particle motion and polarization analysis (elliptical motion). Polarity analysis results: λ_1=1.002, λ_2=0.5, λ_3=0.0, λ_2/λ_1=0.4990, λ_3/λ_1=0.0, Rectilinearity=0.7505, Planarity=1.0.

confirmed P-wave picks $N_P \geq 4$ from the last conditions, then it is classified as a P-wave event. Otherwise, it was label as Rayleigh-wave event.

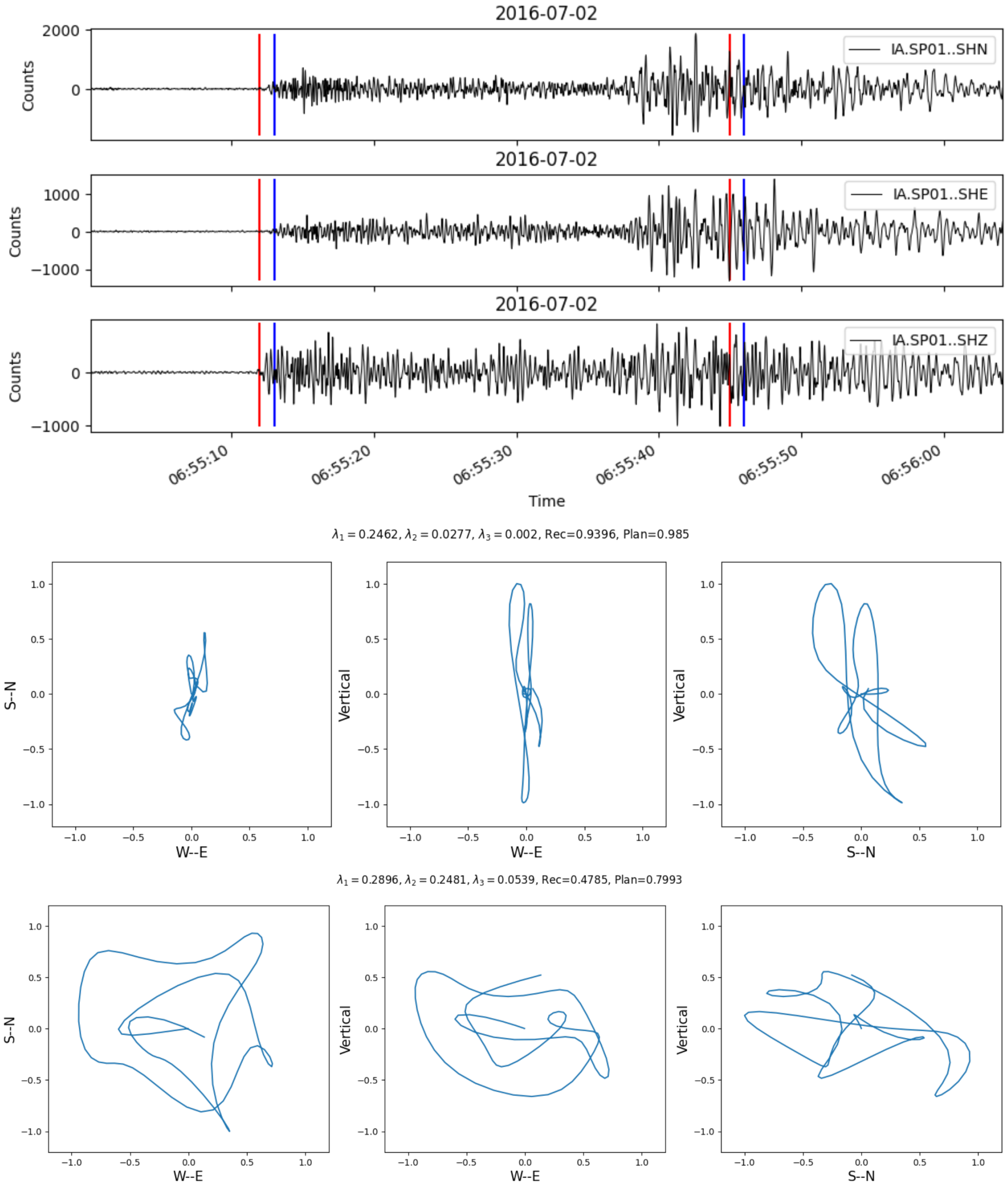

Figure 6.16: (Top): Seismic event captured by the station SP01, with 2 windows selected around the P and the Rayleigh wave. (Middle): Particle motion of the P-wave and its polarization analysis: λ_1=0.2462, λ_2=0.0277, λ_3=0.002, λ_2/λ_1=0.1125, λ_3/λ_1=0.008, Rectilinearity=0.9396, Planarity=0.985. (Bottom): Particle motion of the Rayleigh (R) wave and its polarization analysis: λ_1=0.2896, λ_2=0.2481, λ_3=0.0539, λ_2/λ_1=0.8567, λ_3/λ_1=0.1861, Rectilinearity=0.4785, Planarity=0.7993

6.6 Location of Events

Notice from the last step that the true intention of the classification is to separate the reliable events that can be located as hypocenters from the ones that are not reliable. Then it is understood that only P-wave class events are going to be localized since they reliable candidates for hypocenter location search.

Several methods have been developed from the forward modelling techniques for earthquake location, from simple Linear Inversion to Maximization of Probability Density Functions (PDF). For this study, a probabilistic approach was chosen to overcome the main problems of linear inversions.

The code used in this study for the location routine was NonLinLoc from Lomax (2004), written in C language. The program is a set of codes and packages for velocity model construction, travel-time calculation and probabilistic/non-linear earthquake location in 3D structures. Most of the packages operates as a 3D grid structure which defines a gridded rectangular volume for Non-Global problems and spherical sections for Global approaches Lomax (2004).

The program presents several methods for earthquake location, however, the chosen one was the Oct-Tree Importance Sampling algorithm; a grid-search method which recursively involves subdivisions and samplings in 3D space (Lomax, 2004).

All the events obtained from the previous steps were written in a preferred phase-file format that is recognized for NonLinLoc. The code can accept several formats such as SEISAN, HYPO71, SIMULPS, and others (Lomax, 2004). Due to simplicity, the chosen format was the one designed for this program; NLLoc phase-file format, where each line has the code of the station, component, phase detected, polarity, specific arrival-time of the phase and time-uncertainty (Lomax, 2004).

Once the phase-files are written in the NNLoc format, the next step was to fill the Input Control File, where all the parameters or necessary information for the location routine goes (Lomax, 2004). The file is divided into several sections to fill, which correspond to scripts that must be executed in a certain order to finally get the locations (Lomax, 2004). All inputs and important parameters used are shown in the Table 6.2.

The first section corresponds to the Generic Control Statements, which describes the initial description of the 3D grid location area (see Table 6.2). Since the search is going to be on a local part (East Java) instead of a global search, then an Azimuthal Equidistant projection with WGS-84 coordinate system was selected, aside with a coordinate that is going to be the center of the search area. This also is needed for distance calculation between points in the search space.

For computation time efficiency, NonLinLoc use velocity and time grids with defined station locations for computing theoretical ray-paths instead of running this calculations every time a location is needed (Lomax, 2004). This is the use of the second, third and fourth sections of the Input Control File (Lomax, 2004).

The second section, *Vel2Grid*, was used to define the 3D velocity grid for P waves with slowness values. Here, 3 1D velocity models were taken into consideration. The first one was the velocity model calculated by Koulakov et al. (2007), from a local tomography inversion in Central Java, and used nowadays by the Meteorological, Climatological, and Geophysical Agency of Indonesia (BMKG). The second one is the model developed by Obermann et al. (2018) from the inversion of travel-time data in East Java. The mentioned data came from some of the stations used in this work that are installed over the AW volcanic complex. The third and last velocity model comes from an applied receiver functions analysis on S-waves in Central Java, by Ariyanto et al. (2018). The Figure 6.17 shows the 3 curves, each one representing the different velocity models. For this study, the model from Koulakov et al. (2007) was chosen for the location process since is the one used for the national network (BMKG) and because it is the one from the 3 models that can cover the largest depth range, and the goal is to search for possible sources; from top volcanic, to subduction slabs.

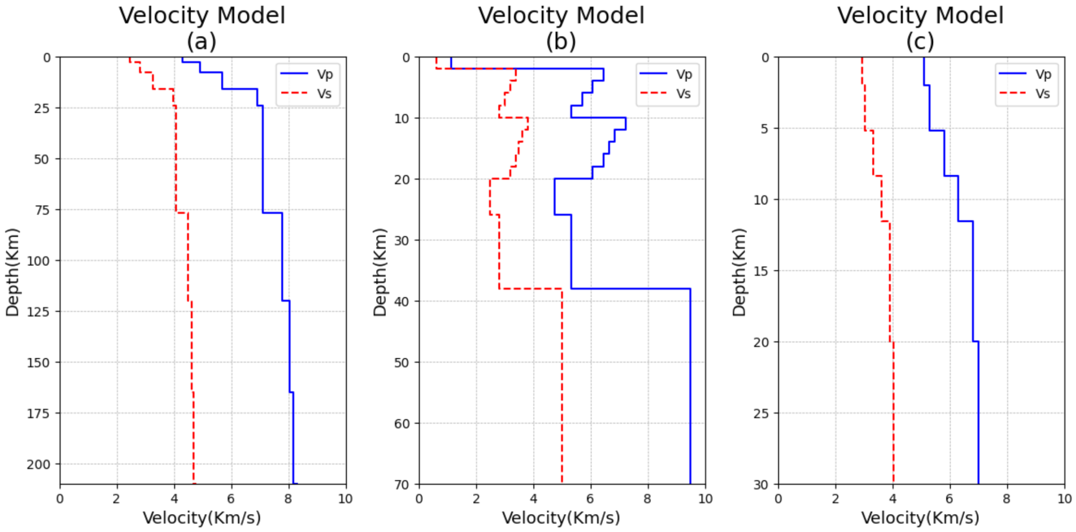

Figure 6.17: Velocity models considered of this study. a) Velocity model from Koulakov et al. (2007), b) velocity model from Ariyanto et al. (2018), and c) velocity model from Obermann et al. (2018).

The Table 6.2 shows the number of points for the velocity grid. Notice that the number of points in the x-direction is 2, and this is since the model to use has no horizontal changes, but only vertical, as the proper 1D original model (Koulakov et al., 2007). The resolution of the velocity block was set to 500 x 500 x 500 meters (see Table 6.2).

The third and fourth sections, *Grid2Time* and *Time2EQ*, make use of pre-calculated take-off angles for the theoretical P arrival-times to the stations from different theoretical source points (Lomax, 2004). To take into account errors, an error of 0.2 seconds was estimated for the P-waves based on the pickings explored in the detection process (see Table 6.2). The Vp/Vs ratio used, a mandatory parameter, was of 1.74, given by Koulakov et al. (2007) as the ratio which provides the minimum Root Mean Square (RMS) values of P and S residuals.

The final section for the Control Input File runs the *NNLoc* code for locating the earthquakes, using the Oct-Tree method (Lomax, 2004) with a probabilistic function from the Equation 4.18. It starts with a grid of 481 x 481 x 201 points, with center in the central coordinate established in the Generic Control Statements, and with a spacing of 1 Km between each node, in all directions (see Table 6.2). The subdivision of each cell is done by 20 x 20 x 20 points iteratively, until reaching the best location point possible (see Table 6.2). The algorithm stops when it reaches a resolution of 10 meters.

SECTION OF INPUT FILE / PROGRAM	**VARIABLE**	**VALUES**
Generic Control Statements	*Geographic Transformation*	Azimuthal/Equidistant WGS-84
	Central Coordinate (Geographic Origin)	-7.8, 112.5
Vel2Grid	*Wave Type*	P
	Grid Type	Slowness
	Velocity Grid points N_x, N_y, *and* N_z	2, 1601, 405
	Velocity Grid Origin (respect to Geographic Origin) X, Y and Z (Km)	0.0, 0.0, -2.0
	Velocity grid point spacing dx, dy and dz (Km)	0.5, 0.5, 0.5
	Velocity model	(see Figure 6.17)
Grid2Time	*Take-Off angles grid calculated*	True
	Network list	(see Table B.4)
	Podvin and Lecomte Finite Difference fraction	10^{-3}
Time2EQ	*Station Error Type for P-wave*	Gaussian
	Error for P-wave	0.2 sec
	Vp/Vs	1.74
NLLoc	*Initial Location Grid points* N_x, N_y, *and* N_z	481, 481, 201
	Initial Location Grid Origin (respect to Geographic Origin) X, Y and Z (Km)	-240, -240, 0.0
	Initial Location Grid points spacing dx, dy and dz (Km)	1.0, 1.0, 1.0
	Grid Type	Probability Density Function
	Location Method	EDT sum probabilities by the variance of origin-time estimates over all pairs of readings
	Minimum number of phases to accept before location	4
	Location Search Method	Oct-Tree
	Location Search Grid points N_x, N_y, *and* N_z	20, 20, 20
	Location Search Grid smallest node spacing (Km)	0.01
	Give high search priority to cells containing stations (Ideal for dense cluster of local stations)	False

Table 6.2: NonLinLoc parameters in the Input File for the Oct-Tree earthquake location method.

CHAPTER 7

Results

The following results present some statistical aspects about the detections achieved on the dates and in the stations mentioned in the Chapter 6 as a way to evaluate the methods used. Following this, the location of the events are displayed.

7.1 MCCT Detection

The Recursive STA/LTA, as said before, was used on the MCCT method, which was the final detection algorithm to approach the multi-component stations in an attempt to have the advantage of the detections on the channels, and integrate them. The Table 7.1 shows the comparison in the number of detections per day on the specific dates for the station SP01, between the Recursive STA/LTA method on individual channels, and the MCCT method.

Table 7.1: The number of detections achieved with the Recursive STA/LTA; applied individually to channels and compared with the MCCT on several dates (year-month-day) to records of the station SP01, pre-filtered between 0.3 and 1.5 Hz.

Station: SP01	**2015-03-20**	**2015-10-15**	**2016-02-02**	**2016-09-10**
N	184	311	293	194
E	200	220	294	243
Z	187	295	324	273
MCCT	**153**	**235**	**294**	**207**

As observed, the number of detections achieved by MCCT never exceeded the maximum value from all the components in each date, but it constantly falls in between the maximum and minimum detection numbers achieved from the channels, with the exception on date 2015-03-20, where its value was lower than all the individual detections on the components.

Regarding individual channels, the N component showed to be the one with the less detections in the dates shown on the Table, except on the date 2015-10-15, which turns to be the maximum. Also, the Z component showed high number of detections on the dates 2016-02-02 and 2016-09-10, which are noticeably higher than the other components.

7.2 Detections

After achieving a database of all possible events (associated detections), the detections were inspected by extracting several features such as: distribution of detection durations, detections per hour and per day, and a ratio that could indicate how many detections were grouped into events. Is is difficult to make for all the stations in all the data period, and so, only 5 stations in 4 days were analysed for inspection. All this is exposed in the Results (Chapter 7).

For the stations, the following ones were selected: SP01, SP03, BB05, KRK, and BLJI (see again the network map on Figure 6.7). The 3 first ones represents the best coverage in AW, while KRK and BLJI represent 2 of the 3 permanent stations used for extending the azimuthal coverage. For the 4 days, the following ones were selected (year-month-day): 2015-03-20, 2015-10-15, 2016-02-02, and 2016-09-10. The selection was made in a way that could be equally distributed across the 2 years of data.

Detections on 2015-03-20

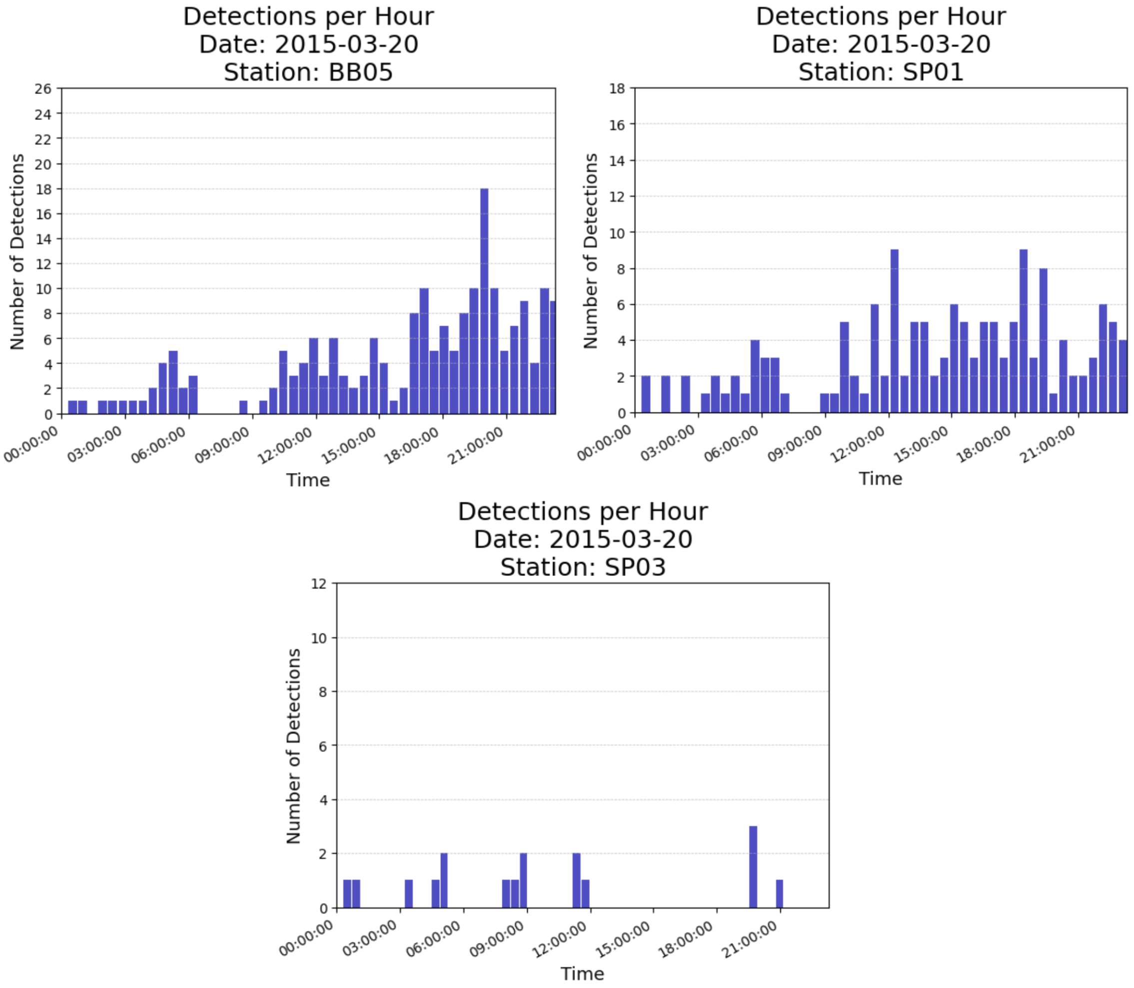

Figure 7.1: Detections per hour for stations SP01, BB05 and SP03 in 2015-03-20. Stations KRK and BLJI have no record on this date. The detections are after the MCCT method and before association step.

The Figure 7.1 shows the distribution of detections during the date 2015-03-20 for the stations selected, except for KRK and BLJI since they have no recordings on this day. Here the stations BB01 and SP01 present a similar behavior during the day, as the number of detections increase towards the afternoon hours.

Both start with no significant detections from 00:00:00 until near 05:00:00 (UTC hour:minute:second). After this time, they exhibit a slight increase beginning from 05:00:00, achieving a local maximum at near 06:00:00 and then descending by 09:00:00. Then, from 09:00:00 to 15:00:00 there is a second increase-decrease in the detections. Nevertheless, after this point, the station BB05 makes another jump in the number of detections while SP01 maintains them constant, with the exception of a noticed decrease near 21:00:00 and a quick recovery. This decrease is also seen by BB05, but not so noticeable since afterward, it maintains the number of detections.

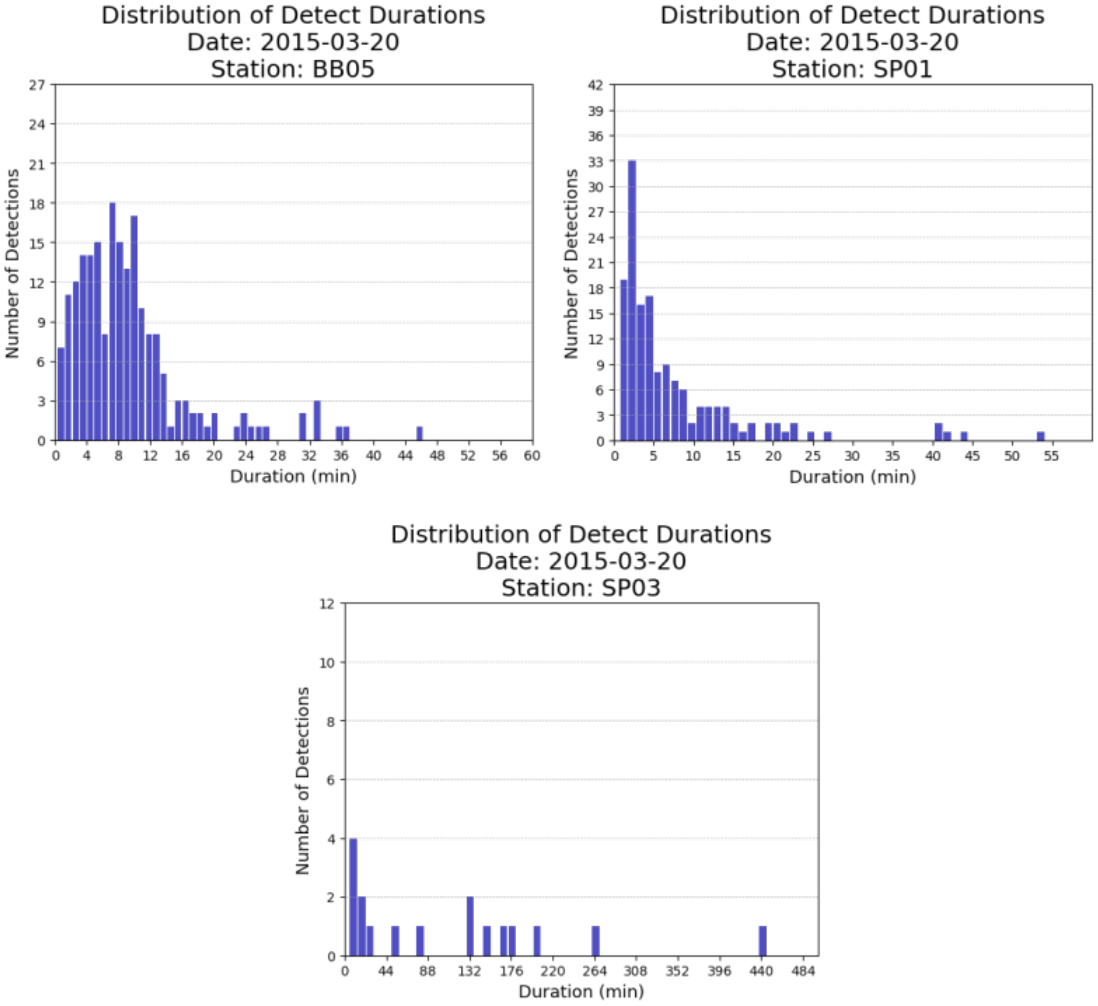

Figure 7.2: Distribution of detect durations for stations SP01, BB05 and SP03 in 2015-03-20. Stations KRK and BLJI have no record on this date. The detections are after the MCCT method and before association step.

The duration of the detections are slightly different between the stations SP01 and BB05 on the 2015-03-20 (see Figure 7.2). Both of them present detections with duration concentrated between 0 and 10 minutes and a sort of exponential decay on the number of detections in relation to the increase of duration. However, the station SP01 has its maximum below 5 minutes, while the station BB05 has it near 8 minutes. While the station BB05 exhibits detections more distributed in the duration range with less number of detections on each against the station SP01, the last one has a high number of detections but in a less distributed duration range, below the 5 minutes. Also, both present a similar number of detections above the 10 minutes of duration.

The station SP03 does not exhibit a clear distribution in the number of detections during a day, as it shows significantly less detections than the other stations. Nevertheless, the distribution still shows the same behavior as the other stations; an increase in detections at afternoon-night hours. Regarding the duration distribution, there is a maximum of them concentrated below 30 minutes (see Figure 7.2).

Nevertheless, it presents durations between 100 and 200 minutes, which is extremely different from the distributions reported by the other stations.

Detections on 2015-10-15

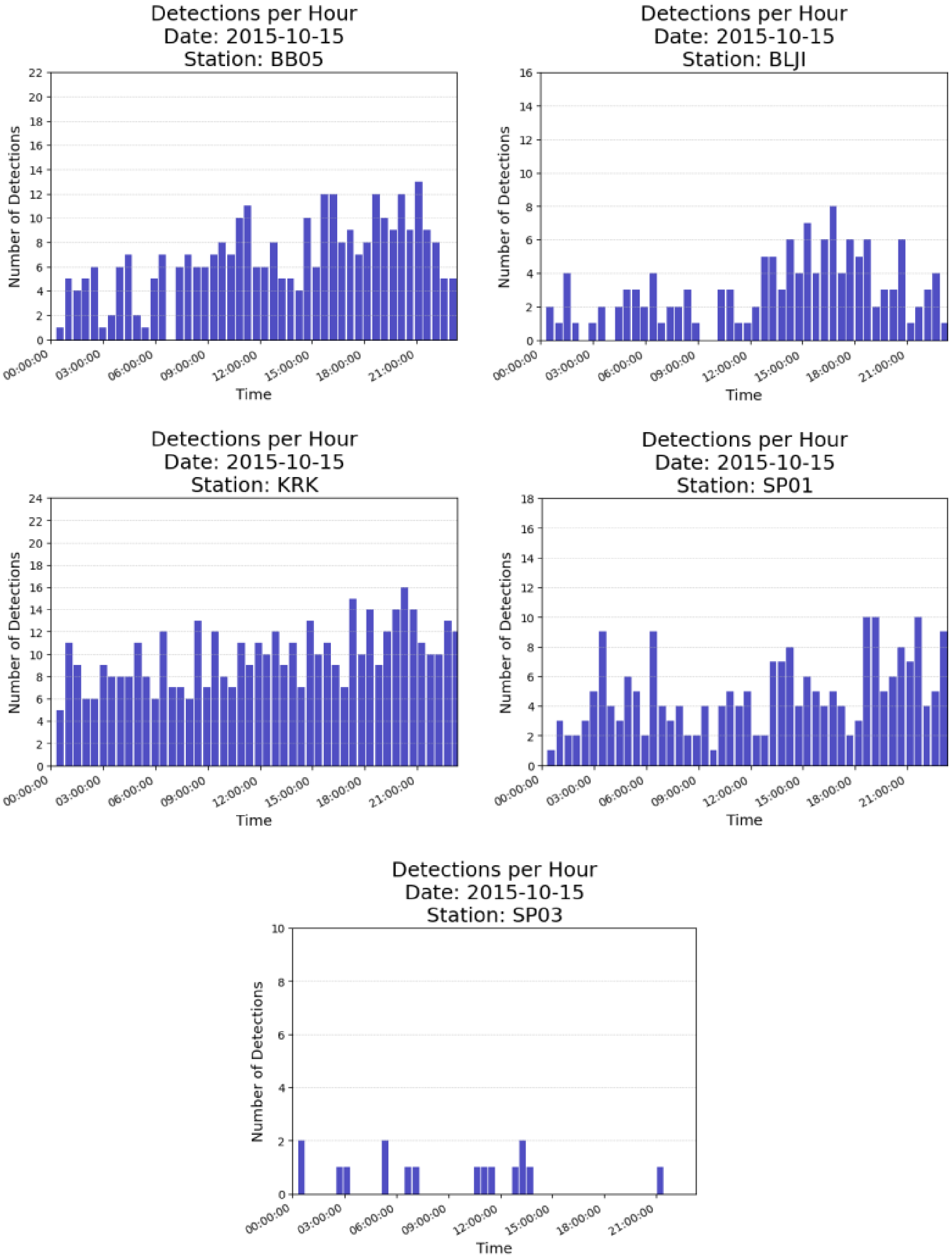

Figure 7.3: Detections per hour for stations SP01, BB05, KRK, BLJI and SP03 in 2015-10-15. The detections are after the MCCT method and before association step.

On the date 2015-10-15, all the selected stations present recordings (see Figure 7.3). The station SP03 shows a similar behavior as on 2015-03-20, both in detection distribution and duration of the detections (see Figure 7.3 and 7.4). No clear tendency is visible for this station, however, the situation is different for the other stations.

The stations BB05, SP01, KRK, and BLJI shows again a tendency of increase in the number of detections, from 00:00:00 to 24:00:00 (see Figure 7.3). They all show the highest peaks after 12:00:00, mostly during the afternoon-night. The station BLJI exhibits a similar distribution of detections as SP01 on the 2015-03-20 (see Figure 7.1), while the rest have changed their detection distribution over the day; where the stations KRK and BB05 have similar behavior.

In terms of the duration of these detections, the station SP03 maintains the same distribution (see Figure 7.4). The stations KRK, SP01 and BLJI present detections with durations mostly concentrated below 6 minutes, while BB05 detections are mostly around the same value instead of below. The detections tend to have more distribution at near 1 minute of duration, however, the station BB05 shows this value at near 6 minutes. The station BB05 is not showing an exponential decay on the distribution graph as the other stations, but mostly assimilating a gaussian distribution with 6 minutes as the central value. All of the stations, except SP03, show a common weak-peak from 2 to 4 minutes in the distribution of the detect durations.

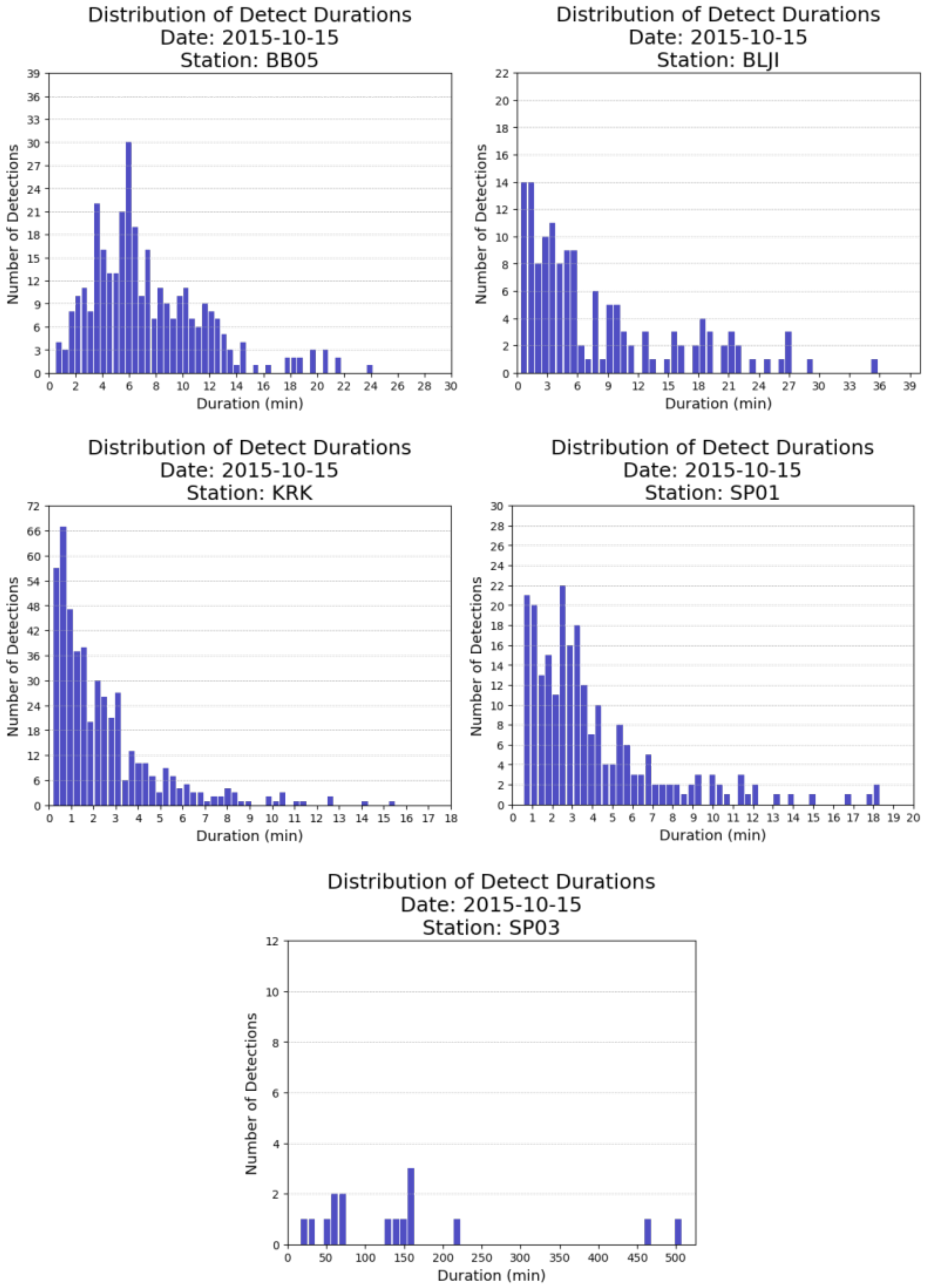

Figure 7.4: Distribution of detect durations for stations SP01, BB05, KRK, BLJI and SP03 in 2015-10-15. The detections are after the MCCT method and before association step.

Detections on 2016-02-02

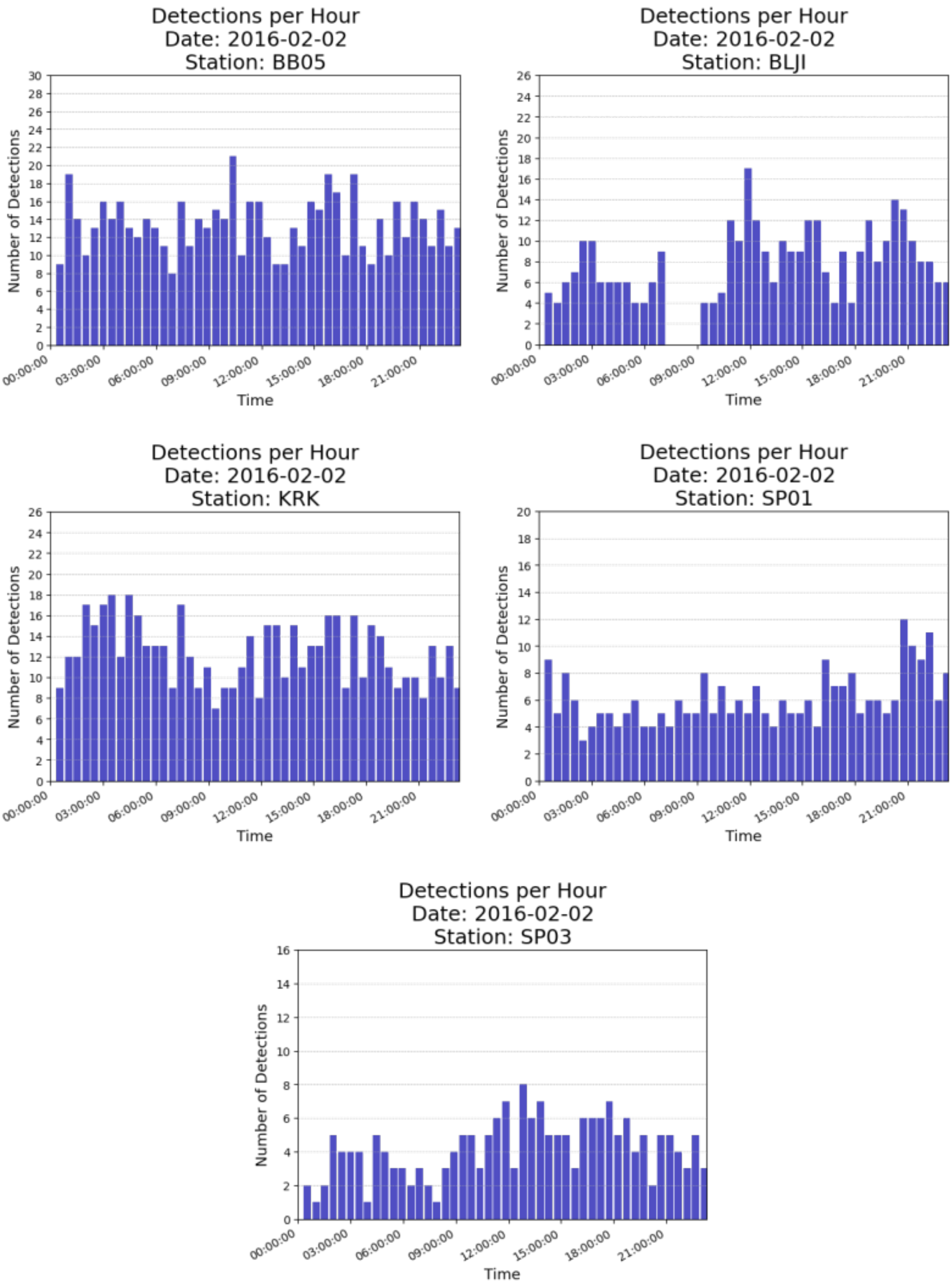

Figure 7.5: Detections per hour for stations SP01, BB05, BLJI, KRK and SP03 in 2016-02-02. The detections are after the MCCT method and before association step.

On the date 2016-02-02, all of the stations show mostly a constant distribution of detections during the day, but the number of detections increased significantly compared to other dates. The increase tendency to detections in afternoon-night hours has disappeared (see Figure 7.5). The station KRK shows 2 cycles of increase-decrease, from 00:00:00 to 09:00:00, and from 09:00:00 to 21:00:00. The distribution of the events on the station BLJI tend to be similar to station KRK, but the second cycle ends near 18:00:00, allowing a third one to appear from 18:00:00 to 24:00:00. Also, the behavior is not completed since there is a gap in the detections, from 07:20:00 to 09:00:00. The station SP03 shows also 2 cycles with the same behavior as the station KRK, but the number of detections is lower. Finally, the stations BB05, and specially SP01, show distributions that tend to be constant through the day. Nevertheless, BB05 presents more significant variations with a total of 4 cycles equally distributed through the time of the day.

Regarding the duration distribution of the detections on the same day, there is also a change in comparison to the other days explored. Now the stations SP01, SP03, and BB05 exhibit a distribution of the detection durations in a gaussian form on the histograms, with a central value near 2 minutes (see Figure 7.6). Also, the distribution histograms for station KRK shows a slight jump in values around the 2 minutes of duration, while the station BLJI shows it between 2 and 3 minutes of duration. This is consistent with the 2 to 4 minute peaks observed at 2015-10-15, but in the present examples they are more clear.

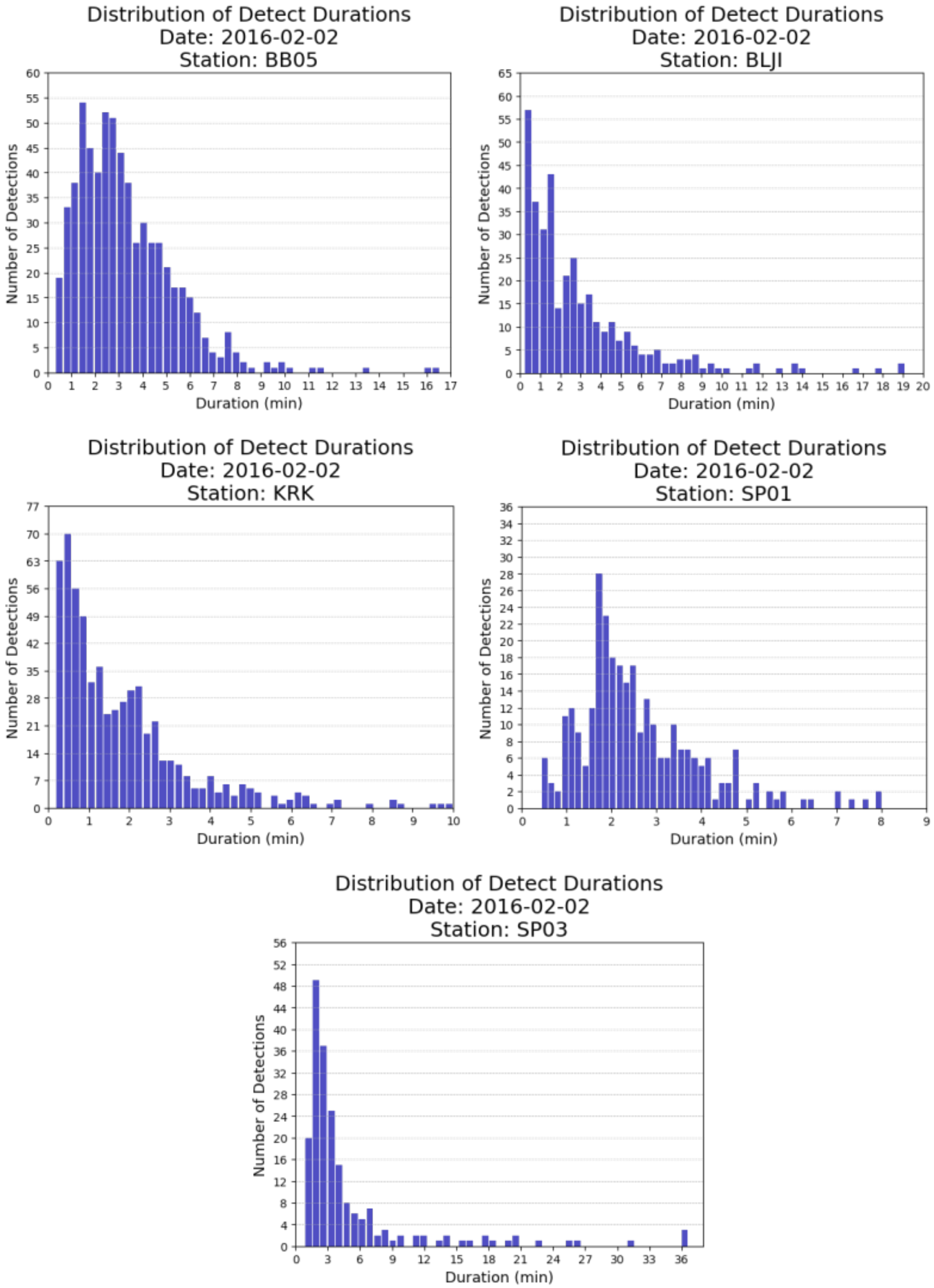

Figure 7.6: Distribution of detect durations for stations SP01, BB05, BLJI, KRK and SP03 in 2016-02-02. The detections are after the MCCT method and before association step.

Detections on 2016-09-10

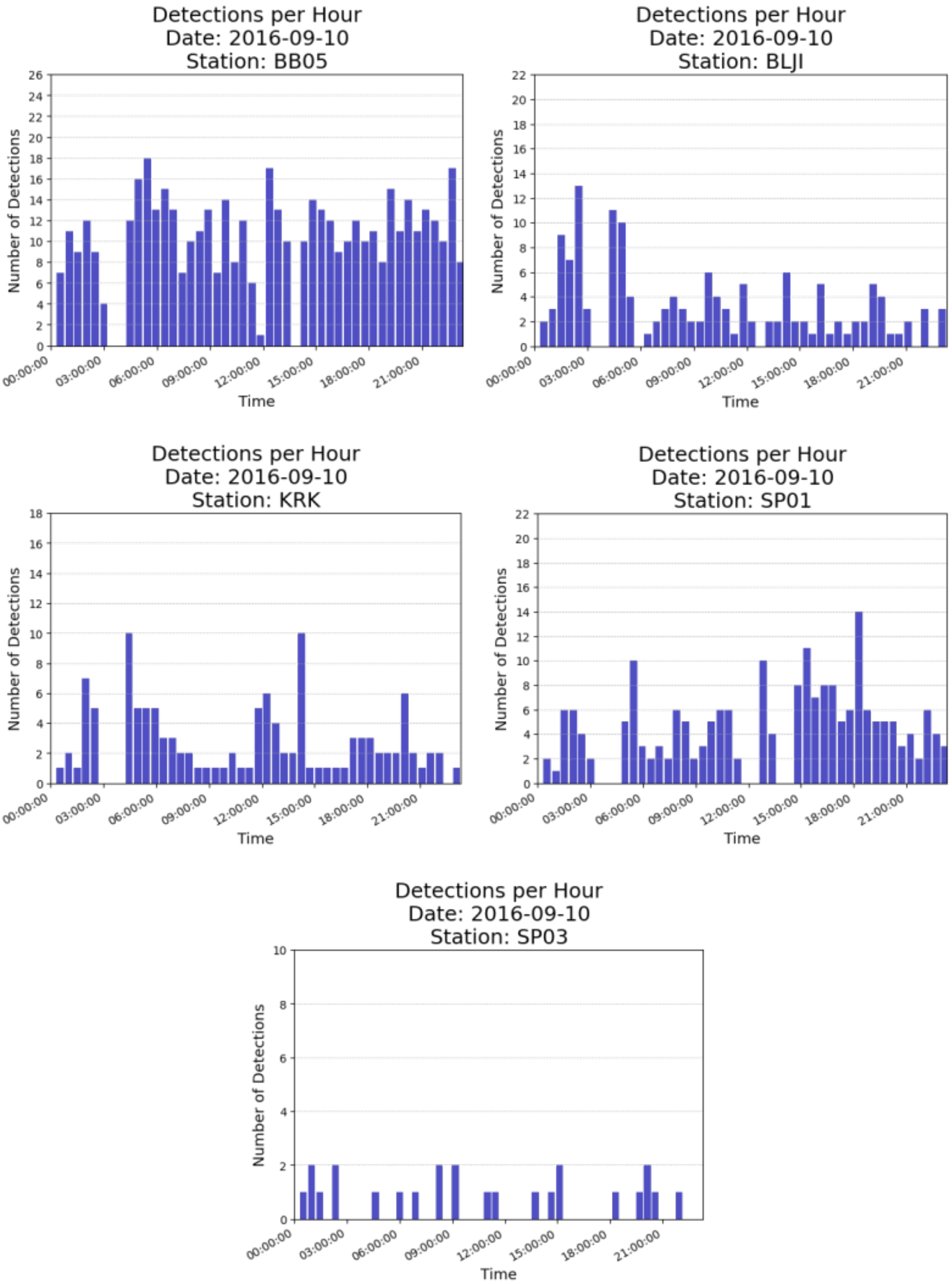

Detections per Hour
Date: 2016-09-10
Station: BB05

Detections per Hour
Date: 2016-09-10
Station: BLJI

Detections per Hour
Date: 2016-09-10
Station: KRK

Detections per Hour
Date: 2016-09-10
Station: SP01

Detections per Hour
Date: 2016-09-10
Station: SP03

Figure 7.7: Detections per hour for stations SP01, BB05, KRK, BLJI and SP03 in 2016-09-10. The detections are after the MCCT method and before association step.

On the date 2016-09-10, the stations BLJI, KRK, SP01 and BB05 no longer present a clear tendency on the number of detection through the day (see Figure 7.7). The distribution at the station BB05 shows a high variation in the rate of detections and thus is not clear to see a pattern, however, its number of detections are higher than the rest of the stations. The stations KRK and BLJI present high number of detections before 09:00:00, and a tendency to flattern the detection rate in lower values, afterwards. All of the stations have high variations in the detection rate, as they present random spikes across the day, and thus do not show a clear tendency as in the other days. Also, the histograms presents some gaps of detections, but all stations share one similar gap which is marked between near 03:00:00 to 04:30:00. For the station SP03, the distribution comes back to be similar as in the first 2 dates explored (2015-02-30 and on 2015-10-15).

Regarding the duration of the detections, the station BB05 present a gaussian distribution with the center between 3 and 5 minutes (see Figure 7.8). Other stations like SP01 and BLJI also try to show in the duration distribution of the detections a similar gaussian behavior, but not as noticeable as with BB05. They have their center from 2 to 3 minutes, and at 5 minutes, respectively (SP01 and BB05). On the other hand, the station KRK shows more an exponential decay in the duration distribution of detections. A curious aspect to notice is that the permanent stations (KRK and BLJI) present high values of duration for some events, which overpass even the 30 minutes long. And last, the station SP03 shows again the similar distribution in the duration of events from the first 2 dates, as it is linked to the distribution in the number of detections during the day (see Figure 7.7).

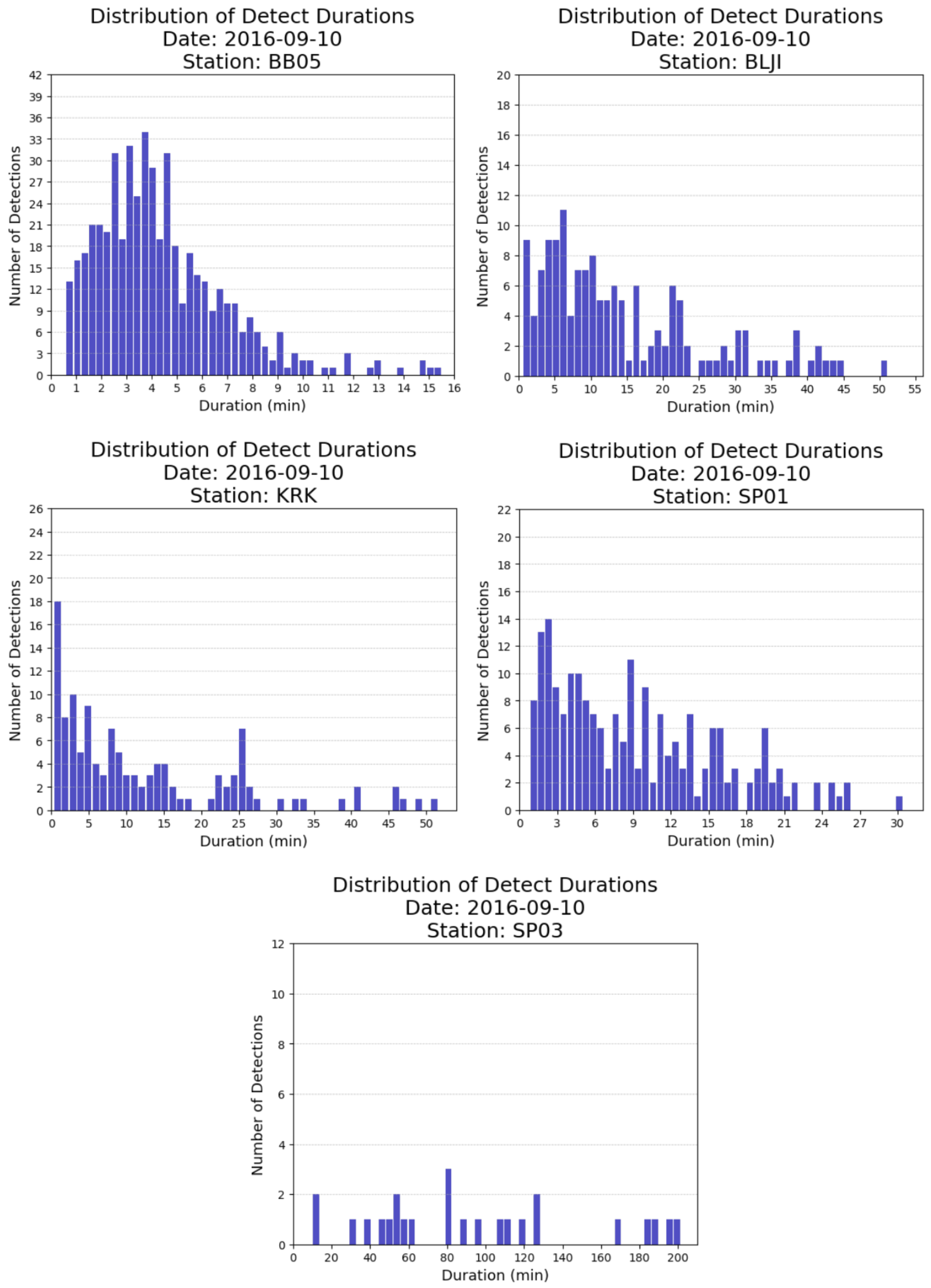

Figure 7.8: Detections per hour for stations SP01, BB05, KRK, BLJI and SP03 in 2016-09-10. The detections are after the MCCT method and before association step.

Ratio of Durations

In all the previous examples of duration distributions the selected stations showed high number of detections with diverse durations. To observe the durations of these detections in context, a ratio d between all the detections and the total time in a day was computed for the selected stations, on the selected days:

$$d = \frac{\sum_{i=1}^{N} t_i}{T} \tag{7.1}$$

where t_i is the duration of the detection i in seconds, T is the total seconds during a day (86'400), and N is the number of detections in a day, obtained from the MCCT method. Then is understood that the value d a ratio that describes the detections of an specific station.

Table 7.2: The ratio of the sum of the duration of detections in a day (year-month-day) with the MCCT method (Recursive STA/LTA), over the total time on a day. The stations used are the same as the ones in the results section. The *NA* values represents the unavailability of data for the certain stations in some dates

Station	**2015-03-20**	**2015-10-15**	**2016-02-02**	**2016-09-10**
SP01	0.8	0.64	0.52	1.33
BB05	1.3	1.67	1.46	1.49
KRK	*NA*	0.8	0.78	1.04
BLJI	*NA*	0.79	0.73	1.5
SP03	1.32	1.7	0.72	1.65

The Table 7.2 shows the results of this duration ratio for the selected stations on the 4 dates inspected. The station SP01 shows ratios of the total detections lower than the total time during a day, with exception on the last date (2016-09-10), and the same behavior is presented for the stations KRK and BLJI, where ratios do not exceed 1.0, with exception on the last date inspected, too. On the other hand, the stations BB05 and SP03 are consistent with high ratios that exceed 1.0, and sometimes, even 1.5.

Total Events

After the association process had produced the final detection groups, a database of events per day was obtained. The total number of events per day, captured by the Bedrock network is shown in Figure 7.9, aside with the eruption periods from Mt. Bromo, reported by Venzke (2016). From the number of events per day, several peaks periods of interest have been noticed.

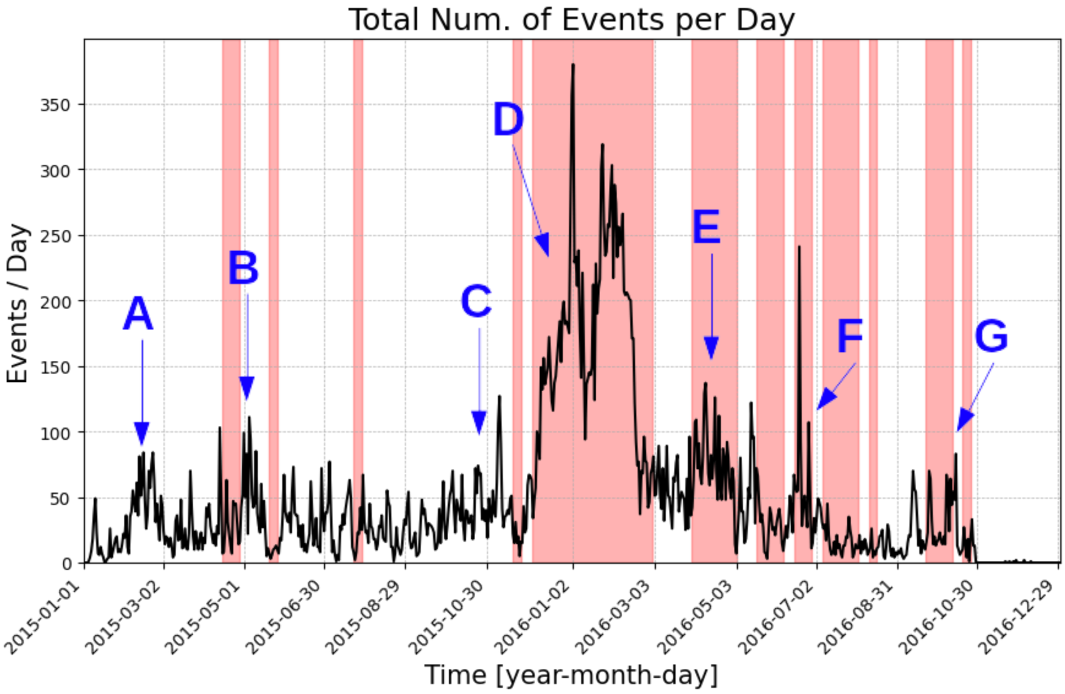

Figure 7.9: Total number of earthquakes per day. These are the final associated detections conforming group of events, searched between 0.3 and 1.5 Hz. Red areas indicate reported periods of Mt. Bromo eruptions (Venzke, 2016). The main peaks identified are labeled with letters from A to G.

The first peak period (A) is from 2015-01-31 to 2015-03-02, followed by the second one (B), which goes form 2015-05-01 to 2015-05-20. Both of the mentioned peaks overpass the 50 events per day, but just the second one reaches above the 100 events. A minor increment is reached as a third peak (C), from 2015-09-15 to 2015-11-20, with similar characteristics as the second one, but wider as it covers more time-range than the last two. Afterwards, the number of events per day presents the fourth peak period (D), one of the highest, between 2015-11-20 and 2016-01-10, showing an increase from 10 to more than 350 events per day. On the date 2016-01-10, the number of events have been reduced from 350 to approximately 140, and afterwards, increases again up to 320 on 2016-01-22, and decays below 50 events per day on 2016-03-27. The fourth peak period marks the highest number of events per day by far in contrast from the rest of the other peak periods. From this point, 3 other peak periods appear afterwards. The fifth peak period (E) occurs between 2016-01-10 and 2016-05-25, reaching a peak of 140 events per day. The sixth peak period (F) comes form 2016-05-25 until 2016-07-12, with an anomalous spike from the rest of the data inside the same sixth peak period, that reaches up to 240 events per day. Before the seventh peak appears, a low-activity period of 10 events per day (average) is present form 2016-07-12 until 2016-09-05, and afterwards, the last and seventh peak period (G); characterized by high variance in the events per day, ranging from 10 to 80 events per day. Finally, the seventh peak period decreases until reaching 0 events per day on 2016-10-30, closing the dataset used on this work. Notice from the Figure 7.10 that the peaks B, D, E, F and G, showing an increase in events, occur in similar moments as some of the reported reported eruptions at Mt. Bromo.

After obtaining the total number of events from the entire data period, an inspection was made to the detections from the selected stations (SP01, SP03, BB05, KRK, and BLJI) in order to check the contribution of each station to the total number of events.

The Figure 7.10 shows the total detections per day for each of the selected stations. The permanent stations as KRK and BLJI present huge gaps of detections during the recording period. Also, there are days inside the entire period where the detections per day reaches zero for all the stations, and others where the number exceed 1'000 detections per day, as the case of KRK in the beginning of 2015, and BLJI in the end of 2016.

All of the stations illustrated in Figure 7.10 coincide with an spike of detections at the beginning of 2016, which lasts near 2 months. Besides this phenomenon, the rest of the spikes seems to be unique for each of the stations, such as the huge increases in detections per day for BLJI and KRK at the end and the beginning of the entire period, respectively. Stations like SP01, BLJI, KRK and SP03 shows sometime controlled values around or below the 200 detections per day, while the station BB05 overpasses this, showing a controlled detection rate around the double (400 detections per day).

To observe the contribution of the detections to the final number of events (see Figure 7.9), the ratio of detections from the selected stations over the total number of events per day was computed. to this we refer to the ratio of associated events (see Figure 7.11).

The graphs from the ratio of associated events (Figure 7.11) shows that, in most of the data period, only 20% of the detections on each station are associated. Also, they all show that during the beginning of the data period (2015-01-01 to 2015-03-02) there is an slight peak in the associated ratio. Some of the stations (SP01 and SP03) present a wider increase-decrease transition than others, and permanent stations (KRK and BLJI) evidence the same gap as the ones found at the total detections per day graphs, in the same stations (see Figure 7.10). Nevertheless, all the stations are consistent with an abrupt increase in their ratio between the date 2015-11-27 and 2016-03-03, which even can reach up to 80% of the detections associated to events from the entire network, and afterwards, the graphs share another increase in the ratio between the dates 2016-03-03 and 2016-06-02, specially in the station SP01 and SP03. Finally, the last increase to been seen in all stations with the exception of BLJI is another slight increase at the end of the period, which goes from 2016-08-31.

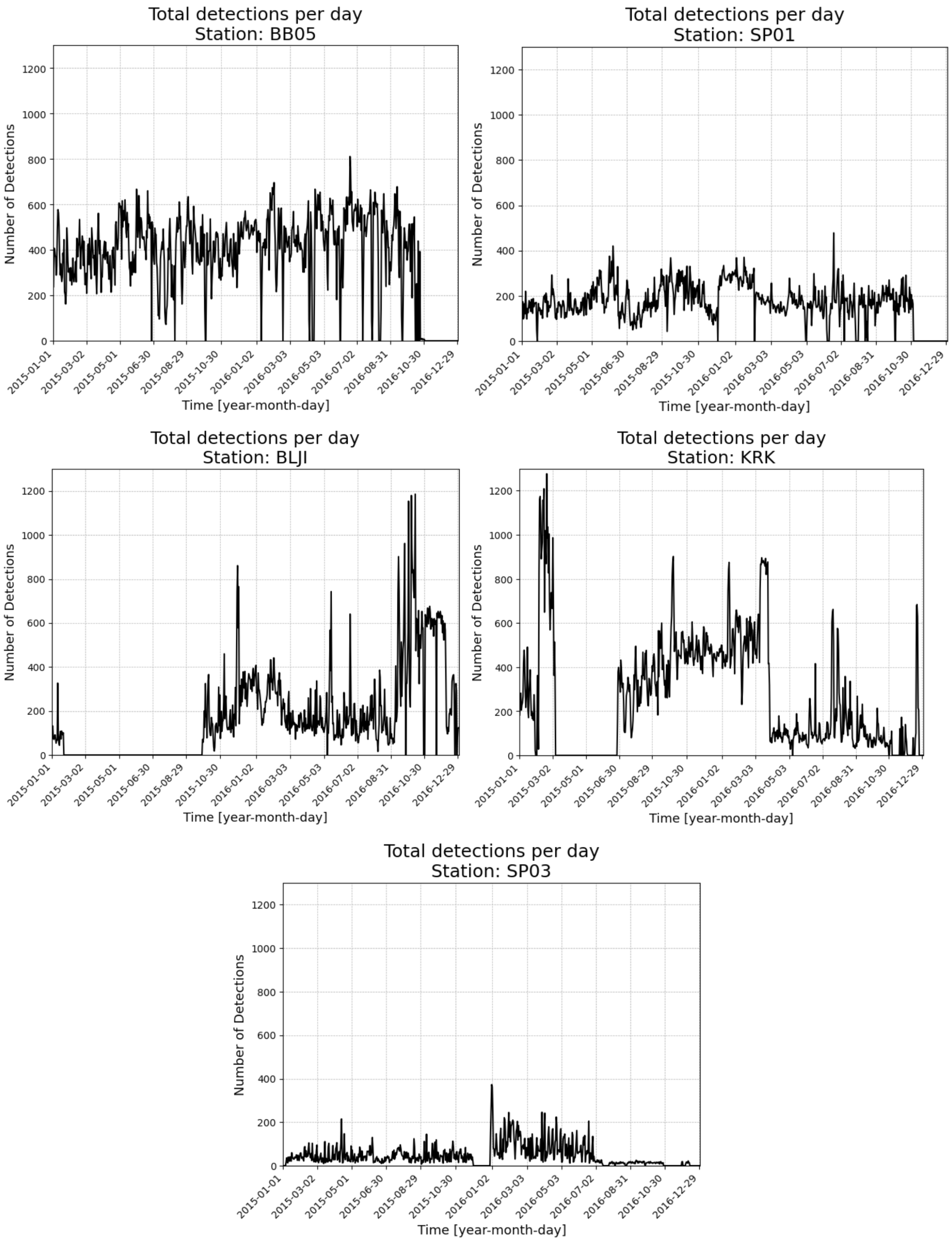

Figure 7.10: Number of detections per day for stations SP01, BB05, KRK, BLJI and SP03 in the entire period. The detections are with the MCCT method and before association step.

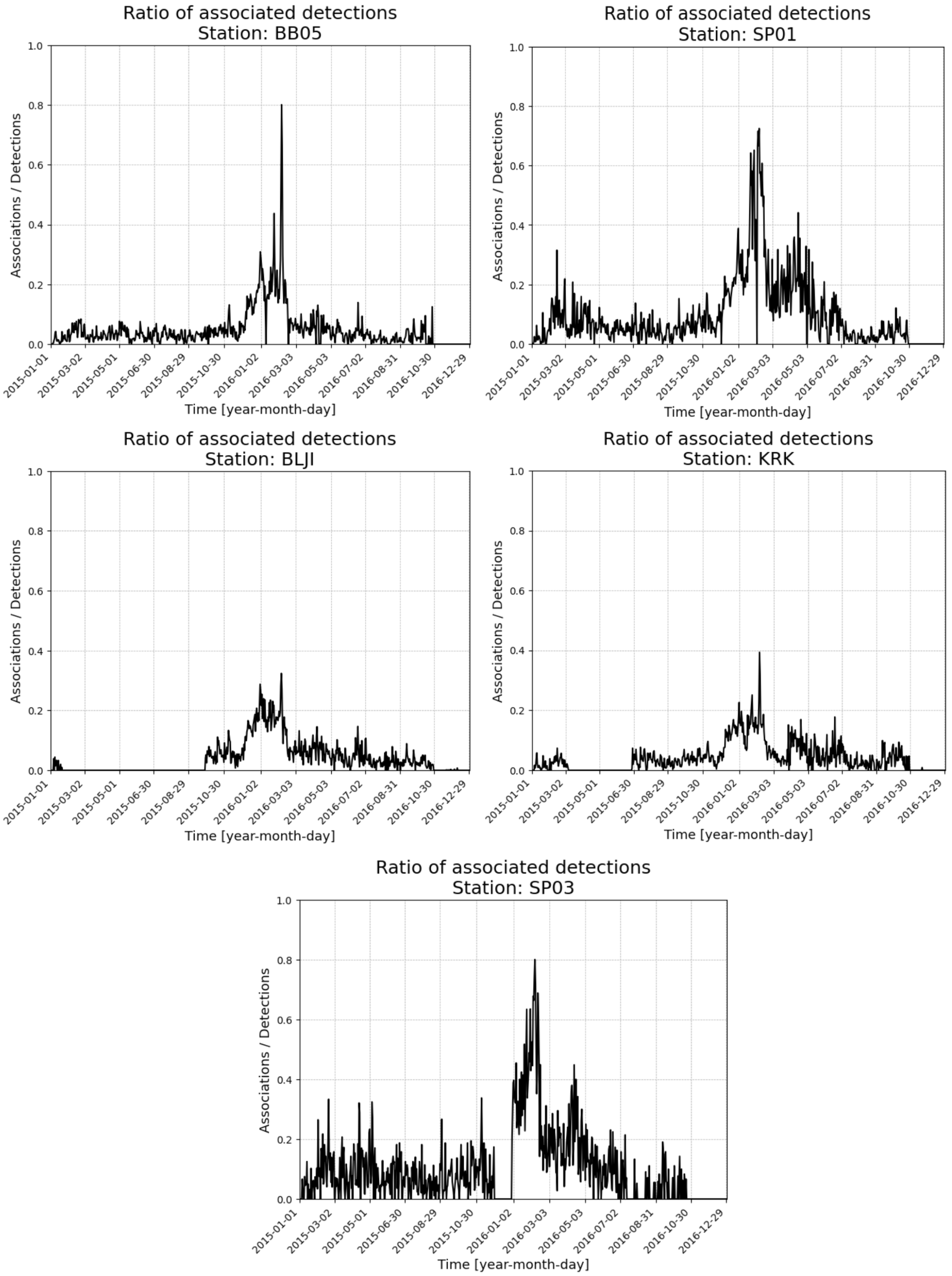

Figure 7.11: Ratio of associated detections over total detections per day for stations SP01, BB05, KRK, BLJI and SP03 in all the entire period. The ratio is between the individual detections on each stations and the total events registered by the network on each day.

7.3 Polarization Analysis

The polarization analysis was done to all of the detections associated to an event, meaning that for all the individual waveforms from each station involved in an event, the following quantities were computed: 1) rectilinearity, 2) planarity, 3) incidence angle, 4) azimuth, 5) back-azimuth, and 6) ratios between the largest eigenvalue λ_1 and the smallest ones λ_2 and λ_3. However, for validation only the polarization analysis from the selected stations are displayed, as seen in Figure 7.12.

A noticeable aspect at first sight on the plots from Figure 7.12 is the big difference on the computer values between the stations near the AW volcanic complex (SP01, SP03, and BB05) and the permanent BMKG stations (KRK and BLJI). The AW stations tend to show constant planarity and rectilinearity values along the recording period, and both features are closely related, or behave in the same way. However, large reductions in these values are present in several time ranges: 1) from 2016-11-30 until 2016-03-01, and 2) from 2016-03-30 until 2016-07-30. This is mostly observed in the results from the stations SP03, SP01, and slightly BB05 (see Figure 7.12). Also, the station KRK seems to show part of the second reduction period in rectilinearity and planarity values. The average values without taking into account the reduction periods is of 0.98 for the planarity in the AW stations, and their reduction in the mentioned time-ranges can reach down to 0.7. On the other hand, the rectilinearity presents average values of 0.92 on the AW stations, without taking into account the reduction periods, where the reduction can reach below 0.8, and even to 0.5 on station SP01.

The incidence angle is also displayed for the events on each station. It is important to remember that for hgih values of incidence angles, the ray arrival is mostly horizontal, whereas for low values, it indicates its mostly vertical. As shown in Figure 7.12, only the stations in the AW volcanic complex shows a sort of reflection pattern on the incidence angle data, having a reflection axis as a horizontal line between 40° and 50°, where there exists less density of points for the AW stations. Nevertheless, it must be clarified that this is not complete reflection, as each data point is unique on the plot. In this sense, some ranges of incidence angles appear also with other ranges and shows interesting things.

The events captured at the station BB05 shows wide ranges; from 10° to 45°, and from 45° to 90°. During the reduction periods, a dense cloud of data starts to appear between the two ranges.

On the station SP03, the phenomenon is different. 3 ranges of incidence angles appear on the plots; from 15° to 45°, from 45° to 73°, and from 73° to 82°. It is not until the reduction period starts when the station begins to present a dense area of points from 80° to 90°.

On the station SP01, the two ranges seen are from 15° to 30°, and from 60° to 90°. A significant gap is observed between 30° to 60°, however, this gap is filled with data on the reduction periods, and the density of points increase at near 90°.

The permanent BMKG stations show different behaviors from the previously described on the AW stations. The ranges of incidence angles are not clear, as they cover mostly all of the possible values; from 0° to 90°. A big exception is the station KRK, after his second gap of information (2016-04-01). There, the incidence angles ranges from 0° to 18°, and from 70° to 90°, breaking with the wide and unclear patterns showed before.

In all the stations, the eigenvalue ratios are consistent with the rectilinearity and planarity, as it shows similar behavior (see Figure 7.12). When the coefficient value of rectilinearity and planarity reduces, the ratios between the eigenvalues increases. It is consistent that the ratio λ_2/λ_1 is always higher than the ratio λ_3/λ_1, and mostly follows the same behavior. In the reduction periods, the λ_2/λ_1 ratio reaches or exceeds the 0.5 value in stations SP01 and SP03. Since the values in rectilinearity and planarity does not shows large changes for BB05, the eigenvalue ratios also follows this behavior, and λ_2/λ_1 mostly do not exceed 0.5. Regarding the stations KRK and BLJI, there is also no information in the reduction periods due to the gaps. For this stations, the λ_2/λ_1 values can reach to 1.0 in the rest of the available results.

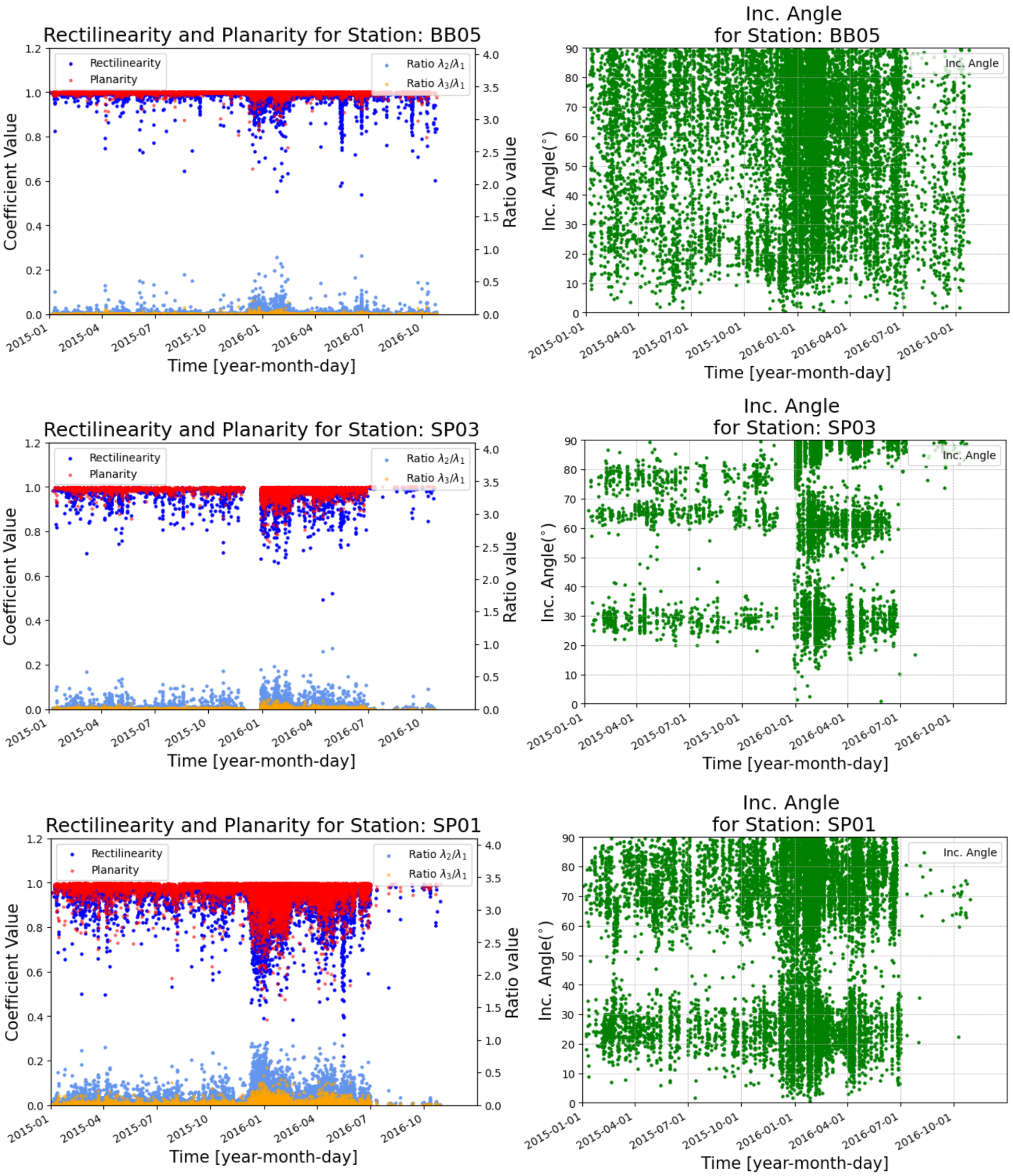

Figure 7.12: Polarization analysis results for station BB05, SP03 and SP01 in all the recording period. The analysis was done exclusively to detections from each station that were associated into an event. For each station, the polarization analysis graphs illustrates: 1) the rectilinearity (blue) and planarity (red) coefficient values, with the λ_2/λ_1 (light-blue) and λ_3/λ_1 (orange) eigenvalue ratios on the left side, and 2) the incidence angle (green) on the right side. The ratios are assumed within the following eigenvalues relation: $\lambda_1 \geq \lambda_2 \geq \lambda_3$. The gaps of results in specific time-periods are due to nonexistence of data for those periods in the specific station, or unavailability of all 3-component data.

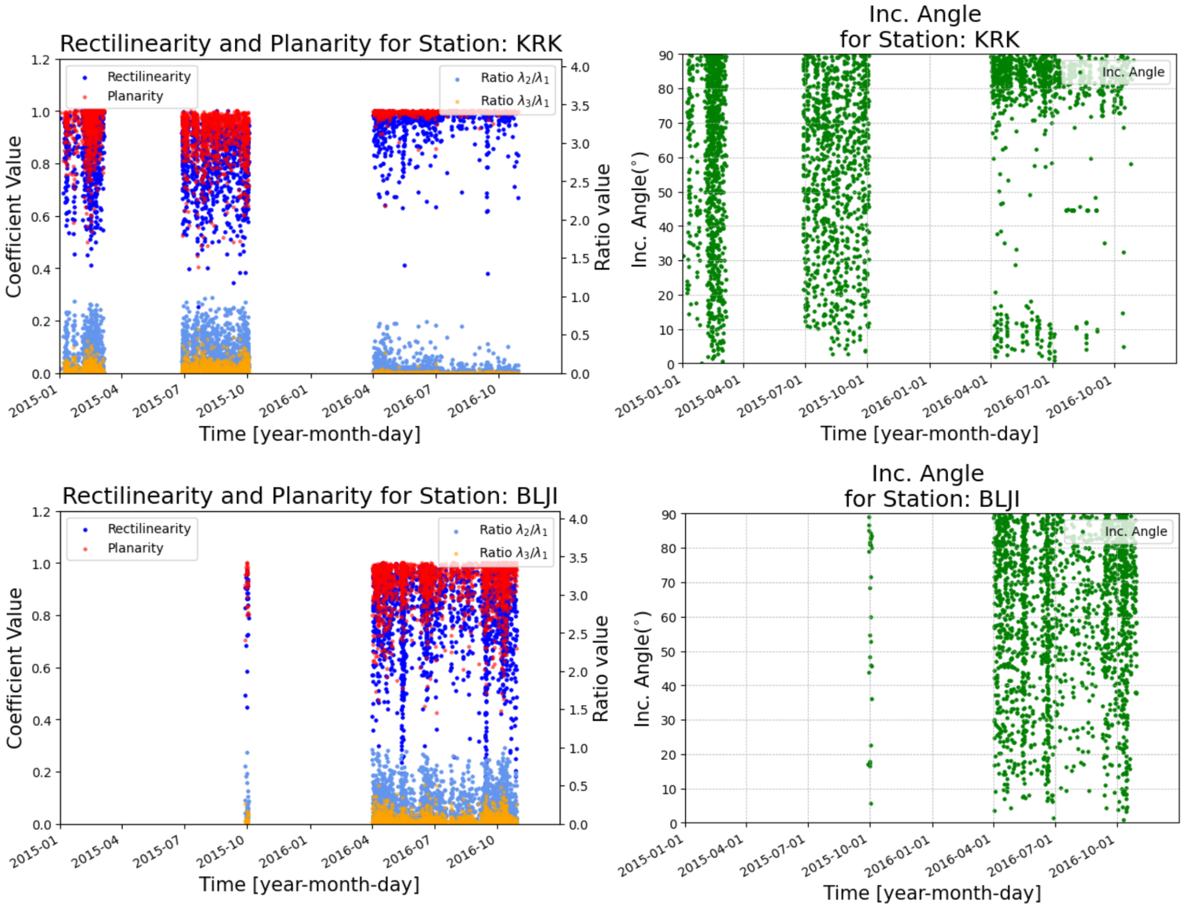

Figure 7.12: (Continued) Polarization analysis results for station KRK and BLJI in all the recording period. The analysis was done exclusively to detections from each station that were associated into an event. For each station, the polarization analysis graphs illustrates: 1) the rectilinearity (blue) and planarity (red) coefficient values, with the λ_2/λ_1 (light-blue) and λ_3/λ_1 (orange) eigenvalue ratios on the left side, and 2) the incidence angle (green) on the right side. The ratios are assumed within the following eigenvalues relation: $\lambda_1 \geq \lambda_2 \geq \lambda_3$. The gaps of results in specific time-periods are due to nonexistence of data for those periods in the specific station, or unavailability of all 3-component data.

Later, the results of the classification between P and Rayleigh waves by the conditions mentioned in Chapter 6 is shown in Figure 7.13. The classified events with acceptable number of P-waves were much higher than the Rayleigh waves. From Figure 7.13, the first 2 peaks (A and G) shows a constant variation of low values on Rayleigh arrivals. It shows an increase/decrease behavior that cover both peaks. Afterwards, the Rayleigh events shows their highest increase during the eruption period on peak D, which behaves in a similar way as the curve of P events. A slight increase/decrease of Rayleigh events happens at peak E, which also covers with two little jumps on the curve for peak F. Thereafter, no Rayleigh activity is shown until reaching peak G, which shows very weak increases on peak G.

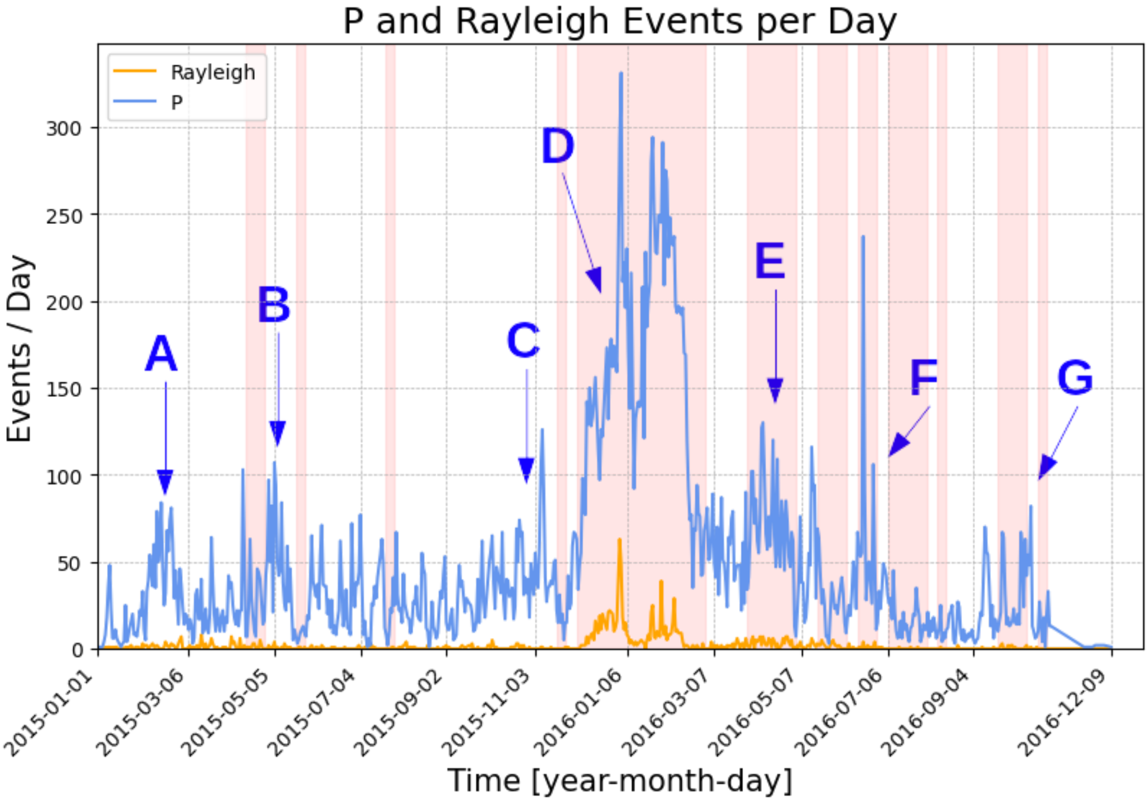

Figure 7.13: Number of classified P and Rayleigh events per day across the entire period. The red areas represents eruption periods of Mt. Bromo (Venzke, 2016). The main peaks identified are labeled with letters from A to G.

7.4 Event Locations

The following subsections show the location results of the events that occurred during the identified peaks in the previous section (peaks A to G; see Figures 7.9 and 7.13). However, only location results with RMS between calculated and measured travel-time differences equal or lower than 1.0 are shown since is the standard for reliable results (SCEDC, 2013; Tsapanos, 2014).

Period A: 2015-01-31 to 2015-03-02

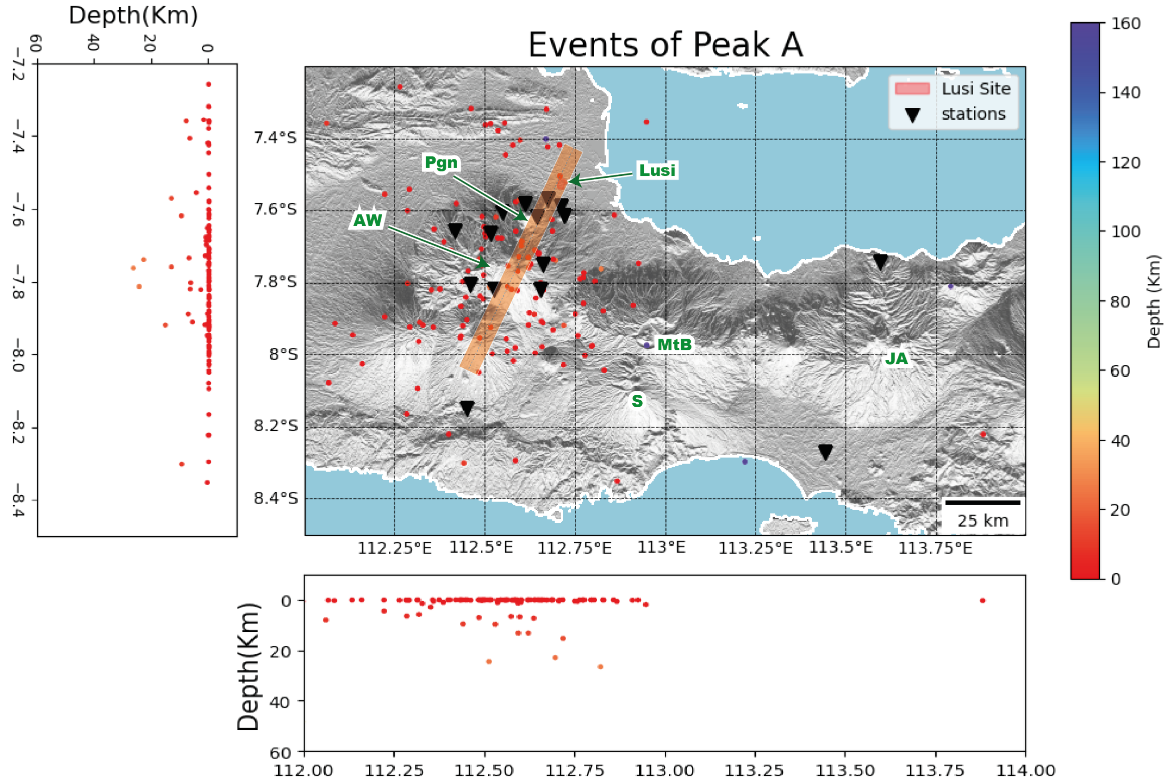

Figure 7.14: Events on map and in cross-sections (latitude and longitude) corresponding to the identified peak period A, with RMS ≤ 1.0. The main volcanoes are labeled in green letters. **AW**:Arjuno-Welirang, **Pgn**:Penanggungan, **MtB**: Mt. Bromo, **S**:Semeru, **AW**:Jyan-Argapura. The Watukosek fault zone is shown with an SW-NE trend orange area.

The Figure 7.14 shows the location of the events corresponding to the peak period A. Most of the events are located around the AW volcanic complex, saturated at 0 Km depth, with some extensions to Mt. Bromo and Semeru. Some of the events located between Mt. Bromo and the AW complex can reach down to 30 Km depth, and tends to reach the surface at AW.

Also, to the NW of the map, there are clear events from 0 to near 10 Km depth, following the lineaments of the main anticlines that rises above from the East Java Basin (Central Deep).

Period B: 2015-05-01 to 2015-05-20

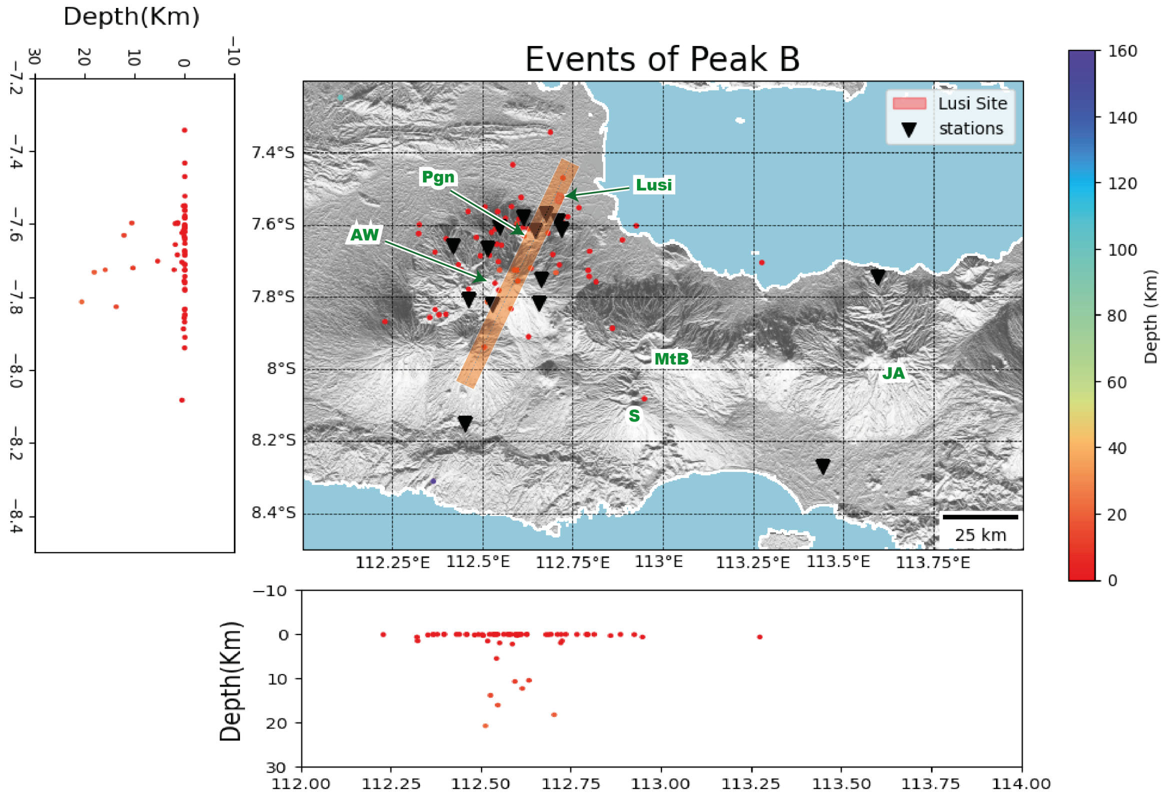

Figure 7.15: Events on map and in cross-sections (latitude and longitude) corresponding to the identified peak period B, with RMS ≤ 1.0. The main volcanoes are labeled in green letters. **AW**:Arjuno-Welirang, **Pgn**:Penanggungan, **MtB**: Mt. Bromo, **S**:Semeru, **AW**:Jyan-Argapura. The Watukosek fault zone is shown with an SW-NE trend orange area.

The Figure 7.15 shows the location of the events corresponding to the peak period B. Mostly all of the events still are located in the AW complex with near 0 Km depth. Other sources are beneath the AW complex down to 22 Km depth, however, this time there is no clear events-trend between Aw and Mt. Bromo or Semeru. Only 2 events are spotted on top of Mt. Bromo, specially near the crater of the Semeru volcano.

Period C: 2015-09-15 to 2015-11-20

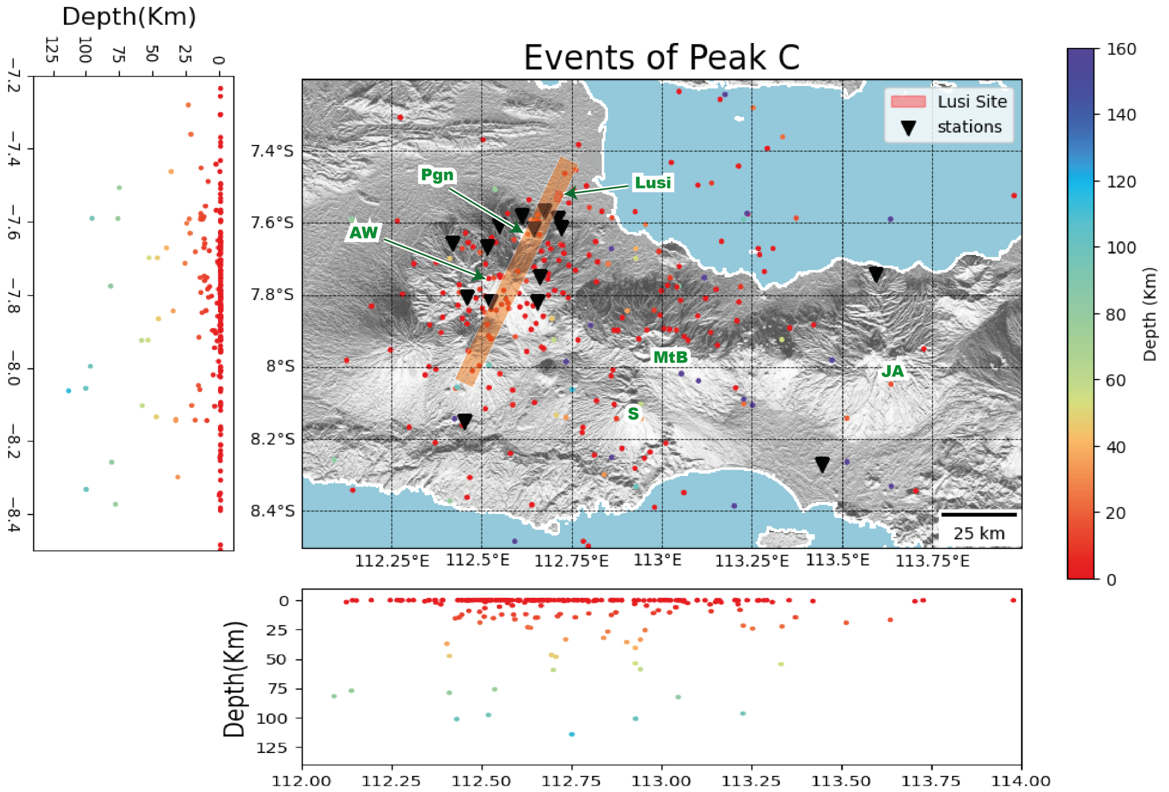

Figure 7.16: Events on map and in cross-sections (latitude and longitude) corresponding to the identified peak period C, with RMS $\leq$ 1.0. The main volcanoes are labeled in green letters. **AW**:Arjuno-Welirang, **Pgn**:Penanggungan, **MtB**: Mt. Bromo, **S**:Semeru, **AW**:Jyan-Argapura. The Watukosek fault zone is shown with an SW-NE trend orange area.

The Figure 7.16 shows the location of the events corresponding to the peak period C. Some events started to appear around Mt. Bromo and Semeru volcanoes with depth reach down to 50 Km depth. There are also some events coming from even below, down to 125 Km depth. Some of the events follow clear lineaments on map such as the one SE to Semeru volcano and the outer crater on Mt. Bromo. Only 5 events start to extend more to the East of Mt. Bromo (Lamongan volcano).

Period D: 2015-11-20 to 2016-03-01

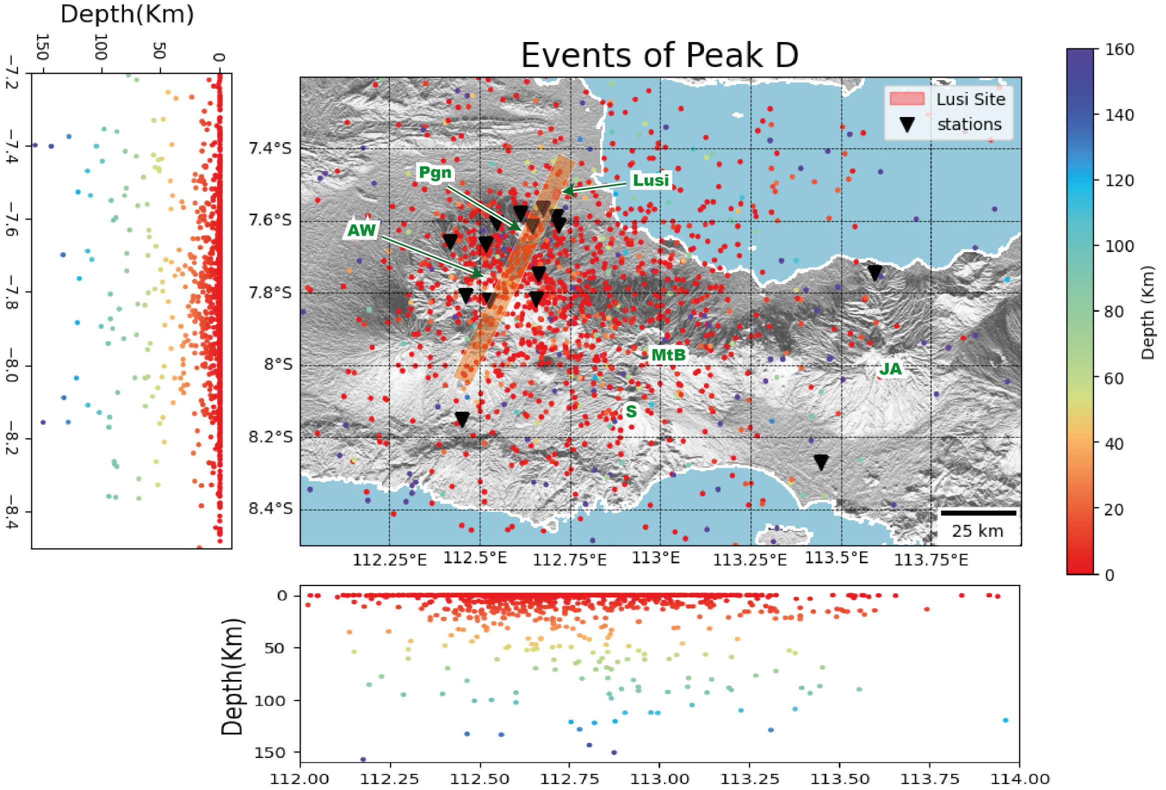

Figure 7.17: Events on map and in cross-sections (latitude and longitude) corresponding to the identified peak period D, with RMS ≤ 1.0. The main volcanoes are labeled in green letters. **AW**:Arjuno-Welirang, **Pgn**:Penanggungan, **MtB**: Mt. Bromo, **S**:Semeru, **AW**:Jyan-Argapura. The Watukosek fault zone is shown with an SW-NE trend orange area.

The Figure 7.17 shows the location of the events corresponding to the peak period D. The highest peak of events shows dispersed cloud of events with main focus on the AW volcanic complex and extends until covering Mt. Bromo and Semeru volcanoes. Some of the events follows lineaments such as the anticlines of the East Java Basin (NW of the map), and a SW-NE trend crossing the AW volcanic complex. Some few falls over the Iyan-Argapura volcano. More deeper events between 50 and 130 Km start to appear, and events up to 50 Km depth shows again a event-trend seen in peak C and A, which goes from the AW volcanic complex to Mt. Bromo.

Period E: 2016-03-20 to 2016-05-01

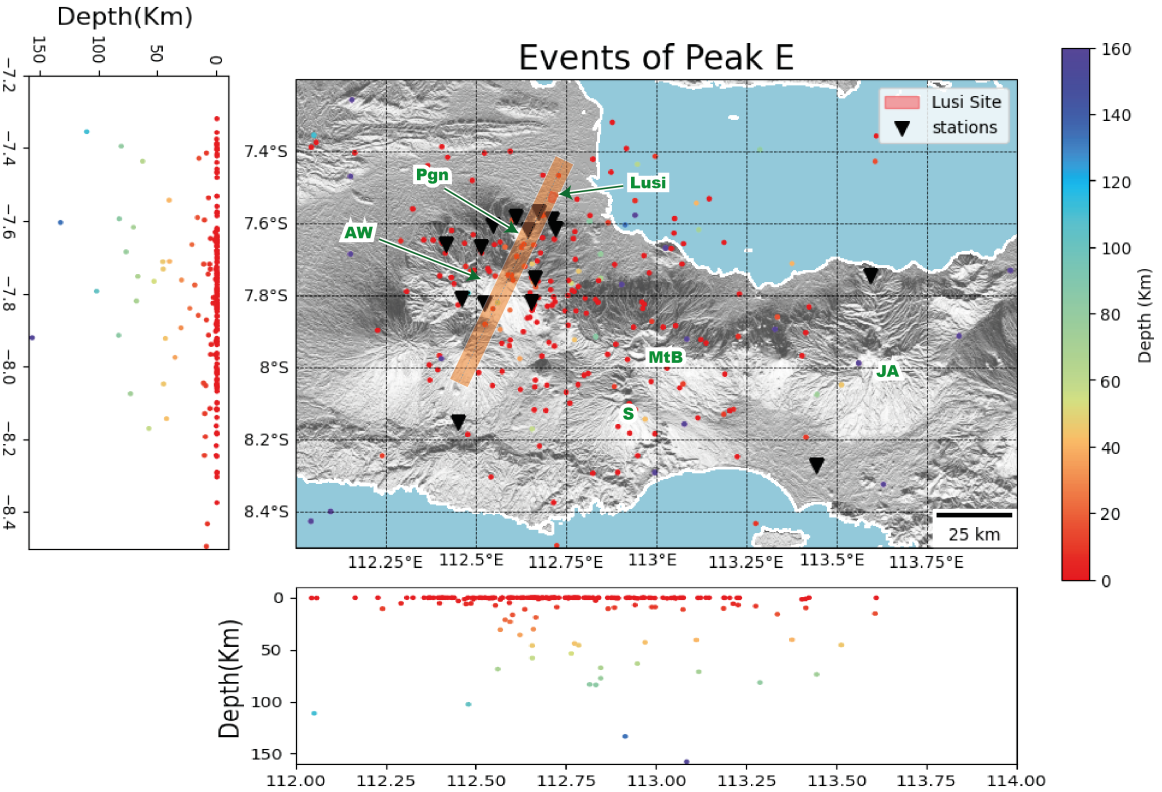

Figure 7.18: Events on map and in cross-sections (latitude and longitude) corresponding to the identified peak period E, with RMS ≤ 1.0. The main volcanoes are labeled in green letters. **AW**:Arjuno-Welirang, **Pgn**:Penanggungan, **MtB**: Mt. Bromo, **S**:Semeru, **AW**:Jyan-Argapura. The Watukosek fault zone is shown with an SW-NE trend orange area.

The Figure 7.18 shows the location of the events corresponding to the peak period E. Most of the events are still concentrated at near 0 Km depth, with a dispersed cloud covering the AW volcanic complex and Mt. Bromo. some events are presented from 20 to 50 Km depth, but only below the AW complex. Others also appear from 50 to 10 Km depth. Some of the events on Mt. Bromo have a similar characteristic to other events at the same place, which is that the events are never placed at the top of the crater, but rather they surround it as delimiting the border of it.

Period F: 2016-05-15 to 2016-07-10

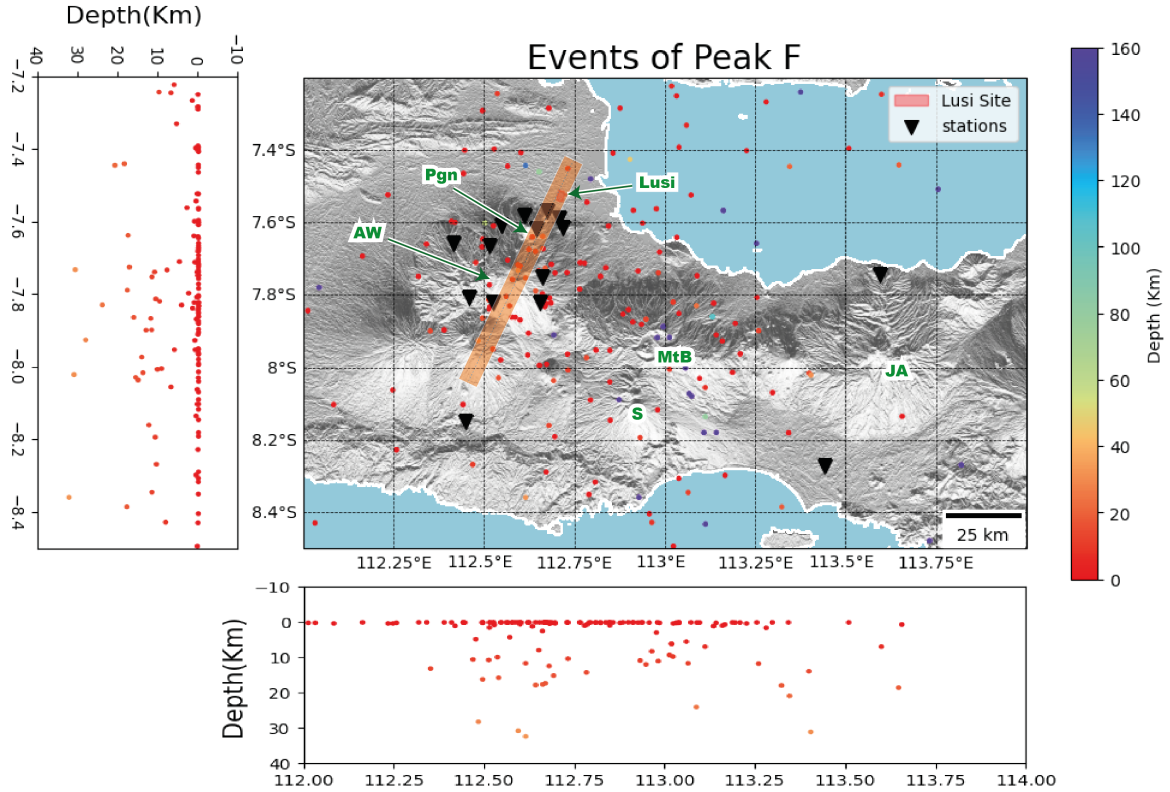

Figure 7.19: Events on map and in cross-sections (latitude and longitude) corresponding to the identified peak period F, with RMS ≤ 1.0. The main volcanoes are labeled in green letters. **AW**:Arjuno-Welirang, **Pgn**:Penanggungan, **MtB**: Mt. Bromo, **S**:Semeru, **AW**:Jyan-Argapura. The Watukosek fault zone is shown with an SW-NE trend orange area.

The Figure 7.19 shows the location of the events corresponding to the peak period F. The events still covers the AW and Mt. Bromo volcanoes. However, in this period more events at Mt. Bromo start to appear from 5 to 20 Km depth since the last peak. The event zones located separately under AW and Mt. Bromo volcanoes tend to reach one another between 10 and 20 Km depth.

Period G: 2016-09-04 to 2016-12-31

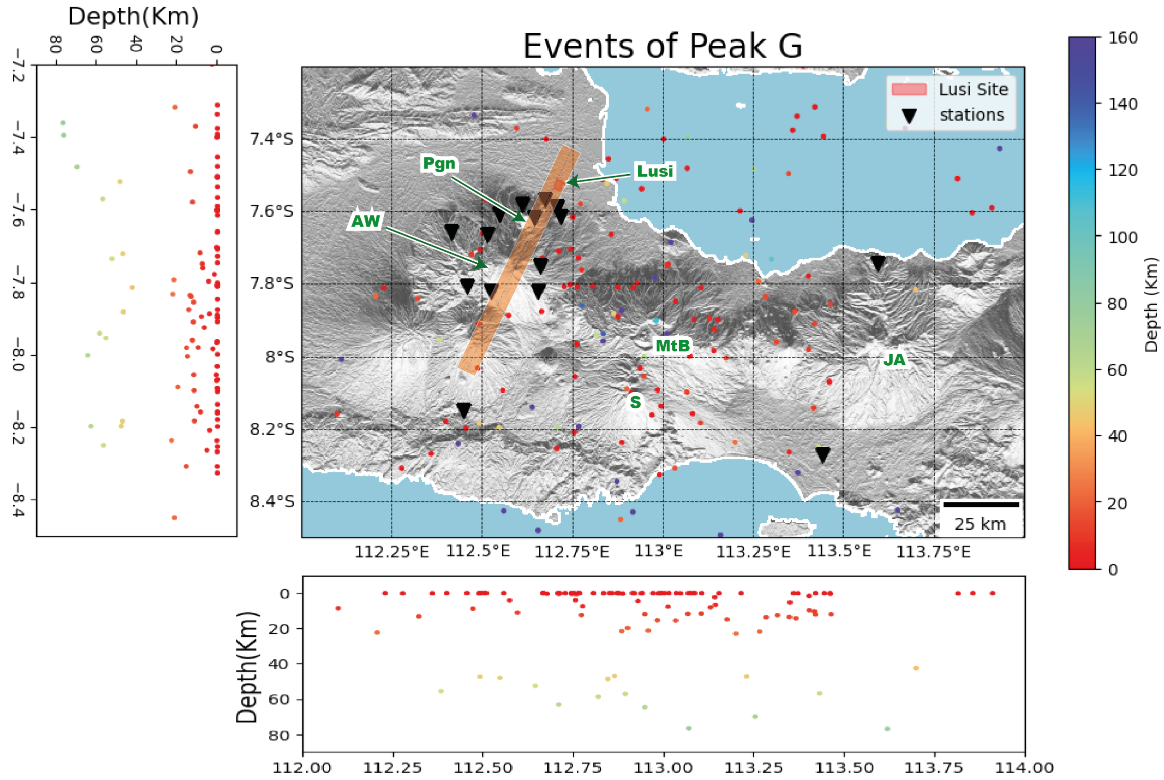

Figure 7.20: Events on map and in cross-sections (latitude and longitude) corresponding to the identified peak period G, with RMS ≤ 1.0. The main volcanoes are labeled in green letters. **AW**:Arjuno-Welirang, **Pgn**:Penanggungan, **MtB**: Mt. Bromo, **S**:Semeru, **AW**:Jyan-Argapura. The Watukosek fault zone is shown with an SW-NE trend orange area.

The Figure 7.20 shows the location of the events corresponding to the peak period G. The AW volcanic complex lost density. Now the events cloud is more centered on Mt. Bromo and Semeru volcanoes. Some overlapping of events can be observed at 10 to 20 Km depth, between the events below Mt. Bromo and Iyan-Argapura. Also, more evident in this peak, there also appears events in the sea (NE part of the map), near the same latitudinal level of the the anticlines of the Eat Java Basin on the NW part of the map.

7.5 Location Uncertainties

In order to evaluate the uncertainty of the location results, the simple Root Mean Square (RMS) error was used, which is the quadratic mean of the travel-time residuals between the calculated and the observed arrival-times, and normalized with respect to the error pick used (0.2 sec, see Table 6.2). Acceptable solutions are then defined when the RMS error is $\leq$ to 1.0.

In total, 32'787 events were located, where only 3'965 were taken as acceptable solutions. The Table 7.3 shows a comparison between the acceptable location solutions and the total events located at each peak of events. All the reliable locations represent mostly between 10% and 20% of the total events at each peak.

Table 7.3: Quantities of acceptable solutions (RMS $\leq$ 1.0) compared with the total located events.

Peak	**A**	**B**	**C**	**D**	**E**	**F**	**G**
Accepted Locations	154	80	374	1'814	328	281	250
Total Events	1'333	938	2'643	14'313	2'876	2'325	1'415
Percentage (%)	**11.55**	**8.53**	**14.15**	**12.67**	**11.40**	**12.09**	**17.68**

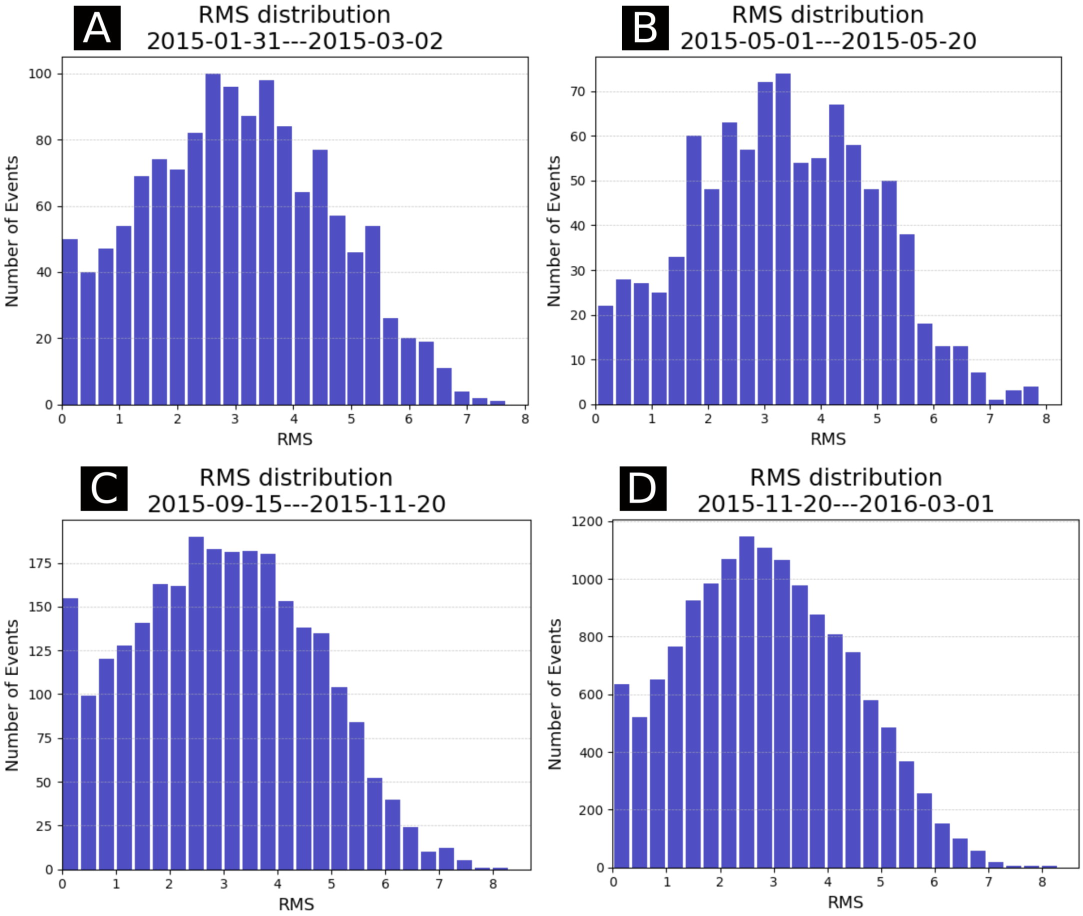

Figure 7.21: Distribution of Root-Mean-Square (RMS) values between theoretical and measured arrival-time differences for all location of the events in the peaks A, B, C and D.

The Figures 7.21 and 7.21 shows the RMS distribution between theoretical and measured travel-time differences as station pairs from event locations (travel-time residuals). All the distribution histograms show that most of the events errors in all peaks have a RMS gaussian-type distribution, with center around 3.0, and rarely overpass the 8.0. However, they all present an slight high number of events with RMS near 0.0, a decrease of it towards 0.5, and from them an increment until reaching near 3.0.

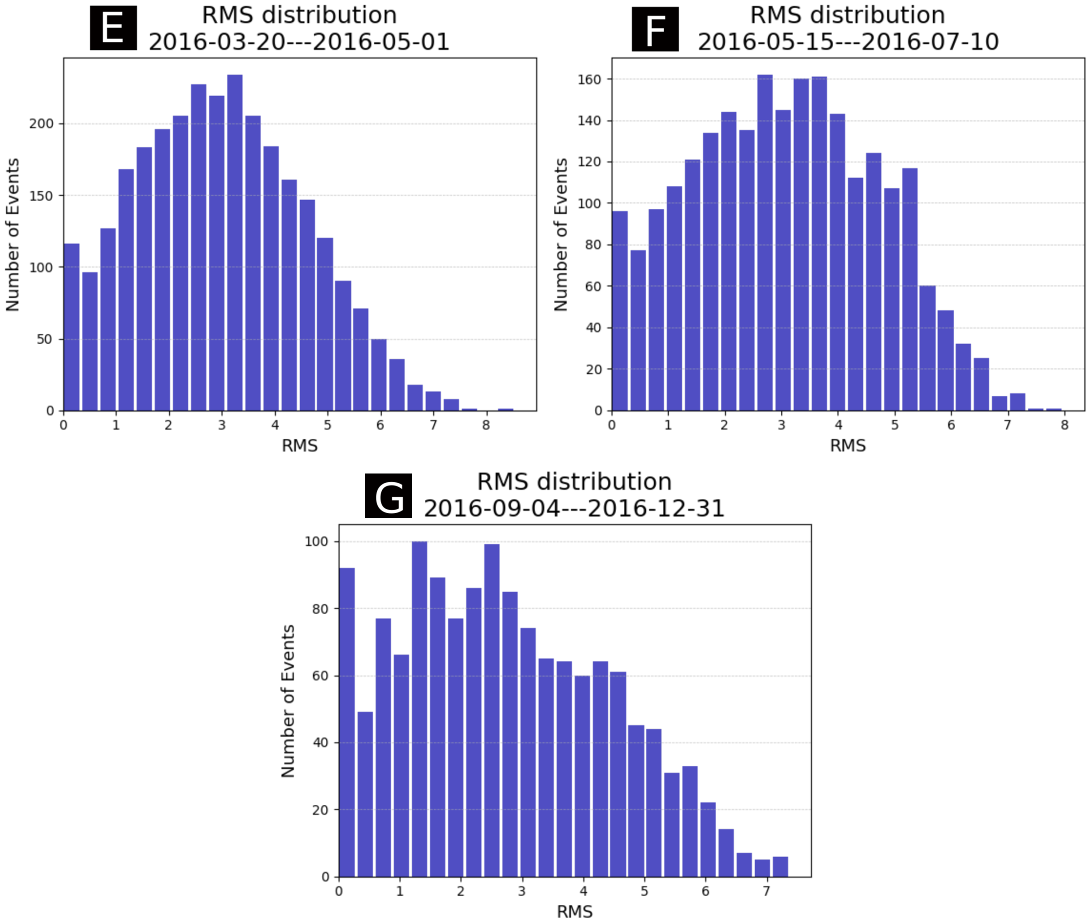

Figure 7.21: Distribution of Root-Mean-Square (RMS) values between theoretical and measured arrival-time differences for all location of the events in the peaks E, F and G.

CHAPTER 8

Discussion

8.1 Detection

Most of the signals in the pre-filter band used (0.3-1.5 Hz) have weak first-arrival impulses, and sometimes not distinguishable at first sight. These signals normally tend to be the ones recognized as the tremors (Minetto et al., 2019). They are embedded in another continuous tremor with lower frequency content.

The best initial method for detection was achieved by the Recursive STA/LTA. It allowed, with high computational efficiency, to draw a quick jump in the characteristic function, and later on, an exponential decay transient that allows to cover the energy dissipation of the event. This method was then ideal for the detection of the signals in the 0.3-1.5 Hz pre-filter band, where some of them didn't show clear P-wave onsets, while in other cases it was clear. It allowed to establish an easy Trigger-On and Trigger-Off values to detect the signals, which were chosen in such a way to pick as near a possible the P-wave arrival time and a long duration of the event until the vanishing part. Nevertheless, the Trigger-On might have gave error in the attempt to retrieve the first-arrival. The low Trigger-On value allowed in some of them a good estimation of the P-wave arrival time, but also it increased the sensibility so that, in some cases, impulses before the wave-train were picked as the P-wave arrival time.

In terms of the MCCT method, the performance is debatable. On one hand, the results of the MCCT detections compared to the detections of on individual channels by the Recursive STA/LTA showed that the number of detection by the MCCT method do not exceed the maximum value across the components, which tend normally to be achieved between the E and the Z components (see again Table 7.1). This proves that the MCCT method was able to discard false detections in individual channels by comparing the overlaps between all the channels. Also, it allowed to mark detections that where not seen, normally on the Z channel, as most of the detections of the MCCT were higher than the smallest number achieved from the components. And furthermore, the method proved to give precision on approximating to the first-arrival pick as it was more resolvable in other other components than just the vertical one. On the other hand, the ratio of durations over an entire day for several stations (see again Table 7.2) showed ratios above 1.0, indicating that the total summed time of all the events detected in a day by the MCCT is higher than the total time of a day, which evidently can't be possible. This revealed that it is due to an error in the MCCT algorithm, illustrated in Figure 8.1.

During the overlap comparison, there are situations where 2 detection windows in the same channel overlap with a larger detection window in another component. On the example (see Figure 8.1), 2 separated detections are noticed at the N and E components. However, the Recursive STA/LTA on the channel Z is not able to solve the 2 of them separately, but rather is sensible to the first detection, and so it interferes with the visibility of the followed one. In the overlapping and comparison process, the second detection is compared between N and E components, and is preserved as it appears in 2 out of the 3 channels. It adjust its start and end times according to the overlaps of the mentioned components. However, the first detection is the one that changes with the detection on the Z channels, and adjust its Trigger-On and Trigger-Off times according to the vertical component. This then results, as observed,

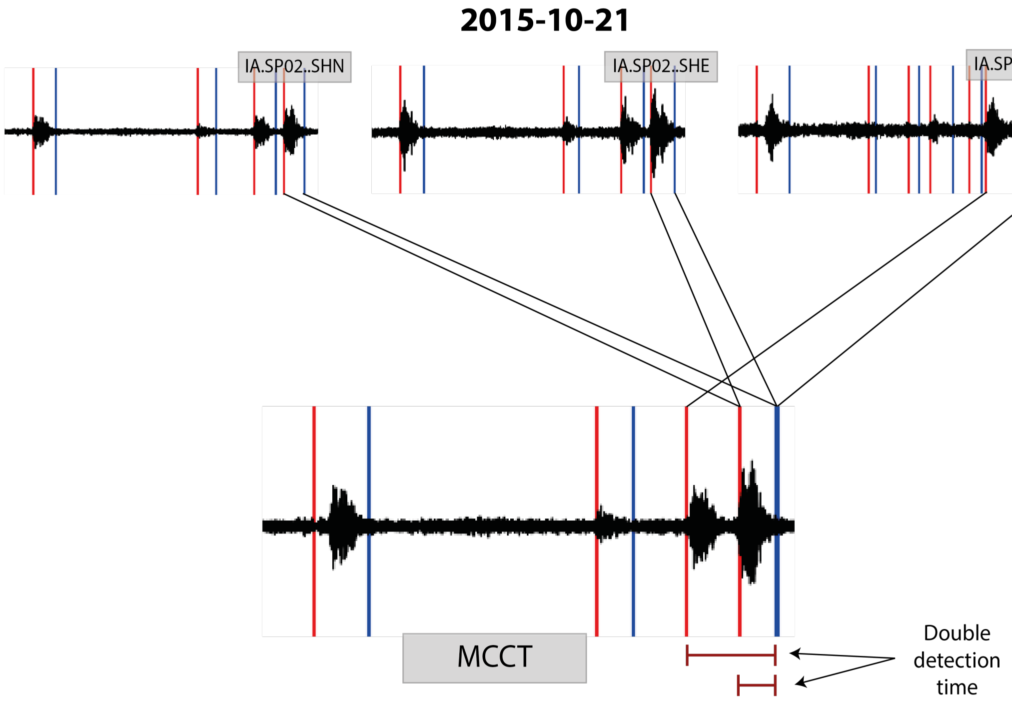

Figure 8.1: Illustration of event-window superpositions from the MCTT method. Counting double some of the durations was one of the side effects discovered after, however, they do not affect the steps further; association and location.

in detections with their time-windows overlapped, counting the durations twice. As noticed, this off course affects the duration statistics, as it is shown in the duration distributions with high number of events (see Again Figures 7.2, 7.4, 7.6 and 7.8). Also, due to high noise and the high sensibility of the Trigger-On and Trigger-Off values, and malfunctioning of the instruments, 2 events were embedded in a single time-window, meaning that they could not be solved individually at some stations.

Nevertheless, the problem on the MCCT method did not affect the first-arrival picks, since they still remain in their proper start-times as planned, and the association method is only based on the first-arrival picks. Therefore, the evidenced problem of the MCCT method does not affect further processes from the association step.

The Trigger-On and Trigger-Off values chosen for high-sensibility towards the first-arrival also brought many false picks, but was not due to the MCCT method. It is attributed to the high noise and malfunctioning of some data in several stations, specially the permanent ones (BMKG), as they presented many errors in the data. Also this is confirmed by the duration distribution of the events, where only the stations BLJI and KRK presented high number of events with durations lower than 1 minute, which could correspond to noise or instrumental spikes, and this was visually confirmed afterwards.

Besides the durations lower to 1 minute, other types of distributions in event durations and detections along the day shown what the data presents huge limitations in terms of quality. Noise and malfunctioning was a frequent phenomenon in the used data, as showed, as an example, by the histograms for the station SP03 in 3 out of the 4 dates chosen for detailed inspection. In the histograms (detections during the day and durations), the station detections showed no tendencies, patterns, or clear distributions while the other stations succeeded. Also, this was confirmed by visual inspection, not only on the station SP03, but also on several ones as BB10, SP17, BB05 and others.

The detections achieved are unlikely linked to human activity. The histograms of the distribution of detections during 24 hours present maximums towards afternoon/night hours (21:00:00 UTC-time), which is very different than human activity. Recent works, even during the COVID situation, as the ones by Diaz et al. (2020) and Lecocq et al. (2020), have somehow estimated the human activity by diurnal variations from seismometers near densely populated areas. They have shown how, in normal situations, the activity spikes up until reaching a maximum at 12:00 (mid day), and after this time it vanishes again, reaching minimums during the night, near 02:00 (morning). Even taking the time shift into consideration; (Indonesia (Java) time = UTC + 07:00), it would still not explain human activity, as the peaks would then pass to be early on the mornings (near 04:00). In addition, the human activity is detected by noise amplitudes (Diaz et al., 2020; Lecocq et al., 2020). According to Obermann et al. (2018), the human noise seems to range primarily between 2 and 3 Hz, different from the 0.3-1.5 Hz frequency range used. Also, Obermann et al. (2018) mention that the area is densely populated and the basin stations present noise because of it. This study used only bedrock stations, however, still there is population and human activity around.

It is clear that the detections throughout the entire period varies between stations as they are distributed in such a way for different purposes (i.e. regional earthquakes, seismicity at LUSI-AW, etc., see again Figure 7.10). Therefore, some stations are capturing certain events better than other ones, or might have superposition of two types of sources, such as LUSI-AW activity, with Mt. Bromo activity. Also, certain stations can have more noise than others during the period, which affects the graphs of detections. From Figure 7.10 it is difficult to establish a common ground between stations, except for the main eruptive periods of Mt. Bromo. However, this detections come to make sense once they are associated, as then they share common peaks, and thus, the number of associated events increases (see again Figure 7.11).

8.2 Types of Events

Recently it was mentioned that the pre-filter used does not match the human activity frequency range defined by Obermann et al. (2018). This means that the frequency band was made for finding the specific tremor signals, observed by Minetto et al. (2019). The total number of events (see again Figure 7.9) in the 2 years period showed several peak periods (labeled from A to G) that were identified, and only peaks B, D, E, F and G occurs in similar moments near volcanic activity from Mt. Bromo. The curve of total number of events describes well several eruption periods of Mt. Bromo, with a frequency range similarly to the ones explored by Minetto et al. (2019), and therefore it mostly likely that most of the detected events were generated from Mt. Bromo activity.

The selected pre-filter and the detection method was able to identify in a certain level the Type A and B events combined from Minetto et al. (2019). When the produced total number of events graph is compared with the one from Minetto et al. (2019) (see again Figure 3.7), it is shown that peaks A, B and C are concordant to peaks from Type B events, in shape and in quantity. However, the peak D, being the maximum peak, shows a different behavior.

Minetto et al. (2019) recognized the same increase coinciding with peak D, but at theirs, both in Type A and Type B events, start at mid January of 2016; near 2 and half months after the eruption activity (Venzke, 2016). In this study, the detection method proved to be more accurate on describing the volcanic activity, as the peak D starts developing quite at the moment where Mt. Bromo erupts (2016-12-02), which is not observable in the detections from Minetto et al. (2019). Also, the total number of events in the peak D overpasses the number of Type A and B events combined, which then shows the high sensibility of the parameters chosen for detection with the integrated MCCT method. Also, during the data inspection, the filter used by Minetto et al. (2019) was compared to the filter used in this study, and it was confirmed that the proposed filter in this work is able to achieve the fragmented tremors not seen by Minetto et al. (2019) during the beginning of the eruptive period (end of 2015).

Minetto et al. (2019) reported at the beginning of the eruption period a slow change from event Type B to Type A. According to the detections achieved here with the selected filter, it was observed that the presence of the Type A events were all the time of the eruption peak D. The Type A event (fragmented tremors) initially had a high energy in the frequency content overlapping the Type B events (continuous tremor); 0.3-0.9 Hz. Afterward, the Type B event lose its energy and only the Type A events remained while their frequency content increased from 0.9 to 1.5 Hz. Therefore, the detections achieve in this study expose that the fragmented tremors where present since the beginning of the eruption period, however, a clear change in eruption style pointed by Minetto et al. (2019) is also noticed afterwards by the continuous tremor decrease and frequency content increment from the fragmented tremors.

The peak D region present 2 maximum peaks, illustrated by a division from a decrease between the 2 (see again Figure 7.9). The uncorrected amplitudes graph from Minetto et al. (2019) was able to see this, but not the Type A and B number of events. Nevertheless, the number of detections achieved in this study (see again Figure 7.9) was able to solve this behavior.

From the histograms, is it possible to observe the type of events registered on peak C, D, and G. The histograms of 2015-10-15 represents the peak C, showing a duration of the detections from 1 to near 6 minutes. Specially, as pointed by all the station, except SP03 which presented errors, there is a common local maximum around 2 to 4 minutes of duration in the events and events around 1 minute or below, meaning that there was a lot of noise that was possibly picked.

On the peak D, described by the histograms of the day 2016-02-02, all the stations revealed events with consistent duration from 2 to 4 minutes, and they are similarly distributed across the day. Some of the detections around this date were visually inspected, and the apparent durations observed coincides with the ones reported on histograms, some of them with no clear first-arrival. These ones corresponds mainly to the Type A events observed by Minetto et al. (2019).

At the peak G the events detected have durations of 2 to 3 minutes and some of 5 minutes, which then seems to be longer than from peak D, which makes it similar then to the events from peak C in terms of duration. This peak seems to show a similar behavior as peak B and others ones that were not labeled in this study. There are several events peak that happens right after an eruption period of Mt. Bromo. This then means that some eruption periods are not consistent with a clear event peak as in D, E, or F, but it happen with a local minimum on the curve of the total events recorded, right before some peaks starts (B and G amongst the labeled).

8.3 Location and Dynamics

In all of the peaks, the RMS for arrival-time difference are quite high, and huge errors are shown by the distributions (see again Figures 7.21 and 7.21). Also, they all present saturated events at 0 Km depth, meaning that most of the events are superficial, estimated to be no more depth than 5 Km of depth.

To clarify, the differentiation between P-wave events and Rayleigh wave events might indicate the preferential type of events, but does not necessary means that the events were superficial or not. The criteria is meant to see whereas the picked first-arrival is could actually be considered a P-wave or not. This then opens the possibility that the Rayleigh class is just events where the first-arrival picked is not a P-wave, and therefore the phase could have arrived before or after.

Low RMS events from peak A indicate sources from the Penanggungan and the AW volcanic complex (see again Figure 7.14). This makes sense as this peak is not associated with any eruption period of Mt. Bromo. Also, even if the two mentioned volcanoes as sources of the events are dormant (Penanggungan and AW), there are still events manually picked by Obermann et al. (2018) which yielded in this location and thus confirms that also events can be around this area.

The reliability on other locations are mostly sure, as several appears in the lineaments of the anticlines at the exposed East Java Basin, which is consistent with the regional tectonic lineaments and their left-lateral movements (Istadi et al., 2009). This is mostly because across the data period many local and regional earthquakes were detected (see again Figure 6.4), aside with the tremor signals. The 1-10 Hz frequency band explored in the validation step of the detections showed to capture these events, but the spectrograms identified that the events also have energy in the lower frequencies as the 0.3-1.5 Hz range. This feature and their clear P-wave onsets made these events to be visible in the used pre-filter (0.3-1.5 Hz). The events from 10 to 30 Km depth appear mostly below the AW complex; bending towards and under Mt. Bromo (see again Figure 7.14). This could be interpreted as the magmatic connection beneath these volcanoes, as there is no distance greater than 50 Km between them. The connections between the magmatic chambers in the area may exists at these depths (Fallahi et al., 2017; Obermann et al., 2018); and in parts of Central-East Java (Haberland et al., 2014). Also, as a boundary, the Moho depth estimations are between 35 to 50 Km depth in Central Java (Wölbern and Rümpker, 2016; Rosid and Ramadhanti, 2019).

The case is similar to peak B, however, the connection between Mt. Bromo and AW complex is not shown (see again Figure 7.15). Only activity below the AW is observed. According to the graphs of detected events by the stations KRK and BLJI (permanent stations), they both exhibit a gap during the development of peak B. There are two possible interpretations at this peak. The first one is that the peak B corresponds only to the activity between the Penanggungan and the AW volcanic complex with the LUSI area, through the Watukosek fault zone, supported by the seismicity below the LUSI area, also indicating a link between them (Mazzini et al., 2007, 2009; Mazzini and Etiope, 2017; Miller and Mazzini, 2018; Obermann et al., 2018; Lupi et al., 2018). The second might be that, due to unavailability of the stations at this moment only the instruments over the AW complex were considered as the network. Therefore, without the extension of the network through the BMKG stations, then it is most likely for the Oct-Tree method to find a solution inside the coverage area of the instruments available, in the AW complex.

The peak C, covering almost 2 months, events show a clear concentration of events at AW, Penangunggang as usual, but now also in Mt. Bromo and Semeru volcanoes (see again Figure 7.16). Some of the events at Mt. Bromo and Semeru follows clearly lineaments such as the crater of Mt. Bromo and scarps of the Southern Uplift, right SW of Semeru volcano (Istadi et al., 2009). High activity is occurring in all the magmatic chambers and connections, as shown by the high number of events concentrated right below the AW complex, Watukozek fault zone, Mt. Bromo and the Semeru volcano, no below than 50 Km depth.

According to the eruption periods of Mt. Bromo (see again Figure 7.13; Venzke (2016)), there is no activity in the moment of this peak. The nearest eruption activity occurs at the beginning of the next peak period (D). This could support the predominance of deeper events than in the surface, which could be gas pressurization from the conducts as anticipation of the main eruption period, which occurred right at the next peak (D).

The great quantity of surface events (≤ 3.5 Km) could not be constrained. Some of them might even have larger depths than the ones reported. To explain why, it would be mention as example the locations of the events at peak (D) by Sukir et al. (2017). According to the authors, most of the events are located beneath Mt. Bromo, reaching up to 3.5 Km in depth. However, the network configuration around Mt. Bromo could not be able to solve with accuracy the location of superficial events since the distance between the stations is longer than the suggested depths. An effect of this is the observed saturation of events at different depth levels (0, 1, 2, and 3 Km), appearing as horizontal lines at the mentioned depths. Also, the polarization analysis at the moment of the peak period C shows high number of events with incidence angle from 60° to 80° at stations SP01 and SP03.

Most of the events where of type tremors, however, there were many events observed at peak C with volcano-tectonic characteristics (VT); clear P-wave arrivals and sometimes S-waves too (Hidayati et al., 2019), and verified visually and also from mostly no Rayleigh class events presented in this period. Their presence may represent some brittle fractures by magma migration from the VT, and resonance between fluids and cavities from the tremor signals (Jousset et al., 2013). According to models such as the ones by Haberland et al. (2014), it is possible that part of the VT events might come from pre-existing suture zones (faults) in the Southern Uplift, in response to high pressure interactions from magmatic activity at depth, which is known to happen (Satyana et al., 2004; Satyana, 2007; Moscariello et al., 2018; Mazzini, 2018). This interpretation is supported also with studies from White and McCausland (2016) and Hidayati et al. (2019), where they saw that strong increases in the number of VT events often precedes volcanic eruptions.

The peak D marks the biggest and main Mt. Bromo eruption during the study period (see again Figure 1.1b), not only because its the highest peak, but also because is the one who has been mostly studied and reported (Sukir et al., 2017; Minetto et al., 2019; Venzke, 2016, 2021). The events from this peak are composed by some VT, but mainly and majority by tremor impulses, which are the ones identified as fragmented tremors by Minetto et al. (2019), with durations from 2 to 4 minutes (see again Figure 7.6). A great part of the fragmented tremors do not show a clear emergent first-arrival impulse that could be detected, and so the methods just estimated the arrival-times. This is supported by the high amount of events with low rectilinearity and high eigenvalue ratios, which points towards an abrupt increase in the Rayleigh class for this period (see again 7.13) and are concordant to eruption activity since they share repetitive self-similar events (Hidayati et al., 2019).

The detections and data inspection with the selected pre-filter showed that, in difference with Minetto et al. (2019), the fragmented tremor (Type A) signals appear not 2 months after the eruption started, but right at the beginning, so it was a continuous repetitive signal through all the eruption period. Nevertheless, the continuous tremor (Type B) was strong at the beginning of the eruption, but their amplitude vanished one month after, letting the fragmented tremor signals to be be noticed clearly in the registers. From similarities with studies as Jousset et al. (2013), the continuous tremor can be attributed to particle emissions, which is an eruptive style confirmed for the period (ash cloud emission; Venzke (2016)). A closer look at the tremor signals shows no clear shape, which could indicate that they are multi-phase events (hybrids), and could incorporate explosion and emission at the same time due to their repetitive self-similar behavior (Jousset et al., 2013; Hidayati et al., 2019; McCausland et al., 2019). Therefore, a change in eruption style is noticed at the end of 2015 from the seismological aspect, however, bulletin reports are not clear in specific changes at this moment (Venzke, 2016).

The locations at this moment (see again Figure 7.17) are mostly concentrated no below than 40 Km depth. The great dispersion of locations at surface might be explained due to inaccuracy of first-arrival picks and the station network configuration very far from Mt. Bromo. However, events below 20 Km depth shows the high amount of activity that could be the continuation of events from peak C, as it has shown in other volcanoes to hold or increase this number of events (Hidayati et al., 2019).

The peak E (see again Figure 7.9) coincidences with another eruption period (Venzke, 2016), also noticed by Minetto et al. (2019). Also, it presents increments in Rayleigh events since the end of peak D, and visualization of them reveals more fragmented tremor signals similar to the ones at peak D, but with less amplitudes and more noise, which is possibly the continuous tremor identified by Minetto et al. (2019). Superficial events are mostly around the AW complex, Mt. Bromo and Semeru volcanoes, while trying to mark lineaments such as the Mt. Bromo caldera.

The peak F, also observed by Minetto et al. (2019), coincides with an eruption event (Venzke, 2016) shorter than the others (see again Figure 7.10). A high spike reaching near 240 events per day can bee seen at the beginning of the eruption period, and visually confirmed as noise. The events located between 5 to 20 Km depth falls directly below AW and Mt. Bromo volcanoes, and could be attributed to normal processes as thermal activity and degassing (see again Figure 7.19). Even if the locations are not well restricted, the polarization analysis (see again Figure 7.12) for station SP01 shows two main ranges on incidence angles; 10°-30° and 60°-90°, indicating incidence from below (AW) and from far (Mt. Bromo). The permanent stations are not able to perceive the events from the AW complex, but only from Mt. Bromo, as their incidence angle range is from 70°-90° for the peak period.

Finally, the last peak (G) also coincides with an eruption period of Mt. Bromo, and not marked by Minetto et al. (2019) (see again figure 7.10). Surface events tend to show a location at Mt. Bromo and

Semeru volcanoes (see again Figure 7.20). For the first time, a clear visualization of beneath connections are observed between Mt. Bromo and Jyan-Argapura volcanoes, indicating that Mt. Bromo not also have fluid/magmatic interactions with the AW volcanic complex, but also can develop certain dynamics with Jyan-Argapura. The AW complex and the Watukosek fault zone shows no significant activity. This observation aside with the deep events mentioned suggests that for this eruption period, Mt. Bromo change its deep interactions from AW to with the Jyan-Argapura volcano.

Most of the events might come from Mt. Bromo, and some from the AW volcanic complex since; 1) the pre-filter used target the same events studied by Minetto et al. (2019), 2) the event peaks over the entire dataset period can match some of the important eruption period from Mt. Bromo, and 3) some of their locations have shown to have a proximal locus from these structures (volcanic buildings). Nevertheless, most of the localized events presented high RMS values superior to 1.0, specially most of the ones near the surface and dispersed across the map. The high number of these events, which is suspected to be mislocated, can be explain due to first-arrival pick errors and also because some of them might have not been associated with arrivals at the permanent stations. The Oct-Tree method see then possible low error solutions within the network on top of the AW since there is no data from the BMKG stations used to extend the coverage. Therefore, this opens a debate over the methods used for the automatic processing of this earthquakes, in all of the proposed steps.

CHAPTER 9

Further Work

The events with low RMS values in differential arrival-times were able to explain some dynamics of volcanic behavior before and during the strongest eruption periods of Mt, Bromo. Still, a high number of non-acceptable locations (RMS > 1.0; see Figures 7.21 and 7.21) can not be ignored, indicating that improvements must be made in order to increase the accuracy, and have better results to describe the eruption evolution. Therefore, some suggestions are made to improve in further works with the same available data.

The Trigger-On and Trigger-Off values were set in such way in order to approximate to the first-arrival impulse. However, this also incremented the number of false detections. In consequence, it is suggested to increase both the Trigger-On and Trigger-Off, from 1.0 and 0.5 to 1.5 and 1.0, respectively. Also, for the MCCT method, a correction must be made in order to neglect repeated detections from the overlapped detection time-windows and just save a unique one.

After reinspecting the events, it was noticed that, even if the used association time-window of 20 seconds is near the theoretical correct value (30 seconds) for P-wave travel-time across the network, still does not work for most of the superficial events. The signals are detected due to an increase in amplitude (first impulse) compared to the rest of the record. In the case of this work, this increase is achieved mostly by surface waves since the first-arrivals motions are weak. Taking this into account, and the surface wave velocity (1.35 Km/s; Minetto et al. (2019)), a 20 to 30 seconds time-window for association is not enough. Visually, a 60 second window is needed so the events can be associated within all of the network. A 20 seconds window association proved to get rid of background noise (see again Figure 7.11), while an attempt with 60 seconds window increased the number of false events. Therefore, it is suggested to not use association windows, but the same coincidence trigger technique (Beyreuther et al., 2010) of the MCCT method. If a certain number of signal windows overlap, then it is consider an event. Also, the threshold for considering a group of detections as an event must be increased from 4 to 5 or 6. The number 4 was chosen since at least 4 measurements are needed for solving the variables of the earthquake location; latitude, longitude, depth, and origin time. However, it has proven to not been sufficient, and 1 or 2 extra are needed to constrain the solution.

Regarding back to the event picks, even if the false detections are reduced with setting new Trigger-On and Off values, still this do not solve the accuracy of the first-arrival picks, and then another method is proposed. The first arrival in tremor signals and other type of events without clear first-arrival impulses proved to be difficult to detect with automatic pickings since they are not so emergent as tectonic events, specially for volcanic tremors (Gottschämmer and Surono, 2000; Katsumata and Kamaya, 2003; Sukir et al., 2017; Minetto et al., 2019), and then it constitutes a problem on the 3D location due to inaccurate P-wave picks. For this, another automatic method by reusing the polarization analysis approach is proposed after the association method, as a way to attempt a more accurate picking of the P-waves.

The method consists on re-picking the first-arrival by using a time-window of 2 to 4 seconds, and sliding it with a step of 0.5 seconds along 30 seconds of the event signal; from the first 27 seconds previous to the original first-arrival pick attempted by the Trigger-On, to 3 seconds after the same mentioned pick. On each window step of the sliding process, a polarization analysis is made to the particle motion to obtain the rectilinearity and eigenvalue rations, and the time with the highest rectilinearity and lowest eigenvalue ratios can be chosen as the re-picked P-wave.

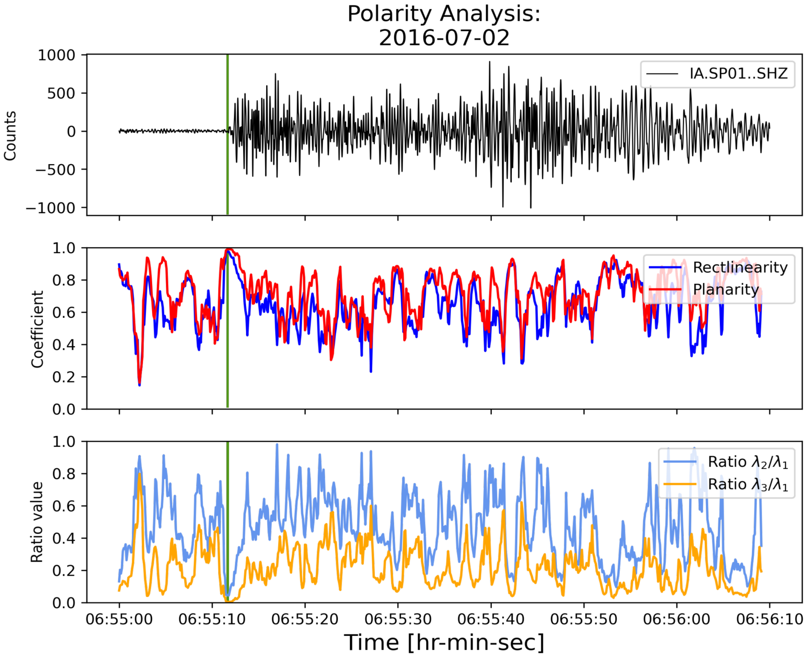

(a) Local seismic event, processed with a pre-filter of 1 to 10 Hz.

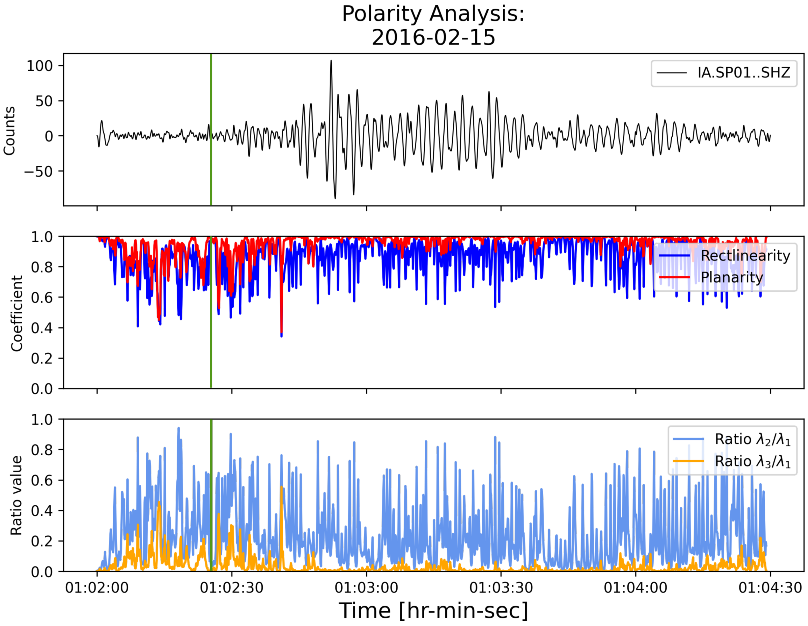

(b) Tremor signal processed with a pre-filter of 0.3 to 1.5 Hz.

Figure 9.1: Polarity analysis made for a local seismic event and a tremor signal with recognizable wave-phases through a 2 seconds window sliding 0.5 seconds. The rectilinearity, planarity, λ_2/λ_1 and λ_3/λ_1 were computed to see the evolution over time. The P-wave arrival is marked with a vertical green line on each case.

The Figures 9.1 show an example of the result of a sliding window technique, applied to 2 different examples; a tectonic event with clear first-arrival and a tremor signal with unclear first-arrival. However, the example shown is the sliding window applied to most of the waveform of the signals. The example for the tectonic event and on the tremor signal shows an increase in the rectilinearity and planarity up to almost 1.0 for the arrival of the P-wave, and the values of rectilinearity and planarity are the highest ones compared to the rest of the trace. In the tremor signal this not clearly shown, however, the values are also the highest ones near the possible first-arrival. Also, they correspond to an weak impulse that can be noticed, which is interpreted to be the P-wave. Therefore, this technique proves to be a potential candidate for achieving P-wave arrival-times from tremor or non good emergent signals, which are essential for 3D location.

Even with the proposed changes and improvements, there are still huge limitations. The dataset is still very compromised since the instruments presents high noise content. Also and most important, the permanent stations used for increasing the azimuthal coverage around Mt. Bromo show information gaps, unavailability of all the components, and in several dates corrupted data in the horizontal channels; as seen by the event gaps and the unclear distribution of rectilinearity and planarity values for events obtained by these stations (see again Figure 7.12). Clearly, for the a reliable performance of the new proposed changes, the dataset must be checked and corrected waveform files must be restored. Besides this, the network by itself would not be able to solve properly the depth of superficial events (depths $\leq$ 10 Km) since the nearest stations to Mt. Bromo are separated by 50 Km or more. According to Sukir et al. (2017), many of these superficial events from peak D, for example, are located on the first 3.5 Km of depth. Therefore, to constrain the depth well, at least 2 stations more over the volcanic structure are needed, and based on the reports of the same authors, the frequency content of the same events might change dramatically between stations on top of the volcano, and distant ones as the BMKG stations or the LUSI network on bedrock.

CHAPTER 10

Conclusions

2-years of continuous recordings were processes to find events in the same frequency range explored by Minetto et al. (2019) as a continuation to their work. The detections achieved along time shows mainly 7 peak periods of high seismic activity; labeled with letters from A to G chronologically, where 4 of them (B, D, E, and F) were found to be temporally linked with eruption episodes of Mt. Bromo mentioned in bulletin reports. However, peak B appears right after an eruption period.

The locations of events with reliable P-phase as first-arrival confirmed by the polarization analysis was done to each peak, and only taking into account the ones with travel-time difference RMS values below 1.0. The peak A correspond some superficial activity from the AW and the Penanggungan volcanic complex, and some deeper ones revealing a possible magmatic connection/interaction between the AW and Mt. Bromo systems.

The peak B shows sources from the AW structure, the Penanggungan volcano, and the Watukosek fault zone, which works as an hydro-thermal conductor between the mentioned volcanic structures and the LUSI site. However, these locations are mostly compromised due to record gaps in the BMKG stations used to extend the search area.

The peak C covers almost 2 months. It describes events coming from the AW and Penanggungan areas, and from the Mt. Bromo and Semeru volcanoes, with durations from 2 to 6 minutes. However, this period was found to show an increase in events, with VT characteristics that preceded the main eruption period of Mt. Bromo, from the end of 2015 to early 2016. It is attributed to high pressure magmatic interactions that could activate pre-existing geological sutures zones in East Java (Southern Uplift). This behavior is consistent with other observations in literature for strombolian volcanoes, previous to main eruptions.

Afterwards, the peak D, as the biggest peak period, marks the main eruption period of Mt. Bromo through 2015-2016, and anticipated by high VT signals from peak C, which is right before. It is mostly dominated by repetitive self-similar tremors, mostly without clear P-phase arrivals and catalogued as multi-phase events, with durations from 2 to 4 minutes. Some of the locations yielded beneath the volcanic structures, and the majority at surface with no clear origin. However, it is suspected to come from Mt. Bromo due to coincidences with eruption, increase in high incidence angle of the events at several stations, and the repetitive presence along the period. The tremor signals are attributed mainly to explosion and particle emissions. Minetto et al. (2019) identified a change in the eruption style, based a progressive change from Type B (continuous tremor) to Type A (fragmented). This study agrees in the eruption style change, however, it was found that the Type A was present since the beginning of the eruption period, while Type B was vanishing.

Near a month passes after the next peak (E) which coincides with the next eruption period of Mt. Bromo. The events presented are similar to the ones in peak D (fragmented tremors), relating to the similar explosion/emission events, but with less amplitude and with an increase in the continuous tremor, a behavior contrary to the one observed at the beginning of the peak D.

The peak F, coinciding with another eruption event, shows mostly events from 5 to 20 Km depth, below Mt. Bromo, and the AW volcanic complex, attributed to thermal interactions and degassing. And finally, the peak event G marks another eruption period from Mt. Bromo at the end of 2016; not identified by Minetto et al. (2019). The surface events show origins from Mt. Bromo and Semeru volcanoes. Nevertheless, deep events showed also a magmatic interaction between Mt. Bromo and Jyan-Argapura volcanoes, revealing that Mt. Bromo has magmatic interaction with AW and Jyan-Argapura.

Many surface events locations were mostly inaccurate due to first-arrival pick errors and association problems with the BMKG stations used to extend the search around Mt. Bromo. These stations, and some of the LUSI network, presented several gaps in their recordings, and malfunctioning in the horizontal components; as shown by the detections and polarization analysis results, which affected the detection and location of the events. This made the automatic processing routing difficult to address and design. Therefore, from errors encountered, several suggestions are made for future works: 1) Adjust the Trigger-On and Trigger-Off by an increment of 0.5, 2) Correct the MCCT method to avoid double pickings (just for statistical purposes), 3) Re-picking of the first-arrival time (P-wave) through a sliding window search with polarization analysis, 4) use the same principle of the MCCT method (detection window overlaps) as an association method. Nevertheless, these changes can not be truly effective if the data of the permanent stations is still compromised.

Bibliography

Ariyanto, P., Rosid, S., Anggono, T., Januarti, Y., et al. (2018). Crustal structure in the southern part of central java based on analysis of tele-seismic receiver function using a neighbourhood algorithm. In *Journal of Physics: Conference Series*, volume 985, page 012018. IOP Publishing.

Bachri, S., Stötter, J., Monreal, M., and Sartohadi, J. (2015). The calamity of eruptions, or an eruption of benefits? mt. bromo human–volcano system a case study of an open-risk perception. *Natural Hazards and Earth System Sciences*, 15(2):277–290.

Ballmer, S., Wolfe, C. J., Okubo, P. G., Haney, M. M., and Thurber, C. H. (2013). Ambient seismic noise interferometry in hawai'i reveals long-range observability of volcanic tremor. *Geophysical Journal International*, 194(1):512–523.

Beyreuther, M., Barsch, R., Krischer, L., Megies, T., Behr, Y., and Wassermann, J. (2010). Obspy: A python toolbox for seismology. *Seismological Research Letters*, 81(3):530–533.

Brumm, M., Manga, M., and Davies, R. (2007). Did an earthquake trigger the eruption of the sidoarjo (lusi) mud volcano? In *AGU Fall Meeting Abstracts*, volume 2007, pages V22C–03.

Centre, G. D. (1993). Geofon seismic network. deutsches geoforschungszentrum gfz. *Other/Seismic Network*.

Davies, R. J., Brumm, M., Manga, M., Rubiandini, R., Swarbrick, R., and Tingay, M. (2008). The east java mud volcano (2006 to present): an earthquake or drilling trigger? *Earth and Planetary Science Letters*, 272(3-4):627–638.

Diaz, J., Schimmel, M., Ruiz, M., and Carbonell, R. (2020). Seismometers within cities: a tool to connect earth sciences and society. *Frontiers in Earth Science*, 8:9.

Dimock, G. et al. (1989). *The unity of the Odyssey.* University of Massachusetts Press.

Droznin, D., Shapiro, N., Droznina, S. Y., Senyukov, S., Chebrov, V., and Gordeev, E. (2015). Detecting and locating volcanic tremors on the klyuchevskoy group of volcanoes (kamchatka) based on correlations of continuous seismic records. *Geophysical Journal International*, 203(2):1001–1010.

Eisner, L., Fischer, T., and Rutledge, J. T. (2009). Determination of s-wave slowness from a linear array of borehole receivers. *Geophysical Journal International*, 176(1):31–39.

Fallahi, M. J., Obermann, A., Lupi, M., Karyono, K., and Mazzini, A. (2017). The plumbing system feeding the lusi eruption revealed by ambient noise tomography. *Journal of Geophysical Research: Solid Earth*, 122(10):8200–8213.

Flinn, E. (1965). Signal analysis using rectilinearity and direction of particle motion. *Proceedings of the IEEE*, 53(12):1874–1876.

Geiger, L. (1912). Probability method for the determination of earthquake epicenters from the arrival time only. *Bull. St. Louis Univ*, 8(1):56–71.

Ginevra, R. (2018). Old norse sígyn (* sei k-n-i éh2-'she of the pouring'), vedic sécanī-'pouring', celtic sēquana and pie* sei k-'pour'*. In *Proceedings of the 29th Annual UCLA Indo-European Conference.*

Gottschämmer, E. and Surono, I. (2000). Locating tremor and shock sources recorded at bromo volcano. *Journal of volcanology and geothermal research*, 101(1-2):199–209.

Greene, M. T. (2015). *Alfred Wegener: Science, exploration, and the theory of continental drift.* JHU Press.

Greenhalgh, S., Sollberger, D., Schmelzbach, C., and Rutty, M. (2018). Single-station polarization analysis applied to seismic wavefields: A tutorial. *Advances in Geophysics*, 59:123–170.

Gresko, M., Suria, C., and Sinclair, S. (1995). Basin evolution of the ardjuna rift system and its implications for hydrocarbon exploration, offshore northwest java, indonesia.

Haberland, C., Bohm, M., and Asch, G. (2014). Accretionary nature of the crust of central and east java (indonesia) revealed by local earthquake travel-time tomography. *Journal of Asian Earth Sciences*, 96:287–295.

Hall, R. (2011). Australia–se asia collision: plate tectonics and crustal flow. *Geological Society, London, Special Publications*, 355(1):75–109.

Hariyono, E. and Liliasari, S. (2018). The characteristics of volcanic eruption in indonesia. *Volcanoes: Geological and Geophysical Setting, Theoretical Aspects and Numerical Modeling, Applications to Industry and Their Impact on the Human Health*, 73.

Harris, A. J. and Ripepe, M. (2007). Regional earthquake as a trigger for enhanced volcanic activity: evidence from modis thermal data. *Geophysical Research Letters*, 34(2).

Havskov, J. and Alguacil, G. (2004). *Instrumentation in earthquake seismology*, volume 358. Springer.

Hidayati, S., Triastuty, H., Mulyana, I., Adi, S., Ishihara, K., Basuki, A., Kuswandarto, H., Priyanto, B., and Solikhin, A. (2019). Differences in the seismicity preceding the 2007 and 2014 eruptions of kelud volcano, indonesia. *Journal of Volcanology and Geothermal Research*, 382:50–67.

Hill, D. P., Pollitz, F., Newhall, C., et al. (2002). Earthquake-volcano interactions. *Physics Today*, 55(11):41–47.

Istadi, B. P., Pramono, G. H., Sumintadireja, P., and Alam, S. (2009). Modeling study of growth and potential geohazard for lusi mud volcano: East java, indonesia. *Marine and Petroleum Geology*, 26(9):1724–1739.

Jousset, P., Budi-Santoso, A., Jolly, A. D., Boichu, M., Dwiyono, S., Sumarti, S., Hidayati, S., Thierry, P., et al. (2013). Signs of magma ascent in lp and vlp seismic events and link to degassing: an example from the 2010 explosive eruption at merapi volcano, indonesia. *Journal of Volcanology and Geothermal Research*, 261:171–192.

Jurkevics, A. (1988). Polarization analysis of three-component array data. *Bulletin of the seismological society of America*, 78(5):1725–1743.

Kanamori, H. and Brodsky, E. E. (2004). The physics of earthquakes. *Reports on Progress in Physics*, 67(8):1429.

Kaneko, T., Maeno, F., and Yasuda, A. (2019). Observation of the eruption sequence and formation process of a temporary lava lake during the june–august 2015 mt. raung eruption, indonesia, using high-resolution and high-frequency satellite image datasets. *Journal of Volcanology and Geothermal Research*, 377:17–32.

Karasözen, E. and Karasözen, B. (2020). Earthquake location methods. *GEM-International Journal on Geomathematics*, 11(1):1–28.

Karyono, K., Mazzini, A., Lupi, M., Syafri, I., Haryanto, I., Masturyono, M., Hadi, S., Rohadi, S., Suardi, I., Rudiyanto, A., et al. (2015). The lusi seismic experiment: Deployment of a seismic network around lusi, east java, indonesia. In *EGU General Assembly Conference Abstracts*, page 14315.

Katsumata, A. and Kamaya, N. (2003). Low-frequency continuous tremor around the moho discontinuity away from volcanoes in the southwest japan. *Geophysical Research Letters*, 30(1):20–1.

Konstantinou, K. I. and Schlindwein, V. (2003). Nature, wavefield properties and source mechanism of volcanic tremor: a review. *Journal of Volcanology and Geothermal Research*, 119(1-4):161–187.

Koulakov, I., Bohm, M., Asch, G., Lühr, B.-G., Manzanares, A., Brotopuspito, K., Fauzi, P., Purbawinata, M., Puspito, N., Ratdomopurbo, A., et al. (2007). P and s velocity structure of the crust and the upper mantle beneath central java from local tomography inversion. *Journal of Geophysical Research: Solid Earth*, 112(B8).

Kumar, S., Kapur, P., and Vig, R. (2019). Computational technique for onset of p-wave for seismic alert system. In *Proceedings of 2nd International Conference on Communication, Computing and Networking*, pages 849–859. Springer.

Kundu, B. and Gahalaut, V. (2011). Slab detachment of subducted indo-australian plate beneath sunda arc, indonesia. *Journal of earth system science*, 120(2):193–204.

Lecocq, T., Hicks, S. P., Van Noten, K., Van Wijk, K., Koelemeijer, P., De Plaen, R. S., Massin, F., Hillers, G., Anthony, R. E., Apoloner, M.-T., et al. (2020). Global quieting of high-frequency seismic noise due to covid-19 pandemic lockdown measures. *Science*, 369(6509):1338–1343.

Lloyd, G. E. R. (2012). *Early greek science: Thales to Aristotle*. Random House.

Lois, A., Sokos, E., Martakis, N., Paraskevopoulos, P., and Tselentis, G.-A. (2013). A new automatic s-onset detection technique: Application in local earthquake data. *Geophysics*, 78(1):KS1–KS11.

Lomax, A. (2004). Probabilistic, non-linear, global-search earthquake location in 3d media. *Anthony Lomax Scientific Software, Mouans–Sartoux, France.*

Lupi, M., Mazzini, A., Sciarra, A., Collignon, M., Schmid, D. W., Husein, A., Romeo, G., Obermann, A., and Karyono, K. (2018). Enhanced hydrothermal processes at the new-born lusi eruptive system, indonesia. *Journal of Volcanology and Geothermal Research*, 366:47–57.

Lupi, M., Saenger, E. H., Fuchs, F., and Miller, S. (2013). Lusi mud eruption triggered by geometric focusing of seismic waves. *Nature Geoscience*, 6(8):642–646.

Marliyani, G. I., Helmi, H., Arrowsmith, J. R., and Clarke, A. (2020). Volcano morphology as an indicator of stress orientation in the java volcanic arc, indonesia. *Journal of Volcanology and Geothermal Research*, 400:106912.

Maryanto, S., Iguchi, M., and Tameguri, T. (2008). Constraints on the source mechanism of harmonic tremors based on seismological, ground deformation, and visual observations at sakurajima volcano, japan. *Journal of Volcanology and Geothermal Research*, 170(3-4):198–217.

Mazzini, A. (2018). 10 years of lusi eruption: Lessons learned from multidisciplinary studies (lusi lab).

Mazzini, A. and Etiope, G. (2017). Mud volcanism: An updated review. *Earth-Science Reviews*, 168:81–112.

Mazzini, A., Etiope, G., and Svensen, H. (2012). A new hydrothermal scenario for the 2006 lusi eruption, indonesia. insights from gas geochemistry. *Earth and Planetary Science Letters*, 317:305–318.

Mazzini, A., Nermoen, A., Krotkiewski, M., Podladchikov, Y., Planke, S., and Svensen, H. (2009). Strike-slip faulting as a trigger mechanism for overpressure release through piercement structures. implications for the lusi mud volcano, indonesia. *Marine and Petroleum Geology*, 26(9):1751–1765.

Mazzini, A., Svensen, H., Akhmanov, G., Aloisi, G., Planke, S., Malthe-Sørenssen, A., and Istadi, B. (2007). Triggering and dynamic evolution of the lusi mud volcano, indonesia. *Earth and Planetary Science Letters*, 261(3-4):375–388.

McCausland, W. A., Gunawan, H., White, R. A., Indrastuti, N., Patria, C., Suparman, Y., Putra, A., Triastuty, H., and Hendrasto, M. (2019). Using a process-based model of pre-eruptive seismic patterns to forecast evolving eruptive styles at sinabung volcano, indonesia. *Journal of Volcanology and Geothermal Research*, 382:253–266.

Miller, S. A. and Mazzini, A. (2018). More than ten years of lusi: a review of facts, coincidences, and past and future studies. *Marine and Petroleum Geology*, 90:10–25.

Millman, K. J. and Aivazis, M. (2011). Python for scientists and engineers. *Computing in Science & Engineering*, 13(2):9–12.

Minetto, R., Maupin, V., Planès, T., Mazzini, A., and Lupi, M. (2019). Sustained low-frequency seismic activity as possible far-field espression of the 2015/2016 mt bromo's volcanic unrest, east java, indonesia.

Moscariello, A., Do Couto, D., Mondino, F., Booth, J., Lupi, M., and Mazzini, A. (2018). Genesis and evolution of the watukosek fault system in the lusi area (east java). *Marine and Petroleum Geology*, 90:125–137.

Müller, C., Barckhausen, U., Ehrhardt, A., Engels, M., Gaedicke, C., Keppler, H., Lutz, R., Lüschen, E., Neben, S., Kopp, H., et al. (2008). From subduction to collision: The sunda-banda arc transition. *Eos, Transactions American Geophysical Union*, 89(6):49–50.

Obermann, A., Karyono, K., Diehl, T., Lupi, M., and Mazzini, A. (2018). Seismicity at lusi and the adjacent volcanic complex, java, indonesia. *Marine and Petroleum Geology*, 90:149–156.

Panzera, F., D'Amico, S., Lupi, M., Mauri, G., Karyono, K., and Mazzini, A. (2018). Lusi hydrothermal structure inferred through ambient vibration measurements. *Marine and Petroleum Geology*, 90:116–124.

Parkinson, C. D., Miyazaki, K., Wakita, K., Barber, A., and Carswell, D. (1998). An overview and tectonic synthesis of the pre-tertiary very-high-pressure metamorphic and associated rocks of java, sulawesi and kalimantan, indonesia. *Island Arc*, 7(1-2):184–200.

Pfeiffer, T. (2017). Volcano discovery.

Procesi, M., Ciotoli, G., Mazzini, A., and Etiope, G. (2019). Sediment-hosted geothermal systems: Review and first global mapping. *Earth-science reviews*, 192:529–544.

Rachmawati, T. A., Rahmawati, D., and Rachmansyah, A. (2018). Disaster risk analysis of mount bromo eruption after the 2015 eruption in sukapura district. In *MATEC Web of Conferences*, volume 229, page 01015. EDP Sciences.

Richards, J. (2011). Report into the past, present, and future social impacts of lumpur sidoarjo. *Humanitus Sidoarjo Fund*.

Rosid, M. S. and Ramadhanti, W. A. (2019). Implementation of esa-mwt method satellite gravitation data to estimate the depth of moho layer and subduction zone in indo-australia plate of central java. In *Journal of Physics: Conference Series*, volume 1153, page 012020. IOP Publishing.

Ryacudu, R. and Bachtiar, A. (2000). The status of the oo-brebes fault system, and its implication to hydrocarbon exploration in the eastern part of north west java basin.

Satyana, A. H. (2006). New insight on tectonics of central java, indonesia and its petroleum implications. In *American Association Of Petroleum Geologists (AAPG) International Conference and Exhibition*, page 90061.

Satyana, A. H. (2007). Central java, indonesia–a "terra incognita" in petroleum exploration: New considerations on the tectonic evolution and petroleum implications.

Satyana, A. H., Erwanto, E., and Prasetyadi, C. (2004). Rembang-madura-kangean-sakala (rmks) fault zone, east java basin: The origin and nature of a geologic border. *Proc. IAGI, 33rd., Ann. Conv. and Exh., Bandung.*

Sawolo, N., Sutriono, E., Istadi, B. P., and Darmoyo, A. B. (2009). The lusi mud volcano triggering controversy: Was it caused by drilling? *Marine and Petroleum Geology*, 26(9):1766–1784.

Sawolo, N., Sutriono, E., Istadi, B. P., and Darmoyo, A. B. (2010). Was lusi caused by drilling?–authors reply to discussion. *Marine and Petroleum Geology*, 27(7):1658.

SCEDC, S. C. E. C. (2013). Southern california earthquake center. *Caltech. Dataset.*

Sharma, B., Kumar, A., and Murthy, V. (2010). Evaluation of seismic events detection algorithms. *Journal of the Geological Society of India*, 75(3):533–538.

Smits, G. (2006). Shaking up japan: Edo society and the 1855 catfish picture prints. *Journal of Social History*, 39(4):1045–1078.

Smyth, H. R., Hall, R., and Nichols, G. J. (2008). Cenozoic volcanic arc history of east java, indonesia: The stratigraphic record of eruptions on an active continental margin. *Special Papers-Geological Society of America*, 436:199.

Soeria-Atmadja, R., Maury, R., Bellon, H., Pringgoprawiro, H., Polve, M., and Priadi, B. (1994). Tertiary magmatic belts in java. *Journal of southeast asian earth sciences*, 9(1-2):13–27.

Stein, S. and Wysession, M. (2009). *An introduction to seismology, earthquakes, and earth structure*. John Wiley & Sons.

Stewart, S. W. (1977). Real-time detection and location of local seismic events in central california. *Bulletin of the Seismological Society of America*, 67(2):433–452.

Sukir, M., Meidi, A., Vanisa, S., and Hetty, T. (2017). Polarization of volcanic tremor recorded at bromo volcano, east java, indonesia. *International Journal of Applied Environmental Sciences*, 12(11):1993–2005.

Susilo, I. M., Abidin, H. Z., and Sapiie, B. (2015). A new definition of sunda block rotation model. In *Joint Convention Balikpapan 2015 HAGI-IAGI-IAFMI-IATMI.*

Swindell, W. and Snell, N. (1977). Station processor automatic signal detection system, phase i: Final report, station processor software development. *Texas Instruments Report No. ALEX (01)-FR-77-01, AFTAC Contract Number FO8606-76-C-0025, Texas Instruments Incorporated, Dallas, Texas.*

Sya'bani, Y. A., Novianty, A., and Prasasti, A. L. (2020). Implementation of automatic first arrival picking on p-wave seismic signal using logistic regression method. In *2020 8th International Conference on Information and Communication Technology (ICoICT)*, pages 1–5. IEEE.

Trnkoczy, A. (2009). Understanding and parameter setting of sta/lta trigger algorithm. In *New Manual of Seismological Observatory Practice (NMSOP)*, pages 1–20. Deutsches GeoForschungsZentrum GFZ.

Tsapanos, T. (2014). How do you determine events as good quality only from catalog data (when the waveform data is not available)?

Venzke, E., e. (2016). Global volcanism program. report on tengger caldera (indonesia). *Bulletin of the Global Volcanism Network*, 41(12).

Venzke, E., e. (2021). Global volcanism program. report on tengger caldera (indonesia). *Bulletin of the Global Volcanism Network*, 46(2).

Vidale, J. E. (1986). Complex polarization analysis of particle motion. *Bulletin of the Seismological society of America*, 76(5):1393–1405.

Walck, M. C. and Chael, E. P. (1991). Optimal backazimuth estimation for three-component recordings of regional seismic events. *Bulletin of the Seismological Society of America*, 81(2):643–666.

Wardoyo, A. Y., Noor, J. A., Elbers, G., Schmitz, S., Flaig, S. T., and Budianto, A. (2020). Characterizing volcanic ash elements from the 2015 eruptions of bromo and raung volcanoes, indonesia. *Polish Journal of Environmental Studies*, 29(2):1899–1907.

White, R. and McCausland, W. (2016). Volcano-tectonic earthquakes: A new tool for estimating intrusive volumes and forecasting eruptions. *Journal of Volcanology and Geothermal Research*, 309:139–155.

Willumsen, P. and Schiller, D. M. (1994). High quality volcaniclastic sandstone reservoirs in east java, indonesia.

Withers, M., Aster, R., Young, C., Beiriger, J., Harris, M., Moore, S., and Trujillo, J. (1998). A comparison of select trigger algorithms for automated global seismic phase and event detection. *Bulletin of the Seismological Society of America*, 88(1):95–106.

Wölbern, I. and Rümpker, G. (2016). Crustal thickness beneath central and east java (indonesia) inferred from p receiver functions. *Journal of Asian Earth Sciences*, 115:69–79.

Yan, H.-S. and Hsiao, K.-H. (2006). The development of ancient earthquake instruments. In *International Design Engineering Technical Conferences and Computers and Information in Engineering Conference*, volume 42568, pages 275–279.

Zaputlyaeva, A., Mazzini, A., Blumenberg, M., Scheeder, G., Kürschner, W. M., Kus, J., Jones, M. T., and Frieling, J. (2020). Recent magmatism drives hydrocarbon generation in north-east java, indonesia. *Scientific reports*, 10(1):1–14.

Zhang, Z., Lin, Y., Zhou, Z., and Chen, T. (2019). Adaptive filtering for event recognition from noisy signal: An application to earthquake detection. In *ICASSP 2019-2019 IEEE International Conference on Acoustics, Speech and Signal Processing (ICASSP)*, pages 3327–3331. IEEE.

Appendices

APPENDIX A

Additional Figures

A.1 Data Inspection

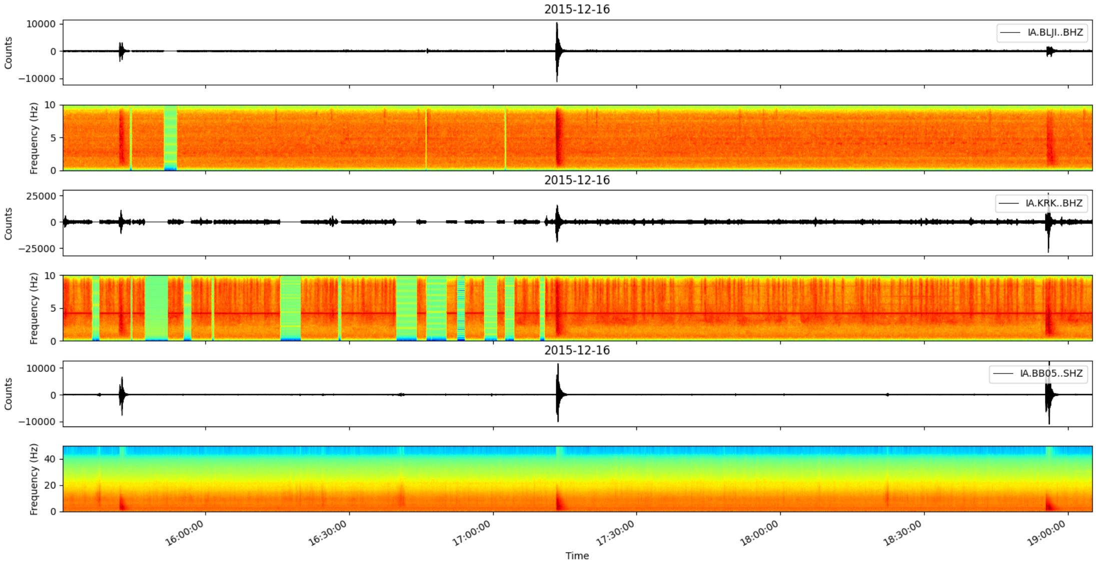

Figure A.1: Signal from Figure 6.4 with bandpass filter between 1 and 10 Hz. Neglecting frequencies below 1 Hz can enhance the signals from the continuous noise.

A.2 Multi-Component Coincidence Trigger

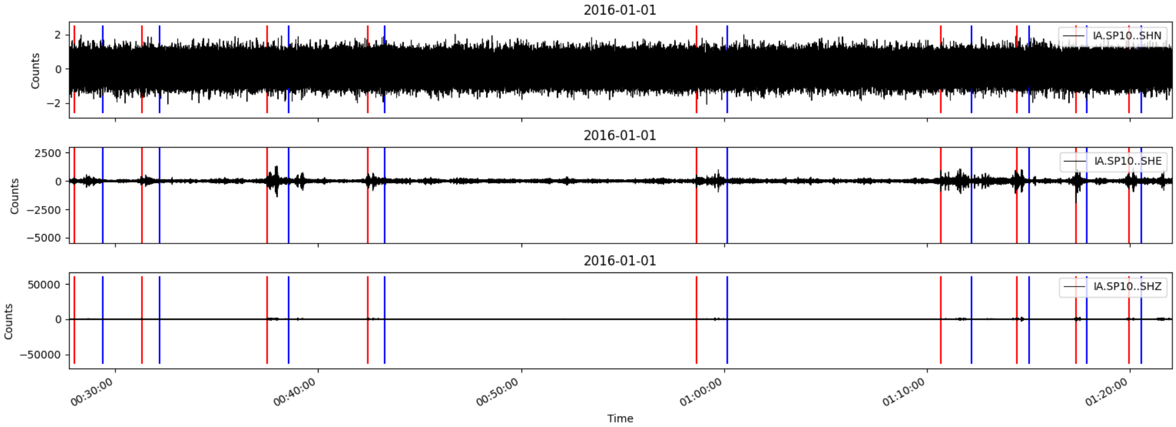

Figure A.2: Multi-component coincidence trigger performance on station SP10 at 2016-01-01 (year-month-day), sliced between 00:27:00 and 01:23:00 UTC, using Recursive STA/LTA in 10-40 Hz pre-filtered data.

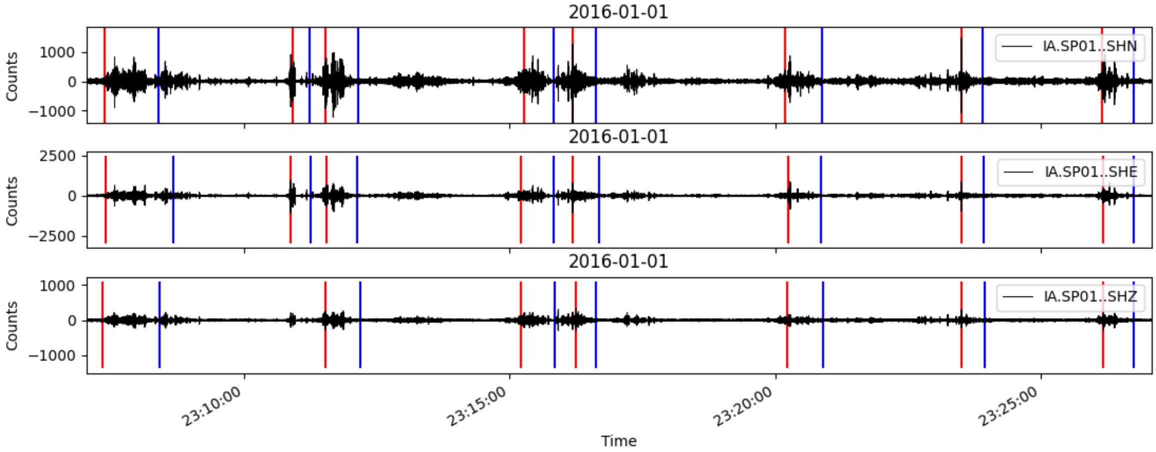

Figure A.3: Example of the Recursive STA/LTA applied individually to each channel of station SP01, with a 10-40 Hz pre-filter. Stream from 2016-01-01 (year-month-day). Notice the difference in time of trigger-on's and trigger-off's at each component for the same evens, and an the first event occurring between 23:10:00 and 23:15:00, not detected in Z channel, but rather in N and E.

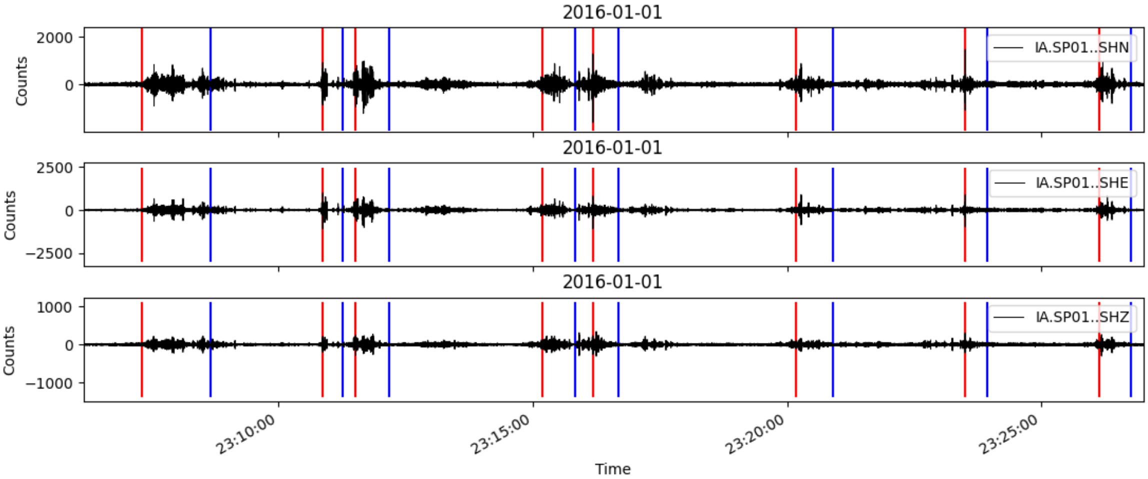

Figure A.4: Result of the multi-component coincidence trigger method applied to station SP01 from the individual channel detections from Figure A.3.

A.3 Detection Methods Results

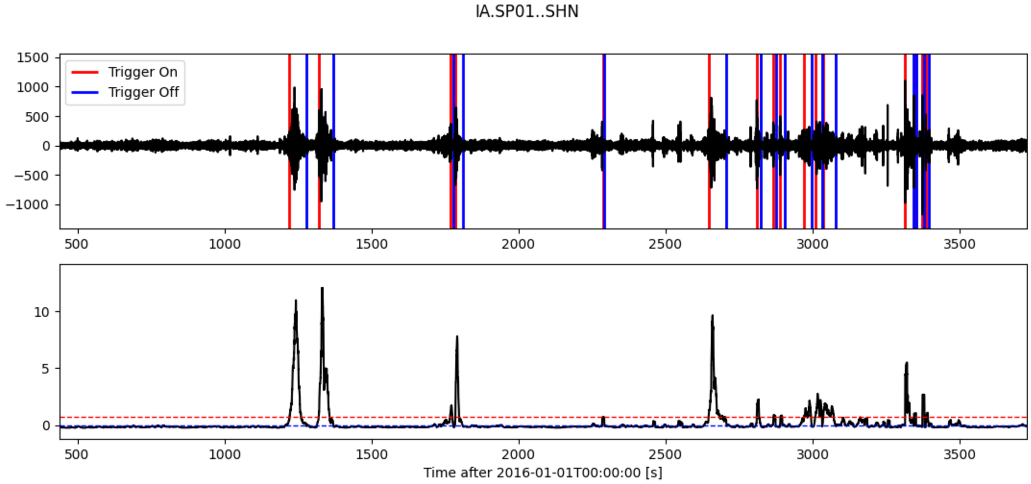

Figure A.5: Multi-component coincidence trigger for station SP10 at 2016-01-01 (year-month-day), sliced between 0 and 3500 seconds after 00:00:00 UTC, using Z-Detect with a 10-40 Hz pre-filter band, and trigger-on and trigger-off values of 0.7 and -0.05.

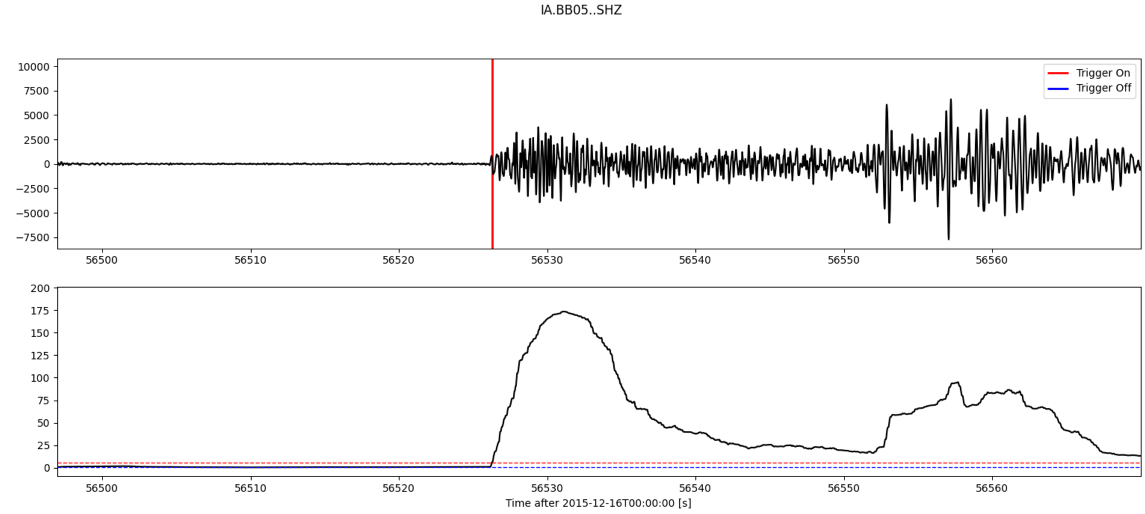

Figure A.6: (Top): First P-wave picking time of a tectonic event recorded at station BB05 at 2015-12-16 (year-month-day) with the Classical STA/LTA detection method. (Bottom): Characteristic function produced by the detection method around the P-wave with the trigger-on and trigger-off values as red and blue horizontal dashed lines. Parameters chosen are shown in Table 6.1.

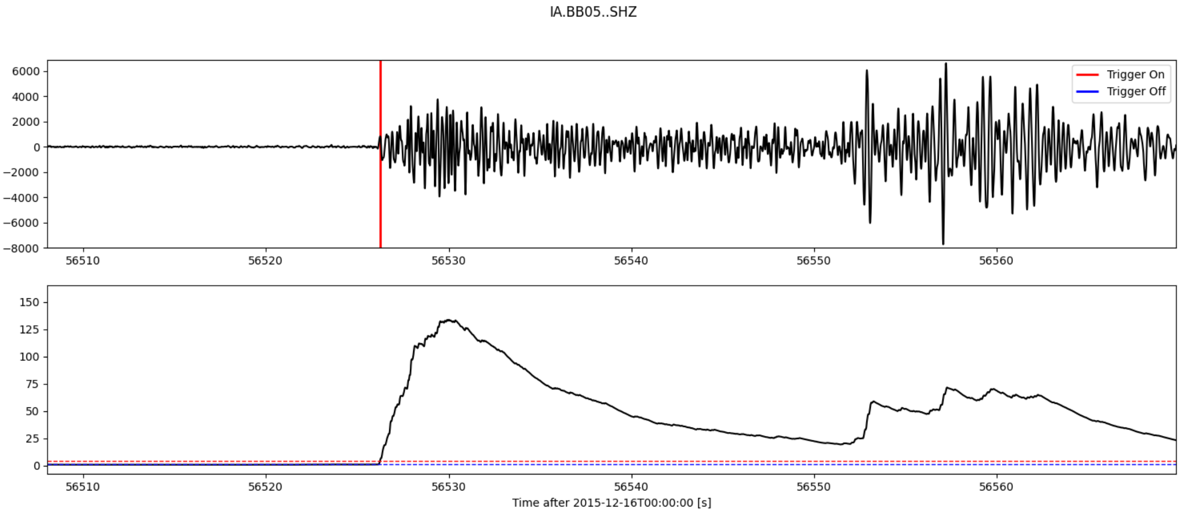

Figure A.7: (Top): First P-wave picking time of a tectonic event recorded at station BB05 at 2015-12-16 (year-month-day) with the Recursive STA/LTA detection method. (Bottom): Characteristic function produced by the detection method around the P-wave with the trigger-on and trigger-off values as red and blue horizontal dashed lines. Parameters chosen are shown in Table 6.1.

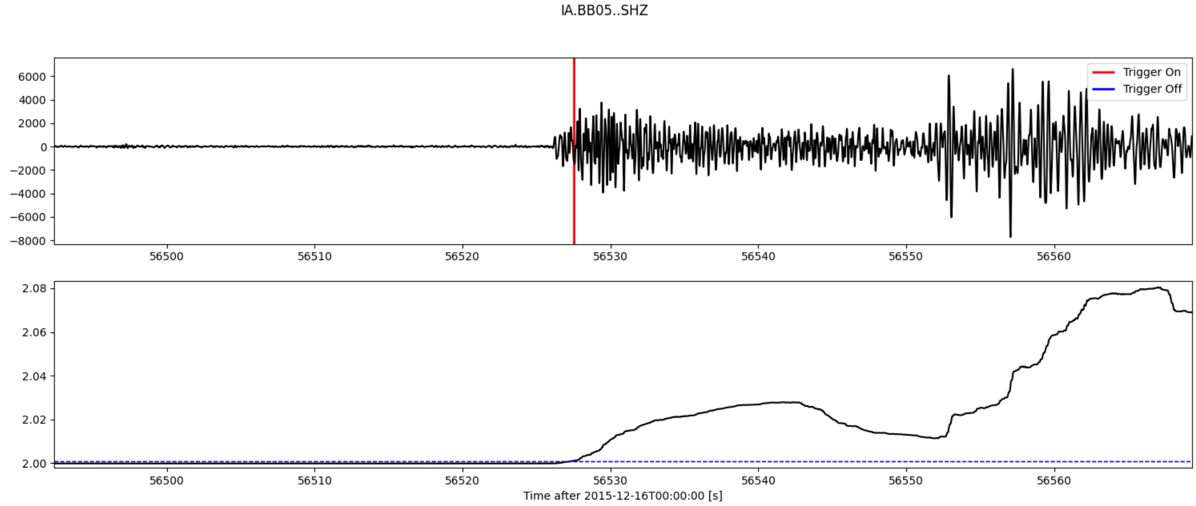

Figure A.8: (Top): First P-wave picking time of a tectonic event recorded at station BB05 at 2015-12-16 (year-month-day) with the Delayed STA/LTA detection method. (Bottom): Characteristic function produced by the detection method around the P-wave with the trigger-on and trigger-off values as red and blue horizontal dashed lines. Parameters chosen are shown in Table 6.1.

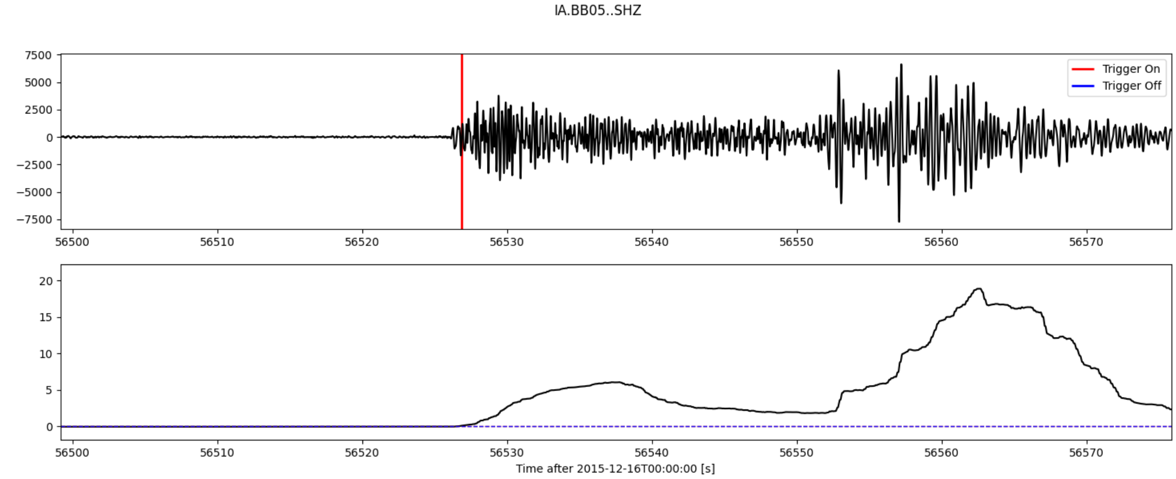

Figure A.9: (Top): First P-wave picking time of a tectonic event recorded at station BB05 at 2015-12-16 (year-month-day) with the Z-Detect detection method. (Bottom): Characteristic function produced by the detection method around the P-wave with the trigger-on and trigger-off values as red and blue horizontal dashed lines. Parameters chosen are shown in Table 6.1.

APPENDIX B

Tables

B.1 Velocity models

Table B.1: Velocity model from Ariyanto et al. (2018). $V_p/V_s = 1.9$

Depth (Km)	**V$_s$ (Km/s)**
0	0.6
2	3.4
4	3.2
6	3.0
8	2.8
10	3.8
12	3.6
14	3.5
16	3.4
18	3.2
20	2.5
26	2.8
38	5.0
70	5.0

Table B.2: Velocity model from Koulakov et al. (2007). $V_p/V_s = 1.74$

Depth (Km)	**V$_p$ (Km/s)**
0	4.3
3	4.9
8	5.7
16	6.9
24	7.1
77	7.8
120	8.05
165	8.17
210	8.3

Table B.3: Velocity model from Obermann et al. (2018). $V_p/V_s = 1.74$

Depth (Km)	**V$_p$ (Km/s)**
0	5.1
2	5.3
5.2	5.8
8.4	6.3
11.6	6.8
20	7.0
30	7.0

B.2 Station Specifications

Table B.4: List of the available stations for the study, and their specifications.

Station	**Latitude (°)**	**Longitude (°)**	**Elevation (m)**	**Instrument**	**Datalogger**	**Sample Rate (Hz)**	**Type**	**Ground Type**
BB01	-7.66678	112.51500	579.0	Guralp CMG-3T 120s	EarthData	100	broad_band	bedrock
BB02	-7.56969	112.67508	98.0	Guralp CMG-3T 120s	EarthData	100	broad_band	bedrock
BB03	-7.75155	112.66239	779.0	Guralp CMG-3T 120s	EarthData	100	broad_band	bedrock
BB04	-7.60764	112.54736	319.0	Guralp CMG-3T 120s	EarthData	100	broad_band	bedrock
BB05	-7.66000	112.41760	500.0	Guralp CMG-3T 120s	EarthData	100	broad_band	bedrock
BB06	-7.47007	112.74787	22.0	Guralp CMG-3T 120s	EarthData	100	broad_band	basin
BB07	-7.82224	112.52538	1100.0	Guralp CMG-3T 120s	EarthData	100	broad_band	bedrock
BB08	-7.58217	112.61199	276.0	Guralp CMG-3T 120s	EarthData	100	broad_band	bedrock
BB09	-7.50609	112.69343	38.0	Guralp CMG-3T 120s	EarthData	100	broad_band	basin
BB10	-7.61472	112.71952	96.0	Guralp CMG-3T 120s	EarthData	100	broad_band	bedrock
SP01	-7.82070	112.65490	899.0	Lennartz LE-3Dlite Mk II 1s	Nanometrics TAURUS	100	short_period	bedrock
SP02	-7.80890	112.45940	1251.0	Lennartz LE-3Dlite Mk II 1s	Nanometrics TAURUS	100	short_period	bedrock
SP03	-7.61820	112.64480	543.0	Lennartz LE-3Dlite Mk II 1s	Nanometrics TAURUS	100	short_period	bedrock
SP04	-7.42875	112.76720	12.0	Lennartz LE-3Dlite Mk II 1s	Nanometrics TAURUS	100	short_period	basin
SP05	-7.53090	112.69510	33.0	Lennartz LE-3Dlite Mk II 1s	Nanometrics TAURUS	100	short_period	basin
SP06	-7.52858	112.67147	46.0	Lennartz LE-3Dlite Mk II 1s	Nanometrics TAURUS	100	short_period	basin
SP07	-7.55378	112.73259	35.0	Lennartz LE-3Dlite Mk II 1s	Nanometrics TAURUS	100	short_period	basin
SP08	-7.50295	112.74337	35.0	Lennartz LE-3Dlite Mk II 1s	Nanometrics TAURUS	100	short_period	basin
SP09	-7.54083	112.69342	34.0	Lennartz LE-3Dlite Mk II 1s	Nanometrics TAURUS	100	short_period	basin
SP10	-7.48538	112.70097	30.0	Lennartz LE-3Dlite Mk II 1s	Nanometrics TAURUS	100	short_period	basin
SP11	-7.56300	112.77570	36.0	Lennartz LE-3Dlite Mk II 1s	Nanometrics TAURUS	100	short_period	basin

Table B.4 continued from previous page

Station	Latitude (°)	Longitude (°)	Elevation (m)	Instrument	Datalogger	Sampling Rate (Hz)	Type	Ground Type
SP12	-7.53112	112.73709	43.0	Lennartz LE-3Dlite Mk II 1s	Nanometrics TAURUS	100	short_period	basin
SP13	-7.54780	112.71270	37.0	Lennartz LE-3Dlite Mk II 1s	Nanometrics TAURUS	100	short_period	basin
SP14	-7.45868	112.64050	42.0	Lennartz LE-3Dlite Mk II 1s	Nanometrics TAURUS	100	short_period	basin
SP15	-7.50610	112.67280	34.0	Lennartz LE-3Dlite Mk II 1s	Nanometrics TAURUS	100	short_period	basin
SP16	-7.48340	112.66747	36.0	Mark L-4-3D 1s	EarthData	200	short_period	basin
SP17	-7.58986	112.70984	51.0	Mark L-4-3D 1s	EarthData	200	short_period	bedrock
SP18	-7.51585	112.73067	25.0	Mark L-4-3D 1s	EarthData	200	short_period	basin
SP19	-7.54207	112.74366	12.0	Mark L-4-3D 1s	EarthData	200	short_period	basin
SP20	-7.53169	112.63348	31.0	Mark L-4-3D 1s	EarthData	200	short_period	basin
SP21	-7.54990	112.73390	42.0	Lennartz LE-3Dlite Mk II 1s	Nanometrics TAURUS	100	short_period	basin
SP22	-7.53000	112.71490	45.0	Lennartz LE-3Dlite Mk II 1s	ANU	250	short_period	basin
SP23	-7.47007	112.74787	22.0	Lennartz LE-3Dlite Mk II 1s	Nanometrics TAURUS	100	short_period	basin
SP24	-7.47007	112.74787	22.0	Lennartz LE-3Dlite Mk II 1s	Nanometrics TAURUS	100	short_period	basin
BLJI	-7.74500	113.59500	80.8	STS-2 120s	*NA*	20	BMKG_Net	bedrock
GMJI	-8.27320	113.44410	80.1	STS-2 120s	*NA*	20	BMKG_Net	bedrock
KRK	-8.15210	112.45060	330.3	STS-2 120s	*NA*	20	BMKG_Net	bedrock

APPENDIX C

Code

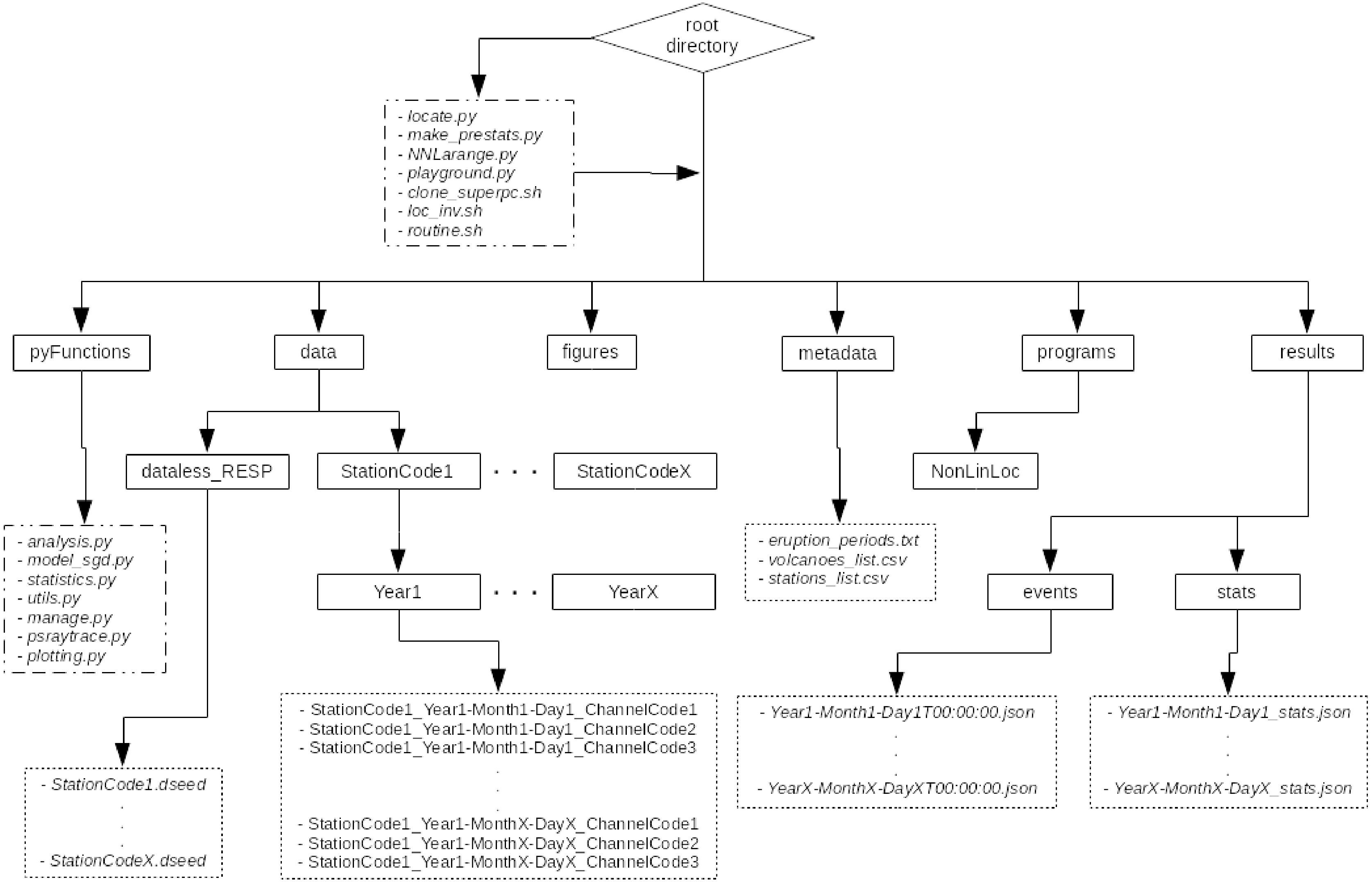

Figure C.1: Code architecture used on this project. The entire code can be found in: https://github.com/Doctus5/TremRoutine. The code architecture is explained below and in the README file of the repository, as well as a description of each main file. Thereafter, every Python file contains the description of each of the methods within.

The root directory or folder DO NOT make reference to the root folder of any UNIX-core type device. Therefore, "root directory" means a main folder of the user's preference on where to store the cloned repository (this one).

Due to confidentiality of ERC-funded Lusi Lab project, the initial dataset cannot be shared (waveform files and response files) as well as the results. Therefore, the "data" and "results" folders shown in the architecture scheme of the program are not included. However, any used dataset must be organized in the specified hierarchical order of the folders.

The content inside "results" will be automatically generated. Files generated for statistics under "stats" folder and the database of the events in the "events" folder will be as .JSON files. Each one in "events" will be a list of dictionaries, where each dictionary corresponds to one event:

Stations and components involved in the detection of that specific events. Waveform file paths involved in the detection. Arrival times per station (tart-end of the detection). Start-End times for waveform extraction of the event in each station involved (for post-processing cases).

The folder "pyFunctions" contains most of the Python files that has the methods for manipulation files around the architecture, between the third-party codes and the other folders, detection and association steps, polarization analysis, plotting functions, and statistics of the detections achieved.

All images that can be produced will be stored in the folder called "figures" if running the plotting functions inside "pyFunctions/plotting.py" and deciding to save them. Currently no folder named "figures" is presented by the same confidentiality agreement, as the files also present results. A folder called with the same name can just be created from scratch by the user.

The "metadata" folder contains files related to the position of stations and volcanoes. Also other priory information can be saved here.

The "programs" folder is designed to contain third-party codes and external programs such as NonLinLoc (Lomax, 2004) that can be used for the location part. Normally this code is designed to work with NonLinLoc installed/compiled within a folder called "NonLinLoc" inside of the "programs" folder. Internal executions for travel-time calculations and probailistic model must be made before with the commands of NonLinLoc locally on the folder of the code.

The other Python files outside of the folders are made for managing functions that are mainly in "pyFunctions" folder. This includes:

- "locate.py": code that manages the detection and association of detected signals of possible events. It then generates the database of the events in the "results" and "stats" folder. Control parameters are defined inside the file. It has the option for parallelizing the process.
- "make_prestats.py": code that generates additional information as the polarization analysis, P and Rayleigh wave classification, Maximum Amplitude, and others. Once run, it will update the files inside the database of the events with the new calculations. It has the option for parallelizing the process.
- "NNLarange.py": code for managing files during the Location inversion with NonLinLoc, such as copying or deleting files, updating the database with the locations, errors, etc. Location inversions will be done inside "NonLinLoc", under "programs" folder.
- "playground.py": not a relevant file for processing, but just a space for playing with the code, calling other functions such as plotting, printing statistics, exploring detection methods and benchmark tests.
- "clone_superpc.sh": shell script for updating files to the Sigma2 HPC servers.

- "loc_inv.sh": shell script for that once run, it automatically starts the location inversion for all the database by batches. This involves the creation of .obs files for NonLinLoc, the copy of those files into NonLinLoc respective folder, running the inversion, copying the output and writing it to updated files of the database, and cleaning of the NonLinLoc ".obs" files.
- "routine.sh": shell script for running the entire routine, from start (detection and association) to end (location of events in database). Not recommended to run as it will be wise to run the codes separately so the user can supervise each process and have quality control in all of them.